Probabilistic flood forecast model based on remote sensing information

Zixin Zhang

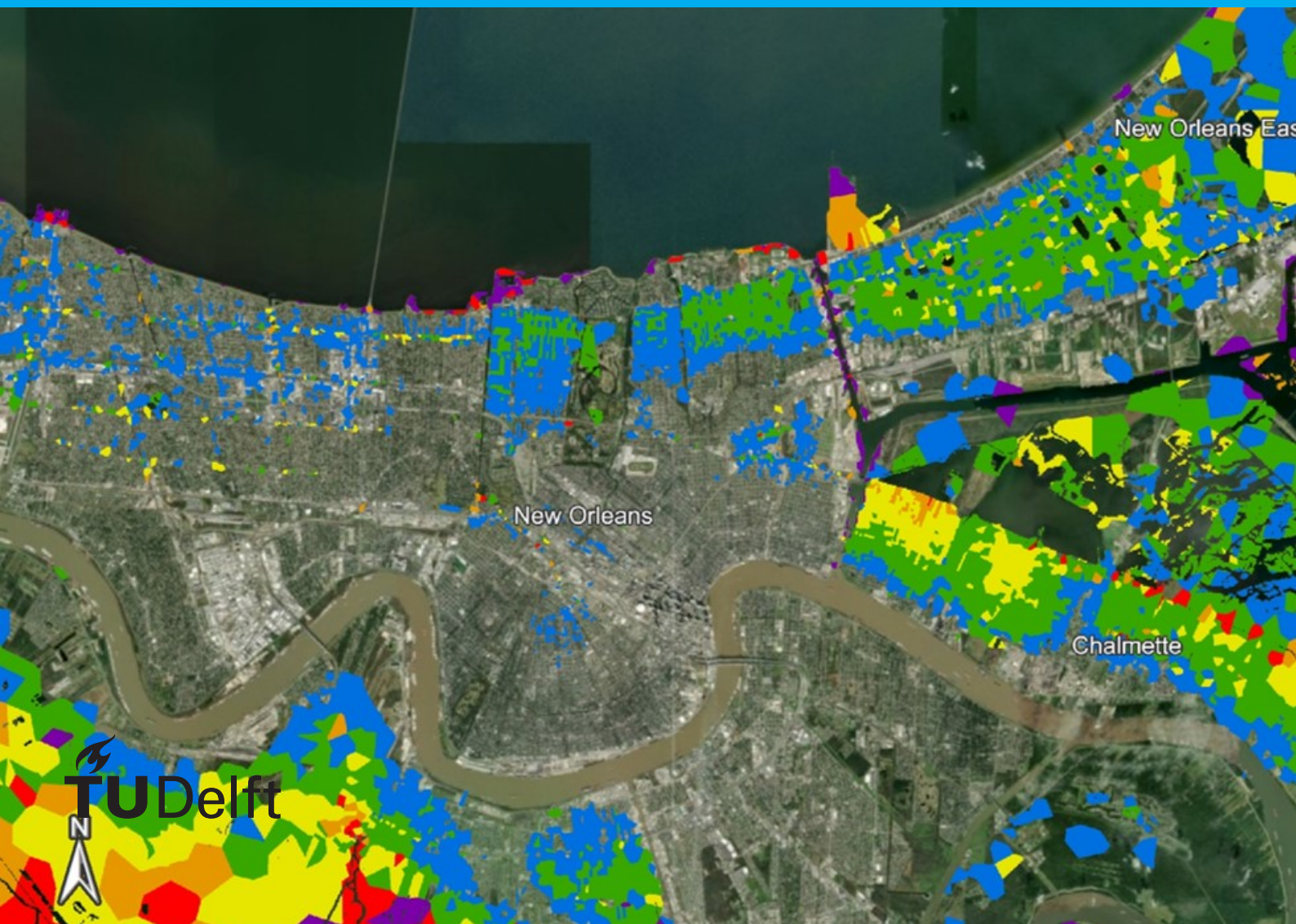

Probabilistic flood forecast model based on remote sensing information

by

Zixin Zhang

to obtain the degree of Master of Science
at the Delft University of Technology,
to be defended publicly on Tuesday, 17th April, 2020 at 9:30 AM.

Student number:	4713117	
Project duration:	April 1, 2019 – April 17, 2020	
Thesis committee:	Prof. dr. ir. Oswaldo Morales Nápoles	TU Delft
	Dr. Sandra Gaytan Aguilar	Deltares, supervisor
	Prof. dr. ir. G.F. Nane	TU Delf
	Dr. ir. Robert Lanzafame	TU Delf

This thesis is confidential and cannot be made public until December 31, 2020.

TU Delft

Deltares
Enabling Delta Life

Preface

In this long ran of writing my master thesis, I have received many helps, supports and advises from many people, to whom I could never express my gratitude enough. Thanks to them, I am able to finish this great adventure.

First I have to thank my committee members, who not only gave my great suggestions and recommendations to the research work, but also taught me a lot about the philosophy of working. I consider it a great luck that Prof.Oswaldo and Sandra allowed me to participate in this research, which is innovative and fits my interests perfectly. My daily supervisor Sandra led me forward during the whole research, and I have learned so much from her about remote sensing, data analysis and working professionally. Dr.Oswaldo and Dr.Tina are brilliant teachers who provided me with a lot of directions on my model. And I received so many instructions from Dr.Robert on improving my writing skills and expanding the scopes of my researches.

Doing your thesis is a tough journey, and when I was facing with obstacles, my family and friends are always there for me. My parents are the most sound support when I am chasing my dream. And I definitely should express my thanks to my friends at the university: Jiechen Zheng, Radityo Andjaringrat Adhi, Naranyanee Gopal and Thanasis Kallioras. They have gave huge help to my research, advising me during the progress. And I am grateful to have friends who gave me emotional support, Yang Yu, Yiting Jia and my roommates.

Zixin Zhang
Delft, April 2020

Contents

Abstract

This study aims to explore the possibility of employing remote sensing images to build a probabilistic flood extent forecasting model. This model is constructed and tested in two study areas: New Orleans and Miami. Images that recorded flooding events are first performed with segmentation method Seed Region Growing, and segmented images are classified by Maximum Likelihood classifier. Area detected as water subtracting the permanent water area is the detected flood extent. In total there are nineteen images being processed. The flood detection result is validated by flooded locations from NOAA flood reports and the news, and the accuracy is at 70.4%. The detection result, with flood conditioning factors which include precipitation, sea level, elevation, drainage capacity and distance to the water area, is the input to the probabilistic forecasting model. All inputs are standardised to a common grid system and every cell in that grid system contains a set of data. Two kinds of model structures are proposed and both models are trained with logistic regression and probit regression, both of which are the members of the Generalised Linear Model(GLM). The first kind of model structure is only tested in the New Orleans study area and the second kind of model structure is examined at both study areas. The precision of the first model structure is at 20% with a kappa value at zero. For the second model structure, over-sampling method SMOTE is used to increase the number of data points of the class 'flooded'. The highest precision of the second model structure at New Orleans is 12.6% and at Miami 23.6%, and the highest cohen's kappa values are 0.127 and 0.131 for New Orleans and Miami respectively.

The first model structure actually failed in building a success model at a large portion of the study area due to limited records. For the second kind of model structure, most variables are linked to the flooding by the model correctly. The precipitation has a positive relation with flooding, especially when time effect is considered. Elevation reduces the probability of flooding. At the Miami study area where no sea dike exists the sea level has a strong positive relation with flooding. Drainage capacity used in the New Orleans study area does not show an influence on flooding, which requires modeling the intricate drainage system more accurately. In Miami study area, when the study area is confined to the seaside and Miami Beach area, the accuracy of prediction is improved, which informs that land-use type is crucial to be considered in the input. This study innovative collected information from several remote sensing images of different flood events and applied the information to build a probabilistic model, which shows that the information provided by mages could link flooding conditioning factors with flooding. It is recommended to incorporate the remote sensing technique in the flood extent forecast model in the future.

Keywords: flood, flood forecasting, remote sensing, probabilistic model

1 Introduction

1.1. Background

Flooding has been one of the severest natural hazards in human history. Each year tens of billions of US dollars are lost by flood and thousands of people lost their lives to floods (Hirabayashi et al., 2013). In the past few decades, due to climate-introduced sea-level rise and extreme weather events, the return period of flooding is getting shorter. At the same time the population density keeps increasing, and many densely populated areas sit at river plain and coastal zone, so one failure in flood defence system could lead to a significant loss in both economics and humanity. It is important for governments and society to have an up-to-date knowledge of flood.

There are four stages in flood management: (1)prediction; (2)preparation; (3)prevention and mitigation; (4)damage assessment(Opolot, 2013). Predicting the amplitude and timing of flooding accurately is an essential step in many fields, such as reservoir management and pre-evacuation. Many types of flood forecasting model have been developed and proven to be helpful. But researchers are keeping improving the performances of models to accommodate to the changing climate. As a result of evolving technology, more sources of information of better quality could be incorporated into models, such as Geographical Information Systems (GIS) and Remote Sensing (RS).

Remote sensing information is proven to be useful in all flood management stages like damage assessment and extraction of flood extent. But most studies of flooding extent detection only focus on one single flood event. Researchers seldom apply multiple RS images to study a series of flooding events.

Now this situation is getting improved with more high-quality RS products being open sources. Resolution or the number of RS images are not constrains anymore, so that we can carry out time-continuous flood analysis. Flood forecasting models are usually driven by past flooding records, and now with a sufficient number of images, it is possible to study flooding characters and build flood forecast model. What is more, unlike gauged data which is sparse, RS images provides extensive and complete information with respect to an extent.

Multi-variate probabilistic models are commonly used in flood forecasting. The generation of flood incorporates rainfall, basin topography, soil moisture and many other factors. Most of them are natural process and some of them are codependent, so multi-variate probabilistic models could precisely describe the mechanism. Although flood forecast based on mathematical model ignore the physical principles of flood generation, it still can capture the essential factors.

1.2. Research objective and methods

The objective of this study is to examine the feasibility of constructing a probabilistic flood extent forecasting model with multiple remote sensing images as input. Researchers have given very satisfying flood detection result by utilising remote sensing images, however few studies have been done to further exploit the results. This study will delineate flood extents of a series of flooding events by using remote sensing images that have recorded them, which serves as the input for the probabilistic models. Flood characters of the study area will be analysed for selecting relative factors in modelling floods. Flood extent forecast models will be trained with flood detection resulting from remote sensing and explanatory factors such as precipitation and sea level.

To perform flood detection, object based image analysis and supervised classification are employed for image processing. Segmentation is first applied to images to delineate the edge of objects which are further classified by using supervised classification. Flooded area is arrived by using objects labelled as 'Water' subtracting permanent water area.

Besides the flood detection result, the flood forecast model's input also includes other auxiliary data which are precipitation, sea level, elevation, distance to the permanent water area and drainage capacity. Two members of generalized linear regression(GLM) family were applied for probabilistic forecasting. While using the same data processing process, regressions and grid system, there are two model structures being constructed to exploit the best way

to train the data. These models are tested in two study areas: New Orleans and Miami.

1.3. Thesis structure

Chapter 1 serves as the introduction to the whole report, giving research background and objectives. Chapter 2 reviews relative literature and provides a research background to this study, where the state of flood forecast model and flood detection on remote sensing are summarised. Chapter 3 gives introduction of two study areas and data exploited in this study. Chapter 4 describes the methodologies of processing remote sensing image and constructing a flood forecast model. In chapter 5, the flood detection result is presented and discussed. Chapter 6 illustrates the construction of the probabilistic flood forecast model by incorporating auxiliary data and using Generalized Linear Regressions. In chapter 7 the whole study is summarised and suggestions were given for improvement in the fugure.

2

Literature review

In this chapter, dozens of papers are discussed which provide this study's background, general methods and inspirations. They are categorized as two groups: flood related and remote sensing related.

2.1. Flood and flood risk

Mitigating flood hazards is a never ending challenge in human history, which will be severer in the future. There are several other types of flooding:coastal flooding, fluvial flooding and pluvial flooding etc. Recent years a new type of flooding, compound flood, is raising awareness. It's the result of interaction between heavy precipitation and high sea level. At urban area storm runoff is fast and it often exceeds drainage system maximum ability. Storm surge not only challenges the coastal flood defenses, but also makes it difficult for river or drainage system to drain storm runoff. They are a highly dangerous combination so a real-time warning systems for timely preparation and evacuation is in great need. But in urban area, the complex surface features and large numbers of small-scale structure require high resolution of hydrological models(Henonin et al., 2013).

In the following several decades coastal flood defence system will be seriously challenged. The projected global mean sea-level rise at year 2100 ranges from dozens of centimeters to 2 meters (Rahmstorf, 2007, Sweet et al., 2007). Analysis from Hinkel et al. (2014) showed the coastal flood damage at 2100 is more sensitive to adopted flood defence strategy than variation in climate and socioeconomic. Therefore flood research and designing flood defence adaptively are of significant meaning.

Flood map is a useful tool in flood research and illustration flood information, which could be categorized into two types: flood hazard map and flood risk map(Nixon, 2016). The first one provides information about the magnitude and water depth while risk map presents the consequence such as casualties, economics lost. Government and researchers have been utilizing flood map for flood risk management. For example, EU Floods Directive required member states to prepare both kinds of map by March, 2014(Nixon, 2016).

The term "flood risk" is usually defined as the probability of flooding multiplying with the consequence. According to the type of consequence, there are social risk, individual risk and economic risk.

2.1.1. Probability in flood

Due to its natural properties, uncertainty is an intrinsic part of flood researches, and rational decision requires fully comprehension of this uncertainty. Unlike the deterministic forecast method, probabilistic forecasts are more scientifically honest and allow decision makers to utilise probability-based method(Lumbroso et al., 2009). A study was done at Rhine river at German section to investigate the probability of downstream levees breaching under the condition that upstream levees failed. Monte Carlo simulations showed that the breaching of upstream levees would reduce the probability of downstream levees' failure, but increase the chance of larger downstream discharge(Apel et al., 2006). This requires stakeholders to make judgement under the consideration of upstream and downstream situations.

Ensemble prediction system(EPS) is a widely adopted method in weather and flood forecast(Molteni et al., 1996). EPS means running on one or several models multiple times with slightly different initial conditions. The range of all results informs us the uncertainty of this prediction(, WMO). The European Centre for Medium-Range Weather Forecasts (ECMWF) is an example(Molteni et al., 1996).

2.1.2. Flood forecasting method

Traditionally hydrologic model is used for forecasting floods. There are several factors we can use to categorise hydrologic models(Devia et al., 2015). Whether the model considers time factor divides models into dynamic ones and static ones. The depth of incorporating physical process in model classifies models into empirical model, conceptual

model and physical-based model. The empirical model is fully driven by data and physical model is designed by human expertise to describe the physical mechanism. The conceptual model is in the middle of these two models. Most traditional hydrological models are physical-based or conceptual, for example, the classic rainfall-runoff model and one-dimensional drainage model(Henonin et al., 2013).

The sources of uncertainty in hydrologic model are input uncertainty, model uncertainty, measurement error etc. Most hydrologic models are deterministic, which can lead to poor judgement of decision makers. Krzysztofowicz presented the Bayesian Forecasting System(BFS) to quantify the uncertainty in hydrologic models, which decomposed the uncertainty into two parts: input uncertainty and model uncertainty, which are quantified independently and integrated into one output uncertainty. This uncertainty equals to the natural variability of the predicted result. In comparison to Bayesian Forecasting System, this study pointed out that Monte Carlo simulation does not actually give a probabilistic forecast due to the lack of hydrologic uncertainty processor and integrator. A detailed overview of the development of Bayesian Forecasting System could be found in study by Han and Coulibaly (2017). Real-time RS images proved to be useful for flood forecast. Researchers used ensemble Kalman filter(EnKF) to assimilate the water level observation(WLO) of SAR into hydrodynamics model to reduce forecast uncertainty(García-Pintado et al., 2015). It pointed out, upon the time when this study was conducted(year 2014), they didn't have high-resolution real-time SAR data source. While now researcher could obtain SAR image from Sentinel-1 within one hour after the image is taken, which enables the real-time flood forecast.

Researchers have used many probabilistic models in flood prediction such as logistic regression. Nandi et al. (2016) produced a flood hazard map for Jamaica using logistic regression and principle component analysis. DEM variables(elevation, slope angle, aspect, flow accumulation, direction and Topographic wetness index) are transformed by principle component analysis to three new component as logistic regression's input variables. The precipitation variable in this study is the annual precipitation amount, therefore this flood hazard map inform people about the probability of flooding regardless of time. The validation of this model used 338 locations as dataset with half as training dataset and other half as validation datasest. A flood susceptibility map is also generated by using logistic regression for an area in South Korea (Tehrany et al., 2013). One flood event's inventory consistent of 160 locations is used for prediction with other explanatory variables such as land use, curvature and soil characteristic. Predicted flood probability is divided into five classes to indict different levels of threat. This logistic regression forecasting achieved good performance with accuracy of 84.4% in training data and 88.64% in validation data.

Other probabilistic methods have also been applied in flood forecast. Bayesian Network(BN) is a probabilistic graphical model that builds on random variables and their conditional dependencies, which makes it suitable for predicting complex physical phenomenon like floods(Li et al., 2010).

2.2. Remote sensing and flood detection

The definition of remote sensing given by the United States Geological Survey is that: remote sensing is the process of detecting and monitoring the physical characteristics of an area by measuring its reflected and emitted radiation at a distance from the targeted (USGS). Its sources include sensors on airplane, satellites and sonar system on ships, and its products could be used in varies fields: hazard, glaciology, ecology and so on. Since remote sensing image could record the surface of a large area which makes it suitable for flood mapping with less human labour. Varies algorithms have been developed to detect flood accurately. Before describing the algorithms, types of remote sensing images should be introduced.

There are two main types of images: optical image and Synthetic Aperture Radar(SAR) image(Tupin et al., 2014). The first one is taken by optical sensor which measures solar light backscattered by the ground, so these sensors are called passive sensor. SAR sensor is an active sensor because it emits electromagnetic wave and receives the backscattered one for measurement. Hence SAR images have one obvious difference from optical ones: cloud, cloud shadow and hill shadow have small effect on SAR images since the electromagnetic wave could penetrate them.

This advantage makes SAR image suitable for flood area mapping. Different from water body delineation, flood detection has the requirement of timing. While water body delineation could avoid problems of clouds and shadow by utilising multiple optical images taken at different times, flooding could not be accurately mapped with bad atmosphere conditionDonchyts (2018), Verpoorter et al., Wang et al. (1999). SAR image provides the solution to this difficulty. The ability to take images during day and night without the interference of cloud enables SAR image wildly applied in flood management field. Chini et al. (2019)

As it is stated the persistence of cloud on remote sensing images excludes the possibility of employing optical images in this study, therefore Synthetic aperture radar images are used to perform the flood detection process.

2.3. Flood detection

The intrinsic of flood detection is water body detection which is an image classification problem. Several water body detection methods are commonly used(Lakshmi, 2017): (1) Visual interpretation, which is of high accuracy but at a cost of huge labour hours; (2) Spectral index, which is formulated via two or more wave bands from optical sensors images; (3) image classification, including decision tree, support vector machine and other machine learning method

(Mountrakis et al., 2011, Yang et al., 2018); (4) Physically based model and additional input data. Because water has a consistent temperature comparing to land, it is possible to use thermal image to distinguish water body. Texture analysis from radar data is another solution. Additional data could be DEM where altitude and position could serve as a threshold; (5)Change detection method. Previously dry location will exhibit differently in spectral, textual and thermal aspects. Simple subtraction will illustrate flooded area(Schlaffer et al., 2015). Which method to use should be decided by data availability and research objectives.

2.3.1. Threshold based on water index

Water index is the foundation of many RS image classification algorithms. Materials have different reflectances at different wavelengths. For example, water almost only reflects wave in visible wave bands, while soil and vegetation could reflect wave in all wave lengths, although in different patterns. Based on this, researchers proposed varies indices, which are mathematical expression of wave bands. Pixel values corresponding to interested object will fall into different zone comparing to other pixels. Sometimes researchers use more than one index to raise the accuracy(Yang et al., 2018). There are some widely applied indices for water body detection such as Normalized Difference Water Index(NDWI) and Automated Water Extraction Index(AWEI).

NDWI borrowed the idea from Normalized Difference Vegetation Index and it could tell water and land apart successfully. But its performance in urban area is not satisfying. Later Xu (2006) modified it into MNDWI, which could distinct water and land much more clear in urban area(Xu, 2006, Yang et al., 2018). The water index image could be segmented into two parts by a single threshold to extract water pixel.

Choosing the threshold is a crucial step for correctly mapping water area. Researcher used different mathematical algorithms to find the optimal one. Martinis et al. (2009) examined Global minimum thresholding, Quality-index thresholding and Kittler and Illingworth's algorithm. Other methods such as minimum valley bottom of the grey histogram, Otsu's threshold are also widely employed(Otsu, 1979, Yang and Chen, 2017).

2.3.2. Classification algorithm

Thresholding focuses on separating water from other types of surfaces, while researchers could use classification algorithms to tell varies objects apart. Anyway, many studies proved that classification algorithms perform well in detecting water body. Approaches that use training dataset are called supervised classification, such as Maximum likelihood, minimum distance, and decision tree classifier. While clustering algorithms require no pre-defined classes and label images based on inherent statistical information (Lu and Weng, 2007).

2.3.3. Change detection

Change detection method identify flooded area by comparing post-flood image with pre-flood image. When applying this method, reference images should meet several requirements: the same viewing geometry, polarisation configuration and backscatter signature as flood images(Schlaffer et al., 2015). At regions possessing distinctive seasonality, we should take images from same season to keep the condition of soil moisture and vegetation growth in an identical situation, because the backscatter coefficient is related to surface moisture. Schlaffer et al. (2015) performed a harmonic analysis to capture one region's seasonality which could help the researcher to perform change detection better.

2.3.4. Object based image analysis

One emerging RS image processing method is object based image analysis and it is often applied before classification(Malinowski et al., 2015). This method processes images on an object level instead of pixel level. Classification result performed at pixel level could have many speckles and noises, but after segmentation pixels are aggregated into objects, which could avoid the 'salt-and-pepper' noise problem. Image segmentation delineates objects by some certain criterion, whose accuracy has a large impact on the following classification result(Gao et al., 2011). There are several segmentation methods: global optimisation(Stewart et al., 2000), edge detection(Fjortoft et al., 1998), active contour model and region growing and merging(Mehnert and Jackway, 1997).

Seed region growing is one widely applied segmentation method. Bechtel et al. (2008).

2.3.5. Integration of RS and DEM

DEM is helpful for flooding delineation in RS imagesBrivio et al. (2002), Pradhan (2009), Y.Wang et al. (2002). Researchers mapped flood extent in North Carolina by using of both Landsat7 data and DEM(Y.Wang et al., 2002). First, they delineated flooded area using a single cutoff value in RS images, and another inundated area is produced by a DEM based on gauged data. Then two flood maps are merged to give the final result.

When incorporating additional data into flood inundation mapping, taking their accuracy and resolution into account is important. For example, vertical error of an old DEM could be as large as 22m, but high accuracy DEM is unavailable in many regions(Saksena and Merwade, 2015). To address this problem, Saksena and Merwade (2015) studied the relation between DEM's properties(vertical accuracy and horizontal resolution)and accuracy of flood mapping,

and they further used this result to generate flood inundation map with a finer resolution resampled from coarse resolution DEM.

But their inundation models were hydrologic instead of water body detection method. Anyway, it reminds us that we should examine the resolution of all inputs rather than only RS image.

Combination of these methods could lead to higher accuracy. Researchers carried a study for mapping all lakes in Sweden and formed the procedure into a system called GWEM(Verpoorter et al.). First they classified images from LANDSAT 7 by a multiple thresholding method which was enhanced by Principle Component Analysis and spectral brightness calculation. Next a decision tree classifier was trained by previously processed data and they marked 26 classes as water. Finally, noises were removed by texture analysis. This system applies several algorithms or indices to improve the final accuracy, which is 94.88%(overall accuracy) with a kappa value at 0.2.

2.4. Difficulties in flood detection

Using remote sensing image to detection flooded area has some conundrum, some of which only exist in flood detection while some other are common problems existing in all types of remote sensing image classifications. Understanding and solving these problems are essential for researcher to exploit remote sensing image more accurate.

2.4.1. Flood detection in built environment

Floods in urban area are usually quick and the built environment is of high surface complexity. These require both high spatial and temporal resolution for RS image.

A study was done to perform water detection in urban area which dealt with the overestimation problem by a noise-prediction method(Yang et al., 2018). They derived the noise by the difference between two water indices and used supervised classification to divided data into two classes. Threshold values for eliminating noise were arrived by Constrained Energy Minimization method. This algorithm showed a better performance especially on User Accuracy(UA) comparing to AWEI index method and Support-Vector Machine methods.

2.4.2. No real-time image

Due to lack of resource, for most flood events around peak there are no satellites taking images. However, some RS images are taken at a certain period after the flood peak, when some flood have already gone, then it is suggested to adopt the multi-sensor method, which is estimating flood extent by images from other sensors. Brivio et al. (2002) gave a new solution which was integrating RS data with GIS. Their method was based on a concept called: least accumulated cost path. The images were performed with a simple threshold approach and the least accumulative cost distance method. The results reached a true positive accuracy of 96.7%. However, the applicable range of this method is not clear, such as land-use(urban and rural) , data source. Also, the accuracy of DEM might effect the final result significantly. These are methods for delineating flood extent without real-time images.

At some times we have images which record the flood peak, but their spatial resolutions are low. Because a trade-off exists between temporal resolution and spatial resolution, satellites and sensor systems designed for high temporal resolution and larger coverage is of low spatial resolution. Vice versa the revisit time is relatively long for high spatial resolution satellites(Lakshmi, 2017). In the case of only low-resolution images available at flood peak, a study done by Zhang et al. (2014) in 2014 used both Landsat and MODIS images to map the flood extent. The algorithm takes advantage of MODIS's high temporal resolution and Landsat's high spatial resolution. Therefore even if there are no high spatial resolution sensors passing-by when a flood is happening this method could still give flood image with high spatial resolution.

Rerouting satellites when detecting hazard events is an ideal method. One NASA program operated a real-time flood detecting and monitoring experiment on the EO-1 Hyperion instrument. On-board science analysis algorithm performs change detection, and if it detects the onset of flood, it will autonomously re-plan route to take images. The images will only be downlinked when flood happens. This approach could filter unwanted information, but it is still limited by cloud and spacecraft's orbital cycle. Researchers operated a similar study to perform flood monitoring better, but instead of using flood onset detection algorithm, they chose flood forecast to trigger the recording(Boni et al., 2016).

2.4.3. Flood detection in vegetated area

Mapping floods in vegetated area could be challenging because inundated vegetation changes the spectral signature of open water. Grass and maize increase water surface's roughness and reduce its reflectance(Malinowski et al., 2015). High vegetation forms a canopy that prevents sensor from detecting water. Aiming at wetland vegetation, Malinowski et al. (2015) employed a decision tree which classified land surface using varies indices combined with Principle Component Analysis(PCA) and topography information. They tested two approaches: object-based image analysis and pixel-based analysis, and the former method resulted in a better accuracy than pixel-based one. This study is useful for flood detection on riverplain but because the training data are from on site up-to-date photos it is difficult to operate over large space or long time span.

2.4.4. Computation in cloud environment

One difficulty of RS image processing and analysing is the large size of data. This poses great requirements for hardware and software. Cloud computation is a nice solution to this. Cloud computation is a large scale distributed computing paradigm. It provides on-demand computing functions and services to customers by the Internet(Duan et al., 2012). Cloud computing includes three classes: Infrastructure as a service, Platform as a service and software as a service. A developer using platform as a service can enjoy a development platform with services and storage with affordable hardware or software.

Google Earth Engine is one cloud-based platform specifically for earth geospatial analysis that enables researcher to access varies types and large quantities of satellite data and fast computation (Gorelick et al., 2017). It stores many widely used earth-observing datasets, such as Sentinal-1, Sentinal-2 and all Landsat archive. This imagery covers climate, environment, geophysical, socio-economic aspects. It also allows customers to upload their own data and process on its platform. Images provided by Earth Engine are pre-processed for fast access and computation. Earth Engine also comes with a high-performance, intrinsically parallel computation service. Its data distribution model and system architect are also designed for efficiency.

3

Study area and data

In this chapter, the background of this research is introduced, which are information of study areas and data descriptions. Understanding flooding characteristics of study area is essential for correctly selecting key elements in flood modelling and constructing the model. It is also crucial to guarantee that data used in modelling are of high credential and they are properly processed. The data includes two part: remote sensing images and flood conditioning factor.

3.1. Study area

Two study areas are chosen for this study, both of which sit at the United States. The first one is located at southeast coast of Louisiana State. The area crosses Jefferson parish and Orleans parish. For simplicity the area is referred to as New Orleans area in this study. The other one is at Florida State, which covers a part of Miami Dade county with the centre at Miami Beach area. The types of flood studied at two locations are different, even though they both are seaside cities suffering from hurricanes. At New Orleans, flood events I considered are caused by heavy rainfall, while at Miami flooding under investigation is caused only by high tides. More exhaustive details about these two areas and their flooding are given in the next sections.

3.1.1. New Orleans

New Orleans sits at the estuary where the Mississippi river meets the Gulf of Mexico. The city is surrounded by Lake Pontchartrain, Lake Borgne and shallow shoal with Mississippi river running through the city, so both coastal flooding and fluvial flooding are threatens to it. Several factors are closely related to flooding mechanism at New Orleans.

Elevation

The elevation of New Orleans is often said to worsen this city's flood situation, which is described as a 'bowl'. Its elevation is shown in figure 3.1a and the average elevation of the study area is 3.5m. The elevation along the Mississippi river is higher than the surrounding area which is caused by sediment from historical flooding events(Rogers, 2008). Figure 3.2 illustrates the process which is common for the downstream section of Mississippi river. This high elevation along the Mississippi river acts as one side of the 'Bowl'. The other side is sea dike at the side of Lake Pontchartrain. In the middle of the bowl runs the Ridge Gentilly causing a rise in elevation. Aside from the river levee and sea levee, the whole New Orleans area is about or under sea water level, which makes the risk of coastal flooding extremely high and the consequence disastrous. However, the high risk of storm flooding at New Orleans is not only affected by low elevation, but also the shape of 'Bowl'. Due to high elevation around the city's periphery, instead of discharging storm runoff into the sea or river by gravity, rainfall tends to stay in the lower area causing standing water. The fact that New Orleans is also sinking is other reason of exposing it to high flood risk(Dixon et al., 2006)(V. et al., 2001). Varies studies show that New Olreans' elevation has been sinking for decades which in combination with sea level rising poses this city to increasing danger of flooding.

Flood defence system

Due to New Orleans' geographic location and topography, it has been suffering from both coastal and storm flooding for a long time, so a sound flood defence system is essentially important. After hurricane Katrina in 2005, which inflicted huge damage on New Orleans, its flood defence system was under fully survey, re-evaluation and upgrade. Now the flood defence system at New Orleans is designed to protect against a 100-year event, which consists of several dike rings closing the city from Mississippi river and sea (see figure 3.3) and drainage system.

The drainage system in New Orleans includes pump stations, outfall canals and closure gates. It went through two phases of construction after hurricane Katrina. The first one which was used temporarily for protecting the city

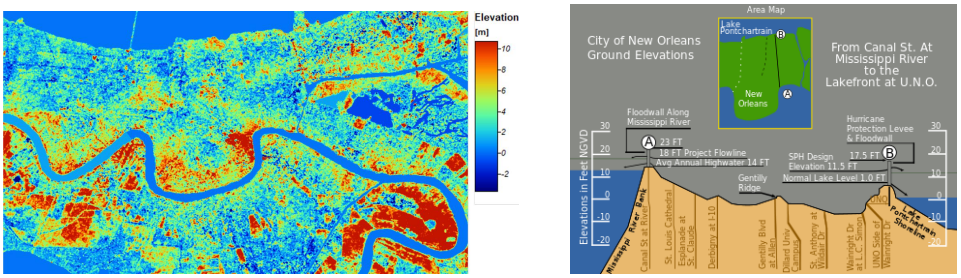

(a) Elevation of New Orleans

(b) Cross section of New Orleans (Wikipedia)

Figure 3.1: Topography of New Orleans

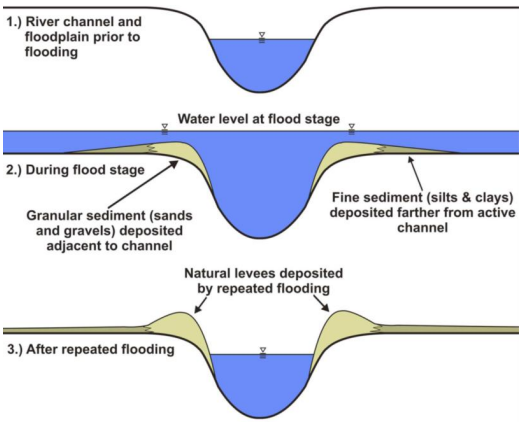

Figure 3.2: Sediment deposition along Mississippi riverside(Rogers, 2008)

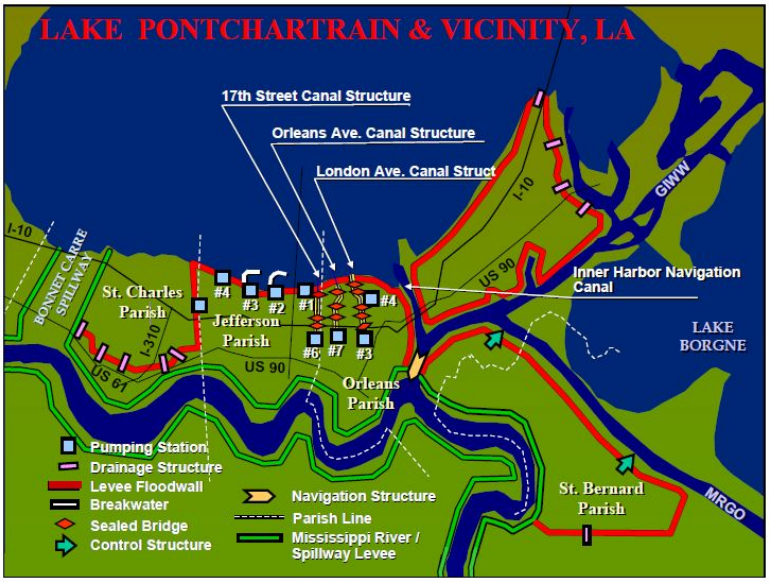

Figure 3.3: Flood defence system in New Orleans

before 2006 hurricane season is called Outfall Canals with Interim Closure Structures, and the second phase is called Permanent Canal Closures and Pumps (PCCP), which was finished at 2018.

The drainage system at New Orleans is operating at several stages, which is shown in figure 3.4. Due to the lower in the middle area, higher in the periphery topography, New Orleans needs to pump water in both canals and low elevation area out. There are dozens of small pump stations in New Orleans which are corresponding to step 1 in figure 3.4. They are in charge of keeping roads dry by pumping water into pipes and culverts, from which water is further discharged into canals. Closures and flood gates control the water level of canals. If both water levels of canals and sea are high, gates will be closed, and high power pump stations will drain water from canals to sea.

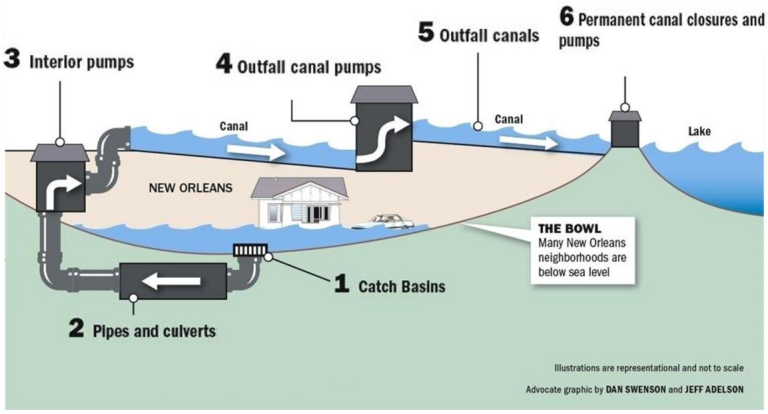

Figure 3.4: Operation of drainage system in New Orleans(Swenson and Adelson)

Study flooding event's characters

Flooding caused by breached levee is very different from flooding without levee failure, so this study only consider flooding events causing solely by heavy precipitation. For a seaside city at the mouth of a major river like New Orleans, it faces the risks of river flooding and coastal flooding. Sitting at the Gulf of Mexico, the hurricane is another source of flooding for New Orleans. When studying floods at New Orleans, the cause of flooding should be identified to narrow down relative variables. For flooding caused by precipitation, drainage system is the most important flood protection methods. Since the flood defence system was upgraded after hurricane Katrina, flooding events that happened before 2005 are excluded.

3.1.2. Miami

Another study area Miami is also a city along the seaside. It sits at the south tip of the Florida peninsula. The study area is an area of the Miami-Dade county with the centre at Miami Beach. Between the Miami beach and downtown Miami it is Biscayne Bay.

Miami sits on a plain with a low and flat elevation as it is shown in figure 3.5. Miami City and Miami Ceach do not have sea levee to protect from them coastal flooding. The average elevation of Miami beach is only of 1.3m above mean sea level which renders it susceptible to coastal flooding. Study reveals that due to sea level rise the risk of coastal flooding at Miami is increasing.

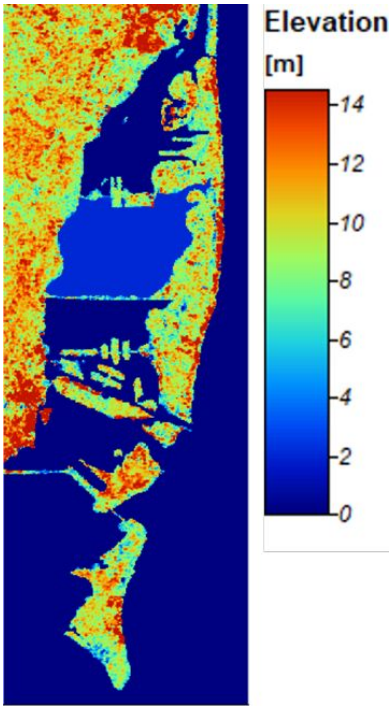

Figure 3.5: Elevation of Miami

Similar to New Orleans, Miami suffers from both coastal flooding and storm flooding. This study puts the focus on coastal flooding introduced by high tides. In recent years 'King tide' has been rising people's attention in Florida state

because every year several flooding events happened and obstructed people's daily lives. By Florida state's definition, king tide refers to high tides introduced by moon and sun aligning, when the combined gravitational force exerted by both celestial bodies are at the largest point(Román-Rivera and Ellis, 2018). At Miami, the king tide happens around September-November, and each time it lasts from three days to a week. Researchers noticed that sea level rising makes sea level at high tide higher(Wdowinski et al., 2016), which makes the risk of coastal flooding much higher. Flooding records used in this study also shows the frequency of coastal flooding raised. According to NOAA's storm event database from 2003 to 2012 no coastal flooding was recorded, but since 2012 frequency of coastal flooding kept climbing. These coastal flooding events are study objects of this research.

3.2. Description of satellite missions and products

Images exploited for flood detection are from three C-band satellite missions: Sentinel-1 and Radarsat-1/2 and two X-band missions:TerraSAR-X and COSMO-SkyMed. These satellites are all commercial missions except for Sentinel-1 which is free to the public. Images from four commercial missions are acquired through applying to the European Space Agency.

Sentinel-1 The Sentinel-1 mission is the European Radar Observatory for the Copernicus joint initiative of the European Commission (EC) and the European Space Agency (ESA)(Agency, b). There are two satellites on its orbital plane: Sentinel-1A and Sentinel-1B, which launched on April, 2014 and April, 2016 respectively. It provides all-weather radar image of the whole earth on a bi-weekly basis and its minimum spatial resolution is 5m. It is worthwhile to notice that all data from SENTINEL program are open and free to all users, no matter for what purposes. And products of SENTINEL program are available by online distribution platform within 24 hour of observation. Products from Sentinel-1 are of high resolution and revisit frequency, but since it has only been operating for about 4 years, there are few flood events recorded in the database.

Radarsat1/2 Radarsat-1 mission, operating from November, 1995 to March, 2013, was a Canadian-lead project to provide earth observation data for Canada and the world. Being active since 2007, Radarsat-2 mission is a collaborative project between Canadian Space Agency and MacDonald, Dettwiler and Associates Ltd.. These two missions have the same ground track and a repeating circle of 24 days. The highest spatial resolution for Radarsat-1 is 8m while Radarsat-2 reaches a resolution of 1m*3m at spotlight mode.

TerraSAR-X TerraSAR-X is a German satellite mission which is supported by the German Ministry of Education and Science(BMBF) and owned and managed by German Aerospace Center(DLR). On the basis of a public-private partnership agreement, EADS Astrium GmbH funded a part of the mission in exchange of the exclusive commercial exploitation right of mission's product. At the beginning of 2008 the mission started its operation officially. Its nominal revisit period is 11 days and the finest resolution is 1m by the high resolution spotlight mode. In 2010 Tandem-x was launched. Two satellites formed a TanDEM-X/TerraSAR-X constellation for the purpose of generating a global, consistent, timely and high-precision DEM.

COSMO-SkyMed COSMO-SkyMed (Constellation of Small Satellites for Mediterranean basin Observation) is a constellation composed of four satellites equipped with Synthetic Aperture Radar operating at X-band. It is conceived by ASI (Agenzia Spaziale Italiana), and funded by the Italian Ministry of Research (MUR) and the Italian Ministry of Defense(MoD), Rome, Italy. The first satellite was launched in June 2007 and the full constellation is completed by the end of 2011. Each satellite has a revisit time of 5 days but the whole constellation could shorten the time to a couple hours of a global level. Its highest spatial resolution is 1m by the spotlight mode.

3.3. Data on flood conditioning factors

Factors that are related to flooding are considered model input which include precipitation, sea level, elevation, distance to permanent water and drainage capacity. But it is different for two study areas due to varies causes of flooding. Before moving to sources of data and their processing methods, a common grid system is presented which is the foundation of data processing and the probabilistic model.

3.3.1. Standardisation of data

A common grid system is created for both study areas, by which data are standardised. Study areas are gridded into rectangular cells, and detection result and auxiliary data will be resampled into these. Furthermore, the probabilistic model is trained using this grid system, where each cell is a forecast unit.

Since the grid system determines the forecast model's spatial resolution, so it is of great importance to choose a reasonable grid size. The size should be small enough to describe different objects. For example, a street and the building next to it shall not be covered in one cell. But if choosing a size too small, it will put an extremely high demand on computational power. The World Geodetic System used is WGS84 and the resolution in this study is 0.0001° in

both latitude and longitude direction, which is about 10m in both directions. This is of the same magnitude of urban structures' measurements. But the area of each cell is of small difference due to the earth's figure. But the study area is small enough so the difference is neglectable. The largest difference between two cells' side lengths is 1.93cm at New Orleans area and 2.17cm at Miami area which is only 0.2% of cell's side length. So all cells in one study area are considered as uniform size.

After constructing a proper common grid system, auxiliary data are sampled and interpolated based on the grid system.

3.3.2. Precipitation

Only for New Orleans study area precipitation is included as an input of model, since flood type studied at Miami is tidal coastal flooding whose generating mechanism does not concern with precipitation. Precipitation data is gauged data from local weather stations. Although it could also be obtained from radar, however, its access is limited. Therefore precipitation data are obtained from three weather stations in the vicinity of New Orleans by the access of NOAA's National Centers for Environmental Information (NCEI), Local Climatological Data (LCD) Dataset. They provide rainfall and other weather data at an one-hour frequency. Weather stations' name and location are given in figure 3.6a, and stations' ID and data length could be referred to table 3.1.

(a) New Orleans station

(b) Miami station

Figure 3.6: Name and location of stations

Table 3.1: Location and data length of weather station and sea level station in New Orleans

Weather Station					
AOI	Station	Station ID	Latitude	Longitude	Data Length
New Orleans	Alvin Callender Field	WBAN:12958	29.8127	-90.0167	2006-Now
	Airport	WBAN:12916	29.9969	-90.2775	2003-Now
	Lakefront airport	WBAN:53917	30.0494	-90.0288	2004-Now
Sea Level Station					
AOI	Station	Station ID	Latitude	Longitude	Data Length
New Orleans	Carrollton	8761955	29.9333	-90.1350	2009-Now
	New Canal	8761927	30.0267	-90.1133	2006-Now

There are three weather stations near the New Orleans study area, giving three records for each flooding event. In total there are 12 flooding events, which means 12 precipitation records at each station. After obtaining raw precipitation data a time period needed to be defined. Only when rain falls between that period it is assumed effective in causing the flooding. The period is defined as 36 hours before the remote sensing image was taken. A weight is given

to the precipitation for considering time effect in flooding, which is linear to time. The rain that falls 36 hours before the image was taken has a weight of 0, while the rainfall happen right at the moment of the image being taken has a weight of 1.

Next step is interpolating three stations' accumulated precipitation amount for each event using the grid system defined in the previous section so that each unit in the probabilistic model has its precipitation input. The interpolation method applied is Inverse Distance Weighting, which calculates the value of each point based on its distances to reference points(Known points). The formula of Inverse Distance Weighting is given as:

$$Z_j = \frac{\sum_{i=1}^{n} \frac{Z_i}{d_{i,j}^p}}{\sum_{i=1}^{n} \frac{1}{d_{i,j}^p}}$$

Where:

Z_j: value at interpolated point j;

Z_i: value at interpolating (known) point i;

$d_{i,j}$: the distance between point i and point j;

p: power parameter, which is a positive real number.

n: total number of interpolating(known) point.

As we can see from the formula3.3.2, a closer distance from a point to one reference point means a smaller $d_{i,j}$, or a larger $\frac{1}{d_{i,j}^p}$. In other words, a closer reference point has a larger weight on the interpolated point. This is in consistence with rainfall distribution pattern, so this interpolated result is used as the approximated precipitation. One example of interpolation result is illustrated in figure 3.7 which is interpolated precipitation of flooding event that happened at 3rd, April, 2012. Weighted precipitation at three weather stations are: 50.27mm, 24.31mm and 0mm. West and north area which are close to stations that received a large amount of rainfall were assigned with a higher value than east and south area.

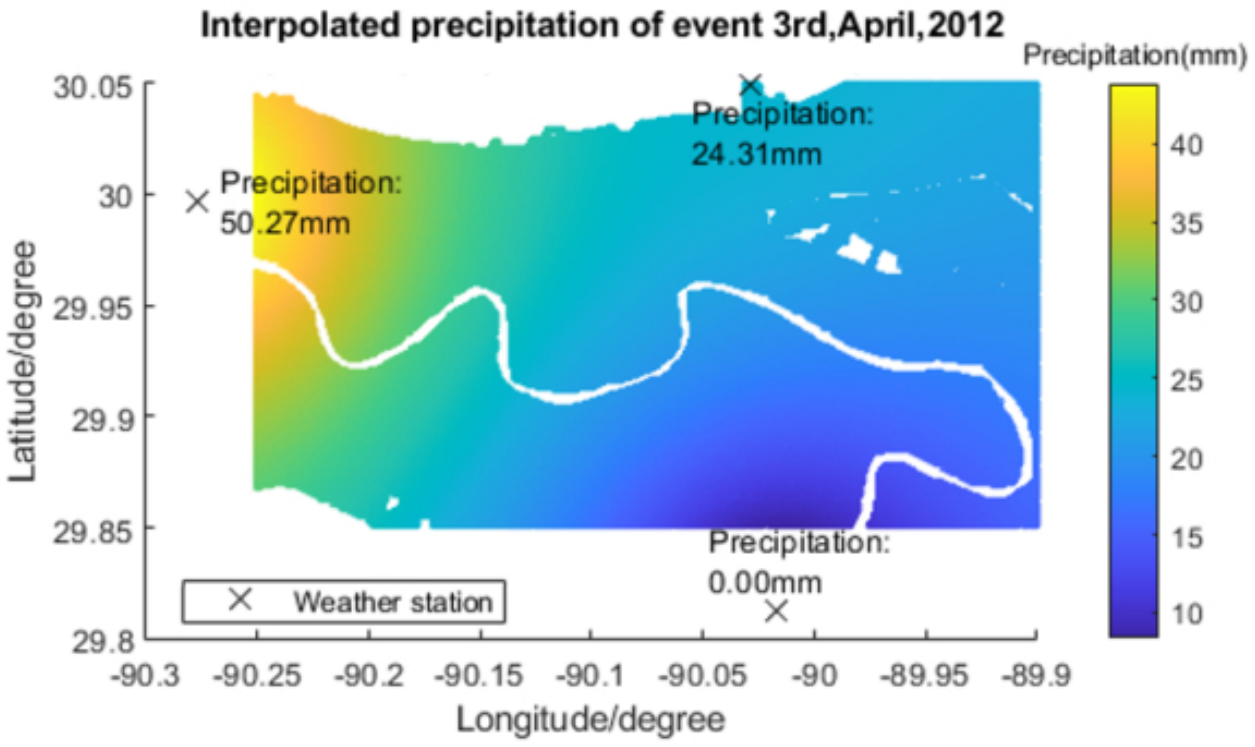

Figure 3.7: Interpolated precipitation of event 3rd, April, 2012

3.3.3. Sea level

Sea level data is obtained from NOAA's Center for Operational Oceanographic Products and Services (CO-OPS). It provides real-time water level information which is updated every 6 minutes. Two water levels stations are set in New Orleans area and one at Miami area. Locations and names of sea level station could be referred to as figure 3.6b and table 3.1.

For both study areas, sea level is a crucial variable but for different reasons. At Miami study area, since study flooding events are coastal flooding caused by high tides, sea level is the driven force of flooding. But at New Orleans,

sea level affects flood extent by impeding the drainage stations' pumping efficiency. Because the city is surrounded by a dike ring which did not breach once during all flooding events under consideration, water could not flow from the sea or river into the road. But due to New Orleans' topography, stormwater relies on its drainage system to drain, and a part of the drainage system's capacity is affected by sea level.

When pumps are at work, the head difference between the suction head and the discharge head is in a negative relationship with discharge. For storm water drainage, it means the larger water level difference between canal and sea is, the smaller the discharge will be. Therefore a higher sea level will result in a lower discharge flow rate of the drainage system, so this study includes sea level as a flood conditioning factor in the New Orleans flood extent forecast model.

3.3.4. Elevation

The elevation of both study areas is derived from NASA Shuttle Radar Topography Mission(SRTM) data sets (NASA), whose original resolution is 30 metre. I interpolated the elevation to the common grid system by Delaunay triangulation method. Figure 3.8 shows the interpolated elevation.

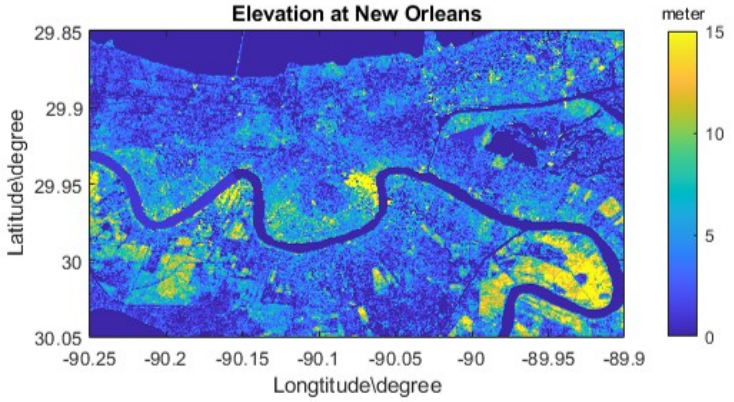

(a) New Orleans elevation

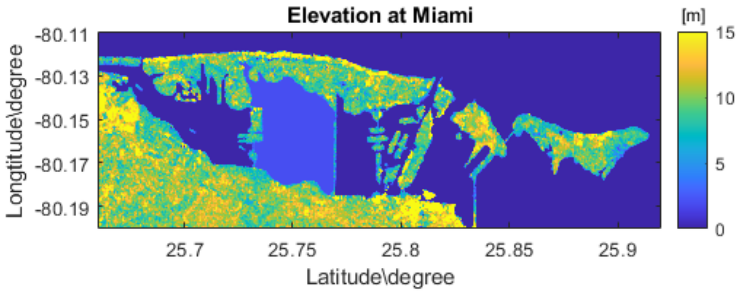

(b) Miami elevation

Figure 3.8: Interpolated elevation

Two study areas' topographies and how they interact with flooding are discussed at further details in sections 3.1.1 and 3.1.2.

3.3.5. Distance to permanent water

Each cell's shortest distance to permanent water is calculated and included as one flood conditioning factor in the model. The periphery of the water area is obtained from OpenStreet map(OpenStreetMap contributors, 2020). At Miami area, permanent water is mainly sea, therefore this variable informs us about how close one cell to the sea is, which obviously affects the chance of one location being flooded during high tides. At New Orleans area, permanent water includes sea, rivers and many canals. Distance to water area are shown in figure 3.9.

3.3.6. Drainage capacity

The drainage capacity across the New Orleans area is included as one input. Due to New Orleans' topography, storm water heavily relies on the drainage system to flow out. There are dozens of pump stations functioning at New Orleans and Jefferson Parish. Drainage stations' locations and capacities are obtained from Jefferson Parish Drainage Department homepage(Jefferson Parish) and Sewage and Water Board of New Orleans homepage(Sewerage and of New Orleans). And new installations of drainage stations during the study period are also recorded. The drainage capacity of the whole study area is arrived by Inverse Distance Weighting interpolation based on the common grid system in a similar way as to how precipitation data is interpolated. Since one drainage station only has an

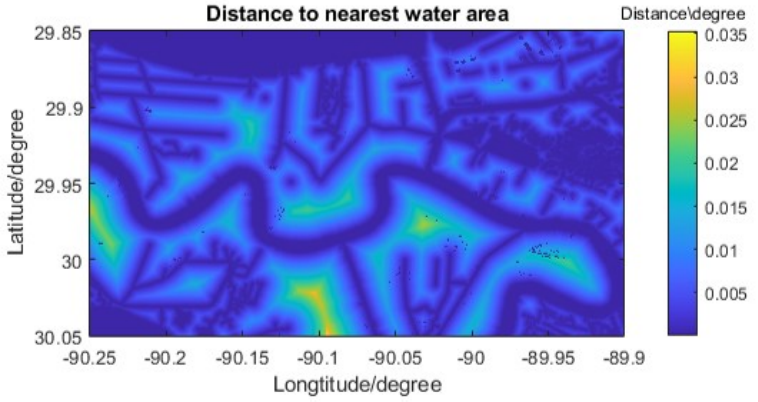

(a) New Orleans

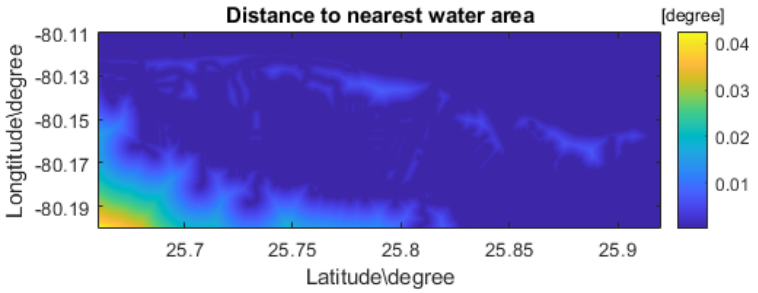

(b) Miami

Figure 3.9: Distance to permanent water area

influence on its surrounding area, each station is assigned with a search radius, which means one station only has an influence on locations that are within circle enclosed by its search radius. This search radius varies for stations of different scales. For stations with a capacity larger than 1000cfs, the search radius is 800 grid lengths or about 8km. For those smaller than 1000cfs, the radius is set about 4km. The interpolation result is shown in figure 3.10.

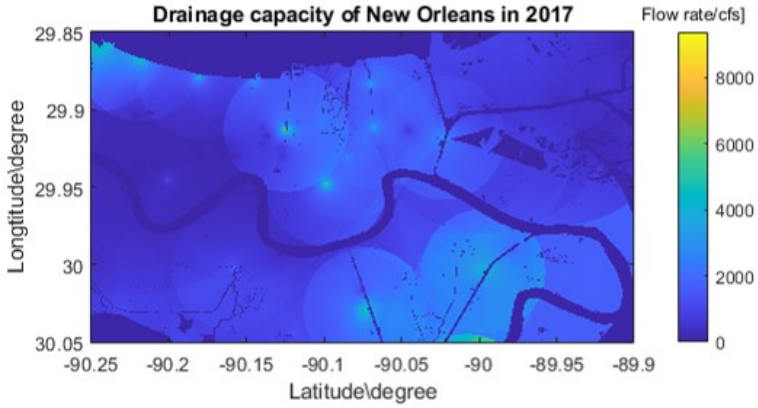

Figure 3.10: Interpolated drainage capacity of New Orleans in 2017

4

Methodology

In this chapter algorithms and methods applied in this study are introduced. It contains two parts: flood detection and flood forecasting model. Flood detection section describes algorithms of processing remote sensing images. The second part presents the probabilistic flood extent forecast model, where the model's structure, probabilistic model and model evaluation methods are discussed.

4.1. Flood Detection

In this section, methods for mapping flood extent are described step-wise. All images analysed for flood detection are products from SAR sensor. Because pluvial flooding is caused by heavy precipitation, cloud usually presents on optical satellites images blocking ground area. As it is mentioned before that SAR(Synthetic-aperture radar) image is not affected by clouds, this study only makes use of SAR images for flood detection. Methods and algorithms are developed for both single-spectral image or multi-spectral image. Since Synthetic-aperture radar only measures in one wave band, algorithms given below are based on the presumption that they are applied to single-spectral image. Flood detection processes are performed on SAGA(Conrad and Böhner, 2015), an open-source GIS software. Algorithms are pre-wrote in this software which allows user to set desired parameters and process remote sensing images.

4.1.1. Object-based image analysis

The first step of flood detection process is called object-based image analysis which subdivides the image to an object level before next step. After segmenting images to objects, it could avoid the salt-and-pepper problem which commonly exists in pixel-level analysis. The segmenting method applied is called Seed Region Growing.

The general idea of Seed Region Growing is planting seeds in the image and allowing them to grow and merge adjacent pixels into polygons which fit closely together without gaps(Adams and Bischof, 1994, Böhner et al., 2006, Mehnert and Jackway, 1997). Values of pixels within one polygon must satisfy several criteria by which new pixel is decided to be merged into one polygon or not. Selecting which pixels as seeds is crucial since it affects final segmentation result greatly. SAGA uses the semi-variogram analysis in selecting suitable seeds(Böhner et al., 2006). Semi-variogram $\gamma(h)$ is a function for describing how data is related to spatial distance. It is defined as half the average squared difference between points Z_i and Z_j separated at distance h. For a 2-dimensional spatial data, $\gamma(h)$ is expressed as:

$$\gamma(h) = \frac{1}{2|N(h)|} \sum_{(i,j)\in N(h)} (Z_i - Z_j)^2$$

Where:

$\gamma(h)$: semi-variogram;

h: distance;

$N(h)$: set of pairs of points which are separated by distance h;

$|N(h)|$: number of pairs of points in set $N(h)$;

In practice, we can calculate the empirical semi-variogram by:

$$\gamma(h \pm \delta) = \frac{1}{2\,|N(h \pm \delta)|} \sum_{(i,j)\in N(h\pm\delta)} (Z_i - Z_j)^2 \tag{4.1}$$

Where:

$h \pm \delta$: distance h plus or minus bin width tolerance δ.

An example of semi-variogram is given in figure 4.1 :

In figure 4.1, dots represents results calculated by formula 4.1. For further application, empirical semi-variogram is usually fitted to one of semi-variogram models, such as spherical variogram model and exponential variogram model.

Spherical variogram model:

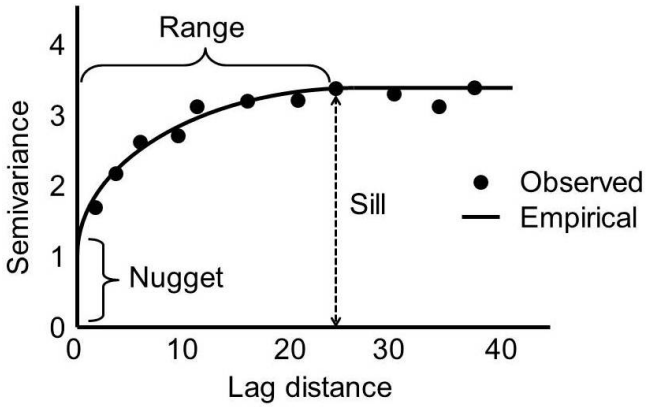

Figure 4.1: Semi-variogram example(Biswas and Si, 2013)

$$\gamma(h) = \begin{cases} (s-n)(\frac{3h}{2r} - \frac{h^3}{2r^3}) + n & h \leq r \\ s & h > r \end{cases}$$

Exponential variogram model:

$$\gamma(h) = (s-n)(1 - exp(\frac{-h}{r})) + n$$

Where: s is the sill; n is nugget and r is the range. Range is the distance that the semi-variogram flattens out, within which two points are related. Nugget is the intercept of semi-variogram with the y-axis and sill is the maximum value of semi-variogram when distance reaches infinity. Unknown points' value could be interpolated by using fitted variogram model.

After computing the semi-variogram function, SAGA continues calculating the spatial representativeness by inverse distance weighted mean g_v whose function is:

$$g_v = \frac{\sum_{i=1}^{m} \frac{\gamma_i}{h_i h_i^p}}{\sum_{i=1}^{m} \frac{\gamma_i}{h_i^p}}$$

Where:

g_v: inverse distance weighted mean, which is all semi-variance gradients with distance from h_1 to h_m with the weights $\frac{1}{h_1}$ to $\frac{1}{h_1}$ powered by p.

By this g_v, metric representativeness r_c is defined as a mean distance in which a pixel does not vary much from neighbouring pixels. This distance is determined as half of global variance V_m being reached:

$$r_c = \frac{v_m}{2g_v}$$

One image results in a matrix of r_c where each pixel is with a representativeness value. A local representativeness maxima suggests the centre of a homogeneous area and minimal indicates pixel-lineaments. This procedure described above serves to plant suitable seeds for the segmentation. After selecting seeds by applying representativeness analysis, criteria of homogeneity and heterogeneity are required for region merging.

Figure 4.2 is an example of segmentation. The upper image is an area cut from an raw image taken by CosmoSkyMed mission. This area covers a part of Mississippi river and its river bank. Dark blue area corresponds to the river, red rectangular shapes on the river are ships, and in the lower left corner is river bank where buildings are identifiable. The lower image presents the result of image segmentation. Ships, riverbank and river are distinctively delineated. Every image of flood events was performed with this segmentation, which enables the next step classification to have a better performance.

4.1.2. Supervised classification

Supervised classification algorithms is applied to classify objects created by segmentation, which operates in the following steps:

1. Decide the image's land-use compositions into which objects will be classified, for example, water, grass and urban buildings.

2. Select and label training data which represent each class. Field trips, aerial images or other data source could help choose training data set. In this study optical remote sensing images are used in identifying land-use.

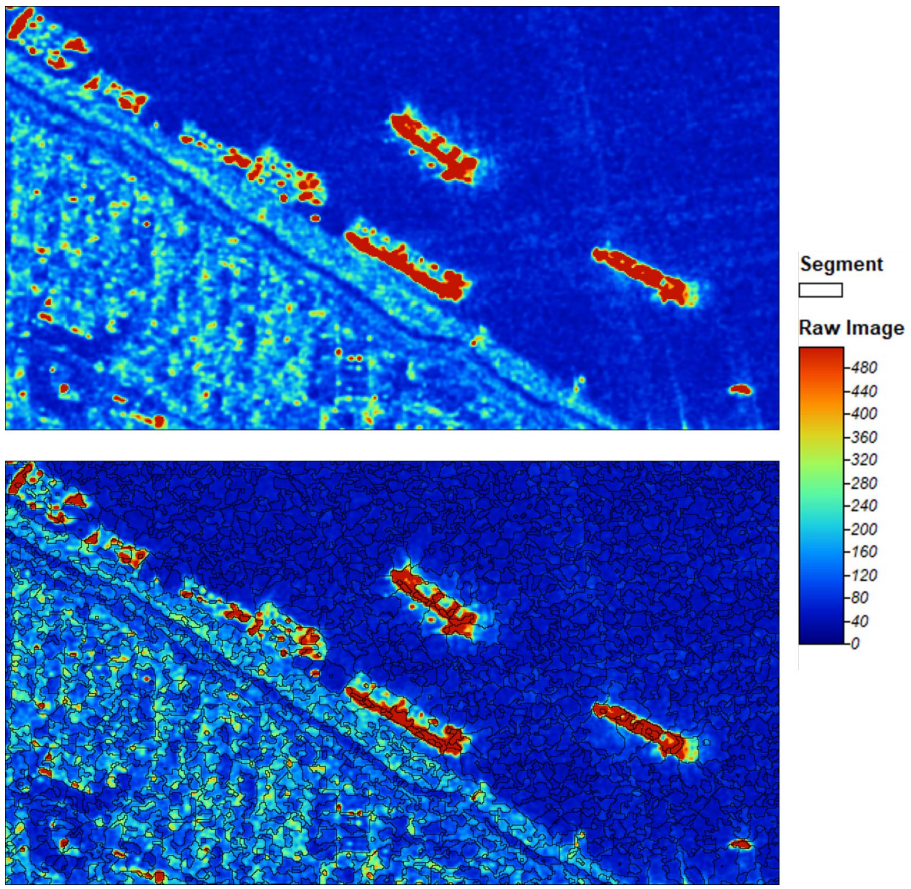

Figure 4.2: Example of object based image analysis

3. Estimate the parameters of classifier algorithm by training data set.

4. Classify every object into one of the desired land-use types using a trained classifier.

Various algorithms were developed for step 3. In this study, two algorithms are compared using a test image and the more accurate algorithm is chosen to perform flood detection on all images. Both methods are widely applied: maximum likelihood and minimum distance classification. Their difference lies in how they exploit the training data.

Maximum likelihood classification

Maximum likelihood classification assumes that statistics in each class follow a normal distribution and it applies Bayes's theorem for decision. First each class's normal distribution is estimated using training data. Then the probabilities of one object belonging to all classes are calculated by Bayes's theorem. Each object is assigned to a class that has the highest probability among all classes. When a threshold is specified, if one object's highest probability is lower than the threshold, that object will remain unclassified. Otherwise the algorithm will label every object to a class. The classification rule is expressed as:

$$x \in \omega_i \text{ if } p(\omega_i \mid x) > p(\omega_j \mid x) \text{ for all } j \neq i$$

where:

$p(x \mid \omega_i)$: the posterior probability of object x belonging to class ω_i.

ω_i: spectral classes where $i = 1, 2, ...M$ with M being the number of classes;

$p(\omega_i \mid x)$: the conditional probability of object x belongs to class ω_i, or probability density function.

To calculate the desired $p(\omega_i \mid x)$ Bayes' theorem is used:

$$p(\omega_i \mid x) = \frac{p(x|\omega_i)p(\omega_i)}{p(x)} = \frac{p(x|\omega_i)p(\omega_i)}{\sum_{i=1}^{M} p(x|\omega_i)p(\omega_i)}$$

Therefore the classification rule could be written in:

$$x \in \omega_i \text{ if } p(x \mid \omega_i)p(\omega_i) > p(x \mid \omega_j)p(\omega_j) \text{ for all } j \neq i$$

The $p(x \mid \omega_i)$ and $p(\omega_i)$ is given by the information of image and training data. After properly choosing training data and estimating classes' distributions, the algorithm could label all objects.

Minimum distance classification

Minimum distance classifier is faster but simpler comparing to maximum likelihood classification. In maximum likelihood classification each class is modelled with a normal distribution using training data while minimum distance classification method estimates classes by the mean m of classes' statistics. The aim is to minimise the distance between object's value and the class in the feature space. The discriminant function is as follows:

$$x \in \omega_i \text{ if } d(x,m_i)^2 < d(x,m_j)^2 \text{ for all } i \neq j$$

Where:

m_i: the mean of class i which is calculated by training data.

$d(x,m_i)^2$:squared distance, generally being euclidean distances whose expression is:

$$d(x,m_i)^2 = (x-m_i)^2$$

When applying minimum distance classifier to one single image, training data gives each class a mean value m_i, so it is suggested that minimum distance classification's performance is better when is is applied to multi-spectral image where each class equips with a vector of mean **m**.

Selection of supervised classification algorithm

In view of these two algorithms' principles, we might guess that maximum likelihood classifier will surpass minimum distance. One SAR image could only provide one mean m to each class when applying minimum distance classifier, which might not be sufficient enough for the classifier to discern classes accurately. To examine this hypothesis and decide on a better algorithm to perform flood detection, these two methods are used on one test image which was taken during the dry period. Because of lacking flood extent record these methods are tested by detecting permanent water area and validating the result against open water area from Openstreet map(OpenStreetMap contributors, 2020). The test image is a SAR image from Sentinel-1 mission which was taken at 31st, Dec., 2018 around New Orleans area. According to precipitation record, there was no precipitation received in all three weather stations during previous days so it is fair to expect that detected water area should be consistent with permanent water area extracted from Openstreet map. The raw test image is shown in figure 4.3a, of which area detected as water is compared with a reference map given in figure 4.3b to determine two classifier's accuracy.

Confusion matrix and index To present and compare the performances of these two classification algorithms, confusion matrix and some indices are used. Table 4.1 is a confusion matrix paradigm for classifying water and land.

Table 4.1: Confusion Matrix for Water Detection

		True Value	
		Wet	Dry
Predicted Value	Wet	True Positive (TP)	False Positive (FP)
	Dry	False Negative (FN)	True Negative (TN)

In the table, each column corresponds to a class of the actual data, and each row represents a class of the predicted result. If one location is labelled as water either in a reference map or detection result, it is said as positive(P). Negative(N) means it is labelled as dry. When the detection result agrees with a reference map, it is marked as a true(T) data point otherwise it is a false(F) one. For example, one location that is detected as water from the satellite image, but it is recorded as dry from flood report, it is a false positive(FP) point. There are several indices for evaluation that are calculated based on a confusion matrix.

Accuracy:

$$Accuracy = \frac{(TP+TN)}{(TP+FP+FN+TN)}$$

Precision:

$$Precision = \frac{TP}{(TP+FP)}$$

Sensitivity:

$$Sensitivity = \frac{TP}{(TP+FN)}$$

Back at 1994, Fitzgerald and Lees (1994) already discussed that overall accuracy could be misleading in the assessment of classification, and they recommended cohen's Kappa as a better indicator, which is considered as a more robust represent for interrater reliability. It is given as:

$$\hat{K} = \frac{p_o - p_e}{1-p_e}$$

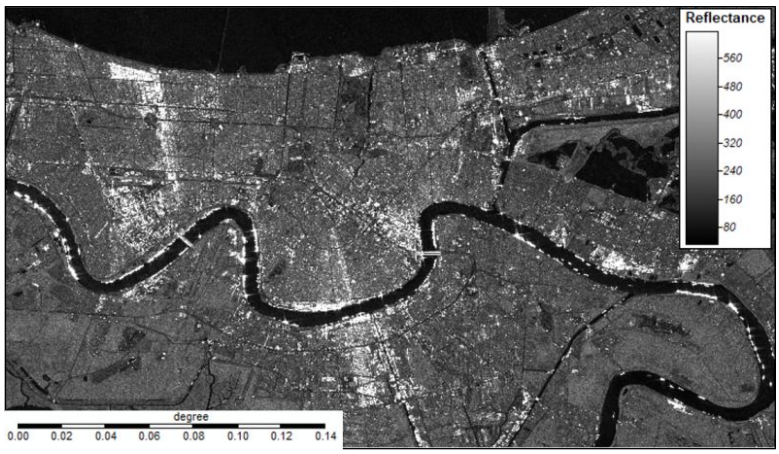

(a) Raw image from Sentinel-1 mission taken at 31st, Dec., 2018, New Orleans

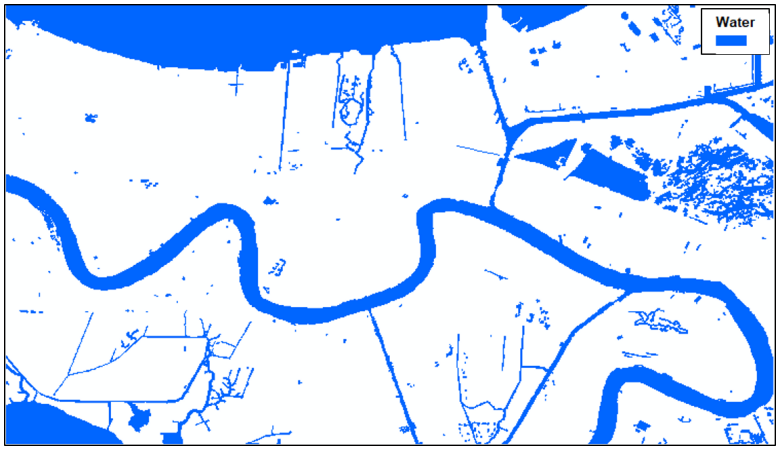

(b) Permanent water area in New Orleans

Figure 4.3: Image and permanent water area for supervised classification algorithm selection

where:

$\hat{K}$: Cohen's kappa coefficient;

p_o: relative observed agreement among raters, which is the summing of diagonal elements of the confusion matrix;

p_e: the probability of random agreement, which is given by:

$$p_e = \frac{1}{N^2} \sum_i N_i . N_{.i}$$

where N is the number of observations and $N_i . / N_{.i}$ are the number of times rater i predicted.

Accuracy, precision and cohen's kappa are not only used to choose a better classifier in this section, it is also applied to evaluate flood forecast model.

Performance of two classifier Figure 4.4 and 4.5 present detection results of two algorithms and their comparison with validation map. Classifications were performed based on the same segmentation result with the same training dataset to control variable. In figure 4.4b and 4.5b colours represent different categories in the confusion matrix. White and blue correspond to TN and TP categories separately where the algorithm classified objects correctly, while the red and green are areas that are in FP and FN categories respectively. Therefore green and red areas indicate the error. As it could be seen, both red and green areas of figure 4.4b are much smaller than those of figure 4.5b. This is examined by summing each category's total area and taking a percentage over the whole area, which is summarised in table 4.2 and 4.3. Scores of the two algorithms are also calculated and presented in table4.4.

It is presented in table 4.4 clearly that the maximum likelihood classification outruns the minimum distance classification in all scores, which indicates an overall better performance, so the maximum likelihood classification is chosen to perform flood detection.

In conclusion, each image that recorded a flood will first be segmented into polygons by seed region growing method. Next polygons are classified by using the maximum likelihood algorithm by which some objects are labelled as water. An Area classified as water subtracting permanent water area gives flood extent of that event. By this procedure each image results in flood map and all these maps are the primary input to the flood forecast model.

(a) Detection result

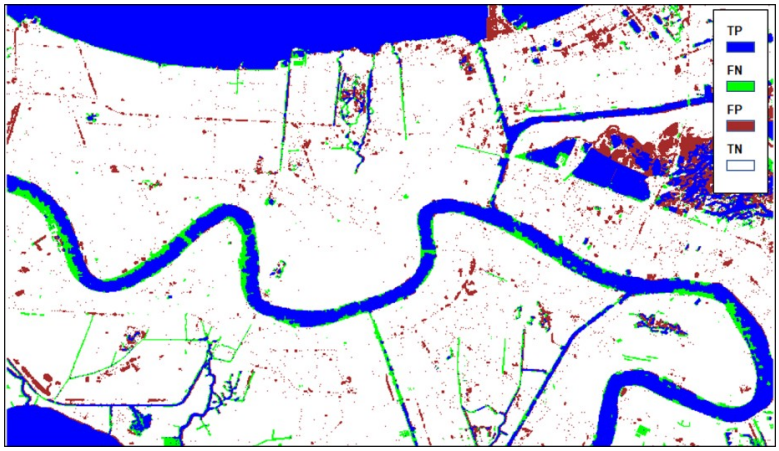

(b) Validation result

Figure 4.4: Detection result by maximum likelihood algorithms

Table 4.2: Confusion matrix of detection result by maximum likelihood algorithm

		Prediction		
		Water	Dry	Sum
Validation map	Water	14.67%	3.20%	17.87%
	Dry	3.56%	78.57%	82.13%
	Sum	18.23%	81.77%	100.00%

Table 4.3: Confusion matrix of detection result by minimum distance algorithm

		Prediction		
		Water	Dry	Sum
Validation map	Water	15.06%	2.80%	17.87%
	Dry	6.25%	75.87%	82.13%
	Sum	21.32%	78.68%	100.00%

Table 4.4: Scores of two algorithms

Scour	**Maximum Likelihood**	**Minimum Distance**
Accuracy	0.932	0.909
Precision	0.805	0.706
κ	0.772	0.713

4.2. Probabilistic forecasting model

The probabilistic forecasting model is trained with input variables whose processing methods are discussed in section 5 and 3.3. This variable includes flood detection result, precipitation, elevation, sea level, drainage capacity and distance to the permanent water area. This model employs two members of Generalized Linear Model(GLM) for predicting probability of flooding. Models' structures and principles of GLM are the focuses of this section.

(a) Detection result

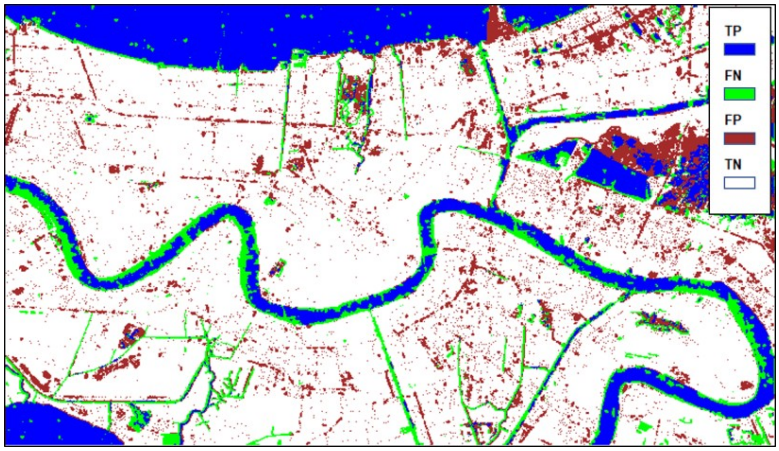

(b) Validation result

Figure 4.5: Detection result by minimum distance algorithms

4.2.1. Model structure

Two different model structures are considered. Both are based on the same grid system which is used in interpolating explanatory variable like precipitation. In the grid system each cell includes data for constructing the model and receiving the forecast result.

4.2.2. Model structure-1

The first flood forecasting model is an ensemble of many unit models. Each cell contains data that is used to train a probabilistic model. In other words, every cell is a independent forecast unit in charge of predicting its own chance of being flooded, and the whole model is an assemblage of these forecast units. The structure of the ensemble model is shown in figure 4.6.

As shown in figure 4.6, the model is constituted of millions of forecast units each of which is trained by its past events' data, and these data include every event's precipitation amount, flood detection result and sea level. In this model structure elevation, distance to the permanent water area and drainage capacity are not considered as model input since for one single cell these variables remain unchanged for all flooding events. Using these input data, each cell trains a forecast model with a set of coefficients, and every cell's probability of being flooded is predicted using its set of coefficients.

4.2.3. Model structure-2

The second model uses the same dataset and is based on the same grid system as the first one. The difference lies in how training data is grouped and utilised. In the first model, each cell is a forecast unit where a independent probabilistic model is trained. For this independent model, each flood event is a data point and the total number of data point is the number of flood events. While the second model includes all cells from several flood events together as one input dataset to train one probabilistic model. Every cell at every flood event is a data point which makes the total number of data points equal to the number of flood events multiplying the number of cells in the grid system. Figure 4.7 presents how one set of training data is grouped.

Each data point contains information of detection from a remote sensing image, precipitation amount, elevation, distance to the permanent water area and drainage capacity all of which are used as model input. Comparing to first

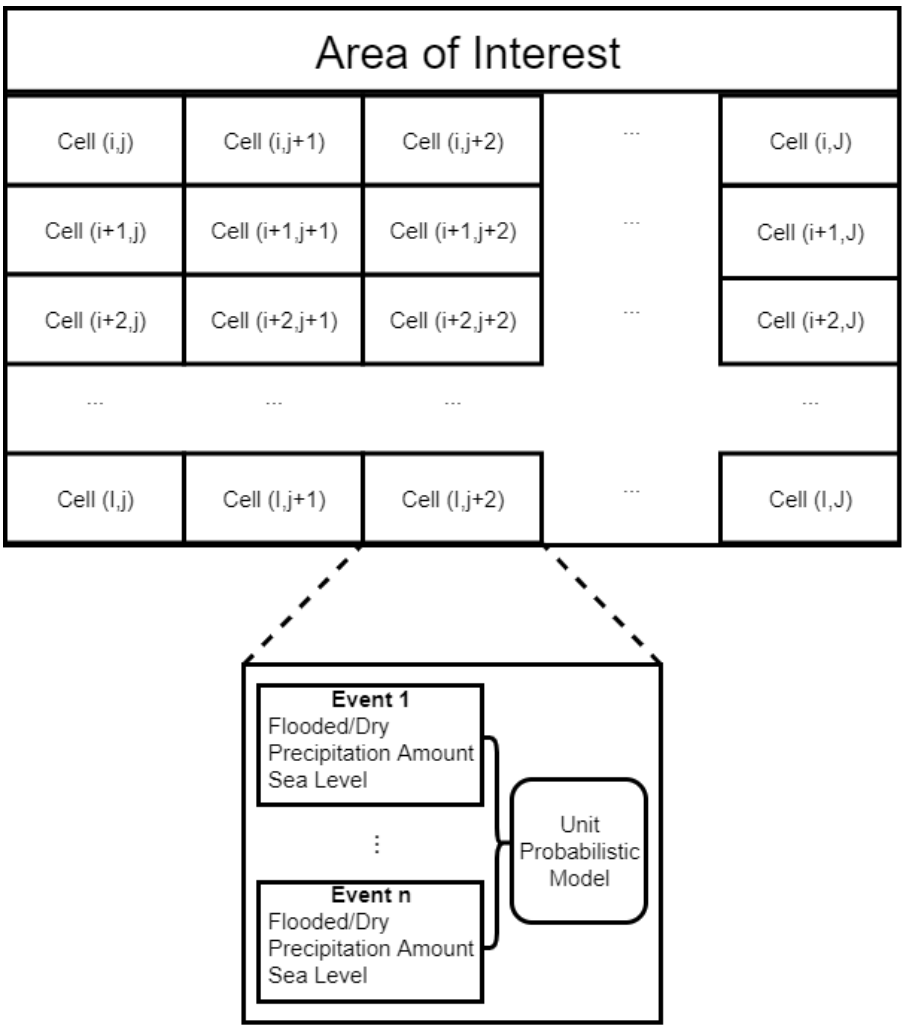

Figure 4.6: First model structure

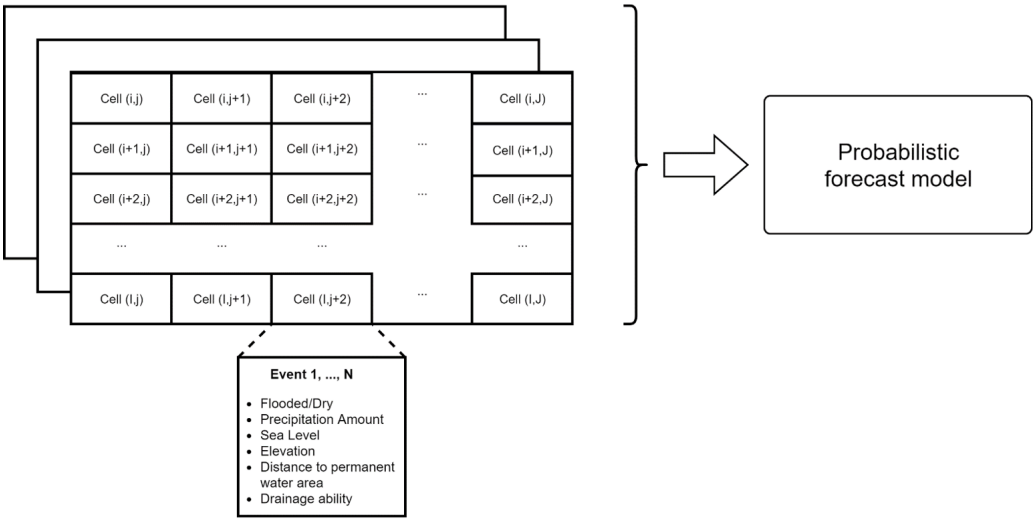

Figure 4.7: Second model structure

structure, the second structure train the probabilistic model based on a much larger data set. With the model structure set and constructed, a probabilistic model is required as the forecasting method.

4.2.4. Generalized linear model

Algorithms employed in this study for predicting the probability of flooding are logistic regression and probit regression, both of which are used in model structure 1 and model structure 2. These two regressions belong to the Generalized Linear Model(GLM) family.

Generalized linear model, which should not be confused with General Linear Model, is a generalization of ordinary linear regression. The response in linear regression is continuous and the result is unbounded. Therefore it is wrong to use an ordinary linear regression for prediction where generalized linear model comes in useful. The ordinary linear regression assumes the response follows the normal distribution with mean and variance μ and σ^2: $Y \mid X \sim N(\mu, \sigma^2)$, while the generalized linear model allows that $Y \mid X$ belongs to an exponential family of probability distributions. For example, in this study, the respond variable flood/dry is a binary variable which follows Bernoulli distribution.

There are three components in GLM(Nelder and Wedderburn, 1972). The first one is a random component which specifies that $Y \mid X$ belongs to the exponential family of a probability distribution. The second one is linear predictor: $\eta = \beta^T \mathbf{X}$. The last one is a link function g which links the random component and the linear predictor in the way of $E(Y \mid X) = \mu = g^(-1)(\mu)$.

The expression of the exponential family of probability distribution is:

$$f(Y;\theta,\phi) = exp(\frac{Y\theta - b(\theta)}{a(\phi)} + c(Y,\phi))$$

Where a, b, c are known functions and θ and ϕ are parameters. This probability distribution could be normal distribution, exponential distribution and Bernoulli distribution etc. Take μ as the mean of the distribution, in other words, $\mu = E(Y \mid X) = Pr(Y = 1)$. With link function we have $\eta = g(\mu)$. Link functions make corresponding regression suitable for specific situation. Members of the GLM family include ordinary linear regression, logistic regression, probit regression and poison regression etc. Because in this study the response variable is binary, logistic and probit regression are used due to the reason that both of them are designed for the prediction of binary variables.

Logistic regression

The link function of logistic linear regression is expressed as:

$$\mu = Pr(Y = 1 \mid X) = g^{-1}(\eta) = \frac{1}{1+exp^{-\eta}} = \frac{1}{1+exp(-\beta^T \mathbf{X})}$$

Where $Pr(Y = 1)$ is the probability of Y equalling a case which in this study is 'flood'. The link function could also be written as:

$$\eta = g(\mu) = log(\frac{\mu}{1-\mu})$$

It shows that the link function is symmetrical in the sense that $g(\mu) = -g(1-\mu)$.

Define $odds = exp(-\beta^T \mathbf{X})$. By rewriting the link function to only have $odds$ term on the left hand side we get:

$$odds = exp(\beta_0 + \sum \beta_i X_i) = \frac{p(Y=1)}{1-p(Y=1)} = \frac{p(Y=1)}{p(Y=0)}$$

Therefore we can compute the result when we increase one unit of predictor variable X_i:

$$\frac{odds(X_i+1)}{odds(X_i)} = \frac{exp(\beta_0+\beta_1 X_1+...+\beta_i(X_i+1)+...+\beta_N X_N)}{exp(\beta_0+\sum \beta_i X_i)} = exp(\beta_i)$$

Here $exp(\beta_i)$ explains the change of $Pr(Y = 1)$ when X_i increase by one unit.

Probit regression

The probit regression is similar to logistic regression in response variable being binary, but the link function in probit regression is:

$$\mu = Pr(Y = 1 \mid X) = g^{-1}(\eta) = \Phi(\beta^T \mathbf{X})$$

Where Φ is the cumulative distribution function of standard normal distribution, which defines the probability $Pr(Y = 1) \in [0,1]$.

Due to the symmetry of normal distribution, link function of probit regression is symmetrical too.

4.2.5. Synthetic Minority Over-sampling Technique

Synthetic Minority Over-sampling Technique(SMOTE) method is applied to model structure 2. In flood detection result the area of flood is only of about 10% overall, therefore the proportions of two classes(flooded and dry) are not balanced, which could lower the accuracy of the forecast model. SMOTE is used to increase the number of flooded data points, which oversamples minority class by synthesising data points before performing classification on imbalanced data (Chawla et al., 2002).

SMOTE creates new data in the feature space. Assuming the aim is to oversample class A at a $N \times 100\%$ of its original size ,where N is an integral number, the first step of SMOTE is finding k nearest neighbours for one point

P_A from class A within that class. New data points are created by using point P_A and its nearest neighbours $P_{1...N}$. Take the difference of explanatory variables between point P_A and one of its nearest neighbours P_i, and multiple the difference with a random number between 0 and 1. The new data point's explanatory variables are equal to adding multiplication result from former step to explanatory variables of point P_A. One new data point is generated in one nearest neighbour direction. This process is iterated N times for each data point in the class A.

In this study, data point in the flooded class is oversampled by SMOTE at a 500% level and oversampled data set is used for training. Models trained by oversampled dataset and original dataset will be compared to analyse the oversampling method's effect.

4.2.6. Evaluation of model's performance

After building a mature forecast model which is capable of generating a map of flooding probability with certain inputs, models' results are subjected to evaluation. In this study two validation methods are used: cross validation and flood record.

Cross-validation is only applied to model structure 2. Several images were grouped as one training dataset to train a probabilistic model, and this model is validated by the rest images. This validation process is repeated by selecting different sets of images each time for training. In the end, every image is used as training data and validation data. The final model is by taking the mean of previous models.

The trained model structure 1 and 2 are validated with real flood records. Scores used as metrics are the same as evaluation of flood detection result, which are precision, accuracy and cohen's kappa. These scores have already been discussed previously. A new tool is introduced from evaluating flood forecast model: Receiver operating characteristic(ROC) curve.

Receiver operating characteristic(ROC) curve

In this study ROC is employed for choosing a threshold of probability. Logistic regression or probit regression informs people about the probability of response equalling one, which is a value between zero to one. Therefore a threshold is required, when one prediction's probability is above the threshold we take it as being predicted flooded and vice versa. ROC curve is a graphic method for choosing a cutpoint by plotting true positive rate (TPR) against the false positive rate (FPR) 4.8a. True positive rate is sensitivity 4.1, while false positive rate equals to $1 - specificity$:

$$FPR = 1 - specificity = 1 - \frac{TN}{TN+FP}$$

Figure 4.8a shows an example of ROC curve from made-up data.

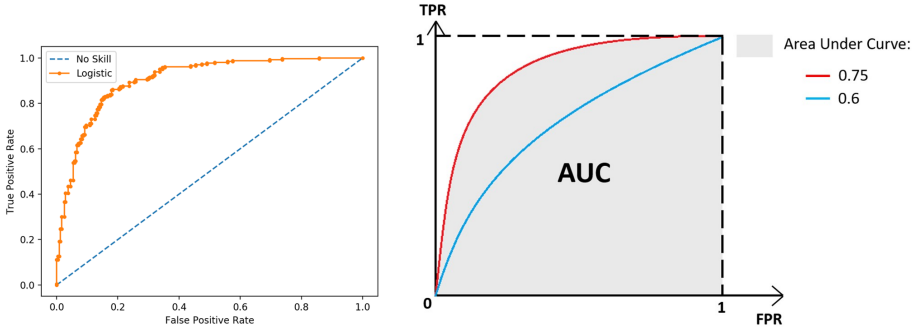

(a) Example of ROC curve

(b) Example of AUC

The ROC curve shows the trade-off between TPR and FPR. The result of the ideal model falls on the upper-left point (0,1). It suggests that it scores full point in true positive rate and zero in false positive rate. A random model falls on the diagonal line. Basing on ROC curve, some other index such as Youden Index and Distance to Corner are used for deciding a cutpoint of probability. Distance to Corner method uses the point on the curve which is closest to the point(0,1) as cutoff value. Area Under Curve(AUC) of ROC curve is another measurement which is the total area under the ROC curve. A closer AUC value to 1 suggests a better accuracy. The model is not useful when AUC equals 0.5. An illustration of AUC is presented in figure 4.8b. Shadow area is the AUC. The area under the red curve equals 0.75 which indicates that its performance is better than the blue curve whose AUC is 0.6.

5

Flood detection of remote sensing images

The first step of constructing the model is detecting flood extent from remote sensing images, and the result is given in this chapter in details. Information on flood events and remote sensing images is presented, and these images are processed in the manners described in section . Both raw images and flood detection result are shown.

5.1. Study flood events

5.1.1. New Orleans

By searching in NOAA's storm event database and the News, since the year 2000 forty-two pluvial flooding events happened in New Orleans, but it is unrealistic to have every flood event recorded by a satellite image. Considering the flood defence system undergone major modification after hurricane Katrina, the study period is taken as from 2006 until now. After looking in several satellites mission, thirteen images that were taken within 36 hours after the flooding were found, which recorded eleven flooding events because two events are recorded by two images. ALL images are accessed by European Space Agency(ESA)(Agency, a). They are listed in table 5.1. However, among these thirteen images only seven images cover the whole study area. These thirteen images constitute the New Orleans' flood events' database.

Table 5.1: Date of study flood events and images at New Orleans

Date of flooding event			**Date of image being taken**					
Year	**Month**	**Date**	**Satellite**	**Year**	**Month**	**Day**	**Hour**	**Minute**
2008	9	1	**TerraSAR-X**	2008	9	2	11	58
2008	9	1	**Radarsat2**	2008	9	2	11	58
2010	5	16	**Cosmo-SkyMed**	2010	5	16	23	51
2011	9	3	**Cosmo-SkyMed**	2011	9	4	11	52
2011	9	3	**TerraSAR-X**	2012	4	3	11	50
2012	4	4	**Cosmo-SkyMed**	2012	4	3	11	50
2012	8	29	**TerraSAR-X**	2012	8	29	12	8
2016	4	1	**Radarsat2**	2016	4	1	23	57
2016	8	15	**TerraSAR-X**	2016	8	15	11	59
2017	8	5	**Radarsat2**	2017	8	6	11	55
2018	8	22	**Cosmo-SkyMed**	2018	8	22	11	41
2019	4	4	**Sentinel1**	2019	4	6	0	2
2019	7	10	**Sentinel1**	2019	7	11	0	2

5.1.2. Miami

The type of study flooding event at Miami is coastal flooding resulting from the 'King tide', which is an extremely high tide. It has been rising people's attention in Florida state because in recent years every autumn it leads to several floods at seaside cities. By Florida state's definition, king tide refers to high tides introduced by moon and sun aligning, when the combined gravitational force exerted by moon and sun are at the largest(Román-Rivera and Ellis, 2018). At Miami, the king tide happens around September - November, and each time it lasts from three days to a week. Researchers noticed that sea level rising makes sea level at high tide higher(Wdowinski et al., 2016), which causes the number of times of coastal flooding surged in recent years. My research agrees with this phenomenon. In NOAA's

storm event database there was no record of coastal flooding at Miami before the year 2012, but the frequency of coastal flooding at Miami increases in the following years. The dates of these records are used to find images from different satellites that recorded high tides. Six images were found and they are listed in table 5.2.

Table 5.2: Date of study flood events and images at Miami

Date of flooding event				**Date of image being taken**					
Year	**Month**	**Date**	**Sea Level(m)**	**Satellite**	**Year**	**Month**	**Day**	**Hour**	**Minute**
2016	10	15	1.03	**Sentinel-1**	2016	10	15	23	27
2016	11	14	0.796	**Sentinel-1**	2016	11	14	23	27
2017	10	4	1.114	**Sentinel-1**	2017	10	4	23	27
2017	10	4	1.0585	**Cosmo-SkyMed**	2017	10	4	11	3
2019	9	26	1.066	**Cosmo-SkyMed**	2019	9	26	23	12
2019	11	22	1.043	**Cosmo-SkyMed**	2019	11	22	11	4

5.2. Flood detection result and analysis

Images summed in table5.1 and 5.2 are presented in this section. Segmentation and supervised classification were performed on them to detected inundation area. The image is first filtered with a Gaussian filter to remove speckles. Then images were segmented by seed region growing into polygons, which are labelled to classes by maximum likelihood classifier. Areas classified as 'water' subtract permanent water area gives the inundation area. Raw images and detected flood extent are compared and shown.

5.2.1. New Orleans

Flood detection results of New Orleans are shown in figure 5.1. In this set of figures, (a) shows the raw image and (b) the flood detection result. Some of these images only cover part of the study area, and the rest area is filled with permanent water area from OpenStreetMap.

5.2.2. Miami

Flood detection results of Miami are presented in figure 5.2. In this set of figures, (a) shows the raw image product, (b) the flood detection result, and these images are given in the order of table 5.2

5.3. Validation

Flood detection results are validated by some known flooded locations. None of these flooding events are severe enough so that its flood map is produced, and no aerial image is available for these events. Therefore it is not possible to validate the flood detection result over the whole study area. However, all of them were recorded in NOAA's storm event database or reported in the news, by which some flooded locations are known. Therefore flood detection result is validated by these locations.

Full records and sources of these flooding events are presented in Appendix A. For New Orleans area there are 27 locations that are known as flooded in reports or the news. Checking these locations with flood detection result there are 19 locations being detected as flooded from images, which gives an accuracy at 70.4%. Flood detection results are inspected in order to find out the reasons of low accuracy.

5.4. Analysis and summary

Generally for flood detection following methods taken by this study, the sources of error could be from the quality of the images and processing methods, which include: image taken at high incident angle(angle between sensor's wave direction and surface's normal direction), low image resolution, inaccurate segmentation and classification and et al. Based on the validation result and visual analysis of these images, there are several errors existing in them.

Reviewing all images, they are products taken from different satellites, at different incident angles, polarisation and passes. Even one satellite mission has several modes, each of which is of one specific resolution. The full information of each image could be found in Appendix B. Although it is preferred to use image from one sensor exclusively with similar parameters, the low chances of having a satellite flying over study area during flooding period require utilising images from different sources in order to make sure data number being large enough. Inevitably, the quality of flood detection result is jagged. The highest resolution among these thirteen images is 1m while the lowest resolution is 50m. A resolution too low could lead to one pixel covering different objects causing a rougher detection result. In the downtown area, backscatter of the building tends to cover roads in images of low resolution. One small area of New Orleans is taken to illustrate how resolution affects on detection result. Figures 5.2 are remote sensing images of that area in three different resolutions. it could be seen that in the upper image, which is of a resolution at 3m, the road and the building are discernible. Other two images are of lower resolutions, but still the image in the middle is

of a resolution at 30m, which shows much more details than the image at the bottom with a resolution at 50m. In the report of flood event at 1st,April,2016, the downtown area of New Orleans is reported as seriously flooded, but in image 5.1n, no flooding is detected in that area with high reflectance of building blocking streets.

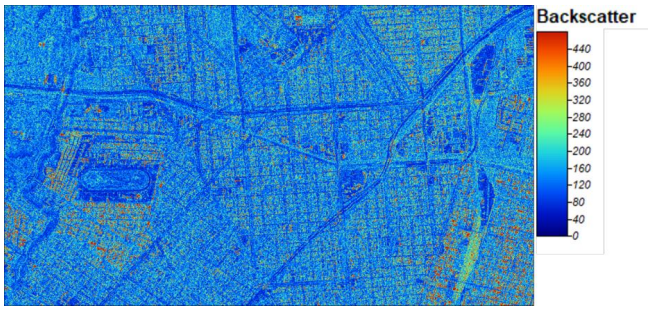

(m) Resolution at 3m

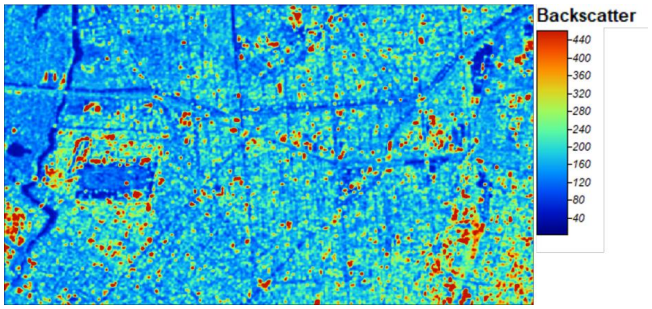

(n) Resolution at 30m

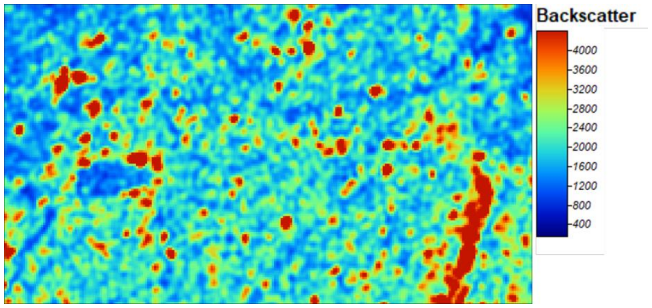

(o) Resolution at 50m

Figure 5.2: Same location in images with varies resolutions

Existence of cloud is another possible reason for error. SAR sensor's wave penetrates cloud, but cloud and precipitation are capable of perturbing radar signal(Marzano et al., 2010, Yonezawa and Takeuchi, 2003). For example, two images recorded flood event happening at New Orleans 2nd, Sep., 2008, one of which was taken by satellite mission TerraSAR-X and one by Radarsat-2 at a lower resolution and 20 minutes earlier. In the image taken by TerraSAR-X at the east-southern area there is a spindle shape area with low backscatter value, which usually indicates water. And that area is identified as flooded. But in the image taken by Radarsat-2 at that location no dark area is observed. It could not be ruled out that the area was flooded during those 20 minutes, however, it also could be a shadow causing by cloud. It is difficult to identify the cause unless other records existing.

Other problems originated from images like shadows of high objects demand analysing each image separately, which require to use more complicated algorithms. These will increase this project's workload to a higher magnitude, therefore they are not performed here.

Another problem among New Orleans' detection result exists along the edge of water bodies, where edge of seaside are detected as water but not marked as water in reference map. Because the river levee and sea levee did not fail, it is likely to be classification error. In examination of the classification algorithm, figure 4.4, which was taken during a dry period, also exhibits this result, so it should be explained by reasons other than flooding or precipitation. Two reasons could explain that. The first reason is that reference map does not record the water area perfectly. For example, in the east area of New Orleans, there is a swamp where it is often labelled as water in the detection result but not in reference map. Change in swamp's shape and high soil water content due to tides could caused this area being detected as water. Second, object based analysis caused that error. If the difference of reflectance between riverbank and river did not exceed criteria, a pixel of riverbank could be merged with a pixel of the river into one object. Because the supervised classification labels one object by using its mean value, that object is still classified as water which leads to the edge shape detected water area along the water body. In Miami, along the edge of islands, edge-shape detected flood areas

also exit. However, Miami and Miami beach do not have coastal flood defence system like New Orleans, so these areas are exactly flooded area where the algorithm tries to detect.

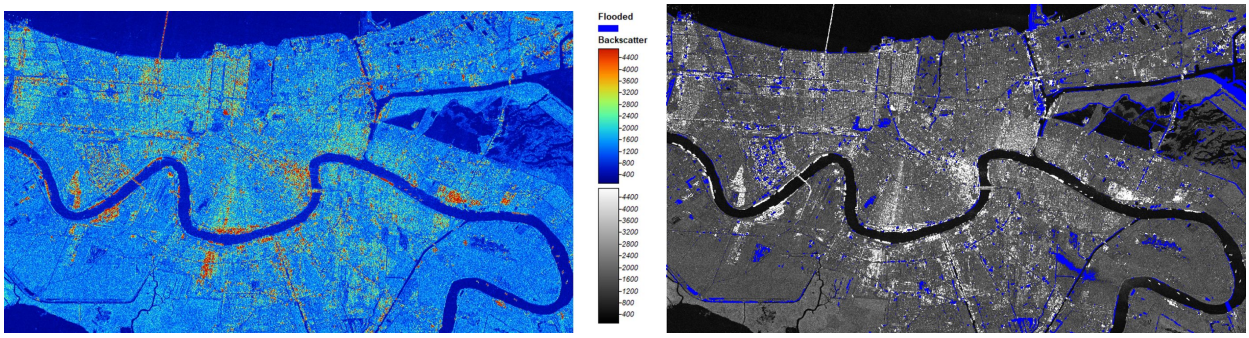

(a) Raw image(02/09/2008) By TerraSAR-X

(b) Flooded area(02/09/2008)

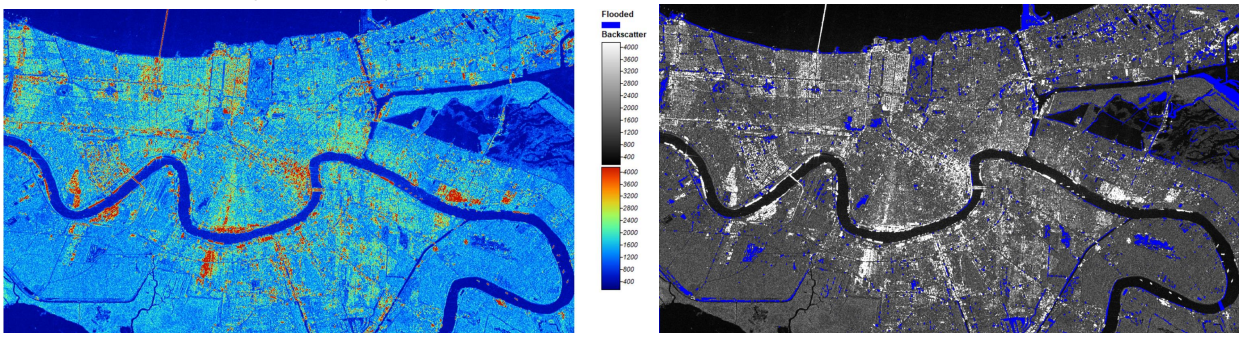

(c) Raw image(02/09/2008) by Radarsat-2

(d) Flooded area(02/09/2008)

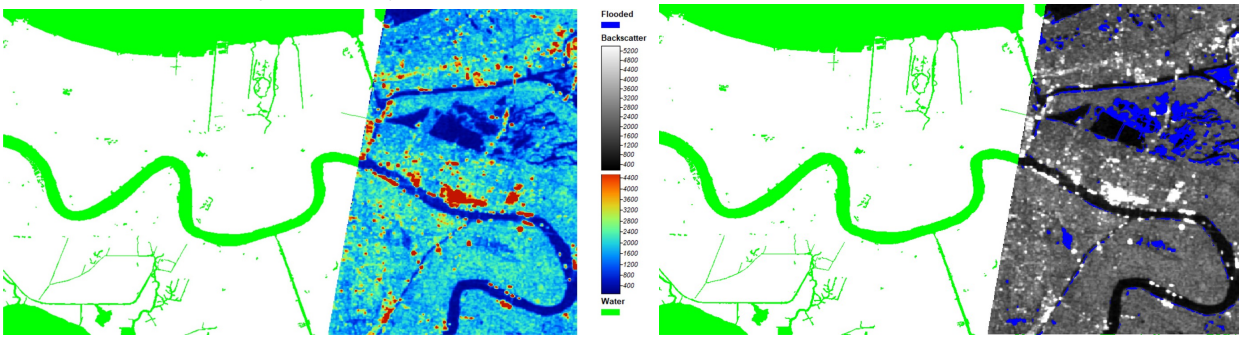

(e) Raw image(16/05/2010)

(f) Flooded area(16/05/2010)

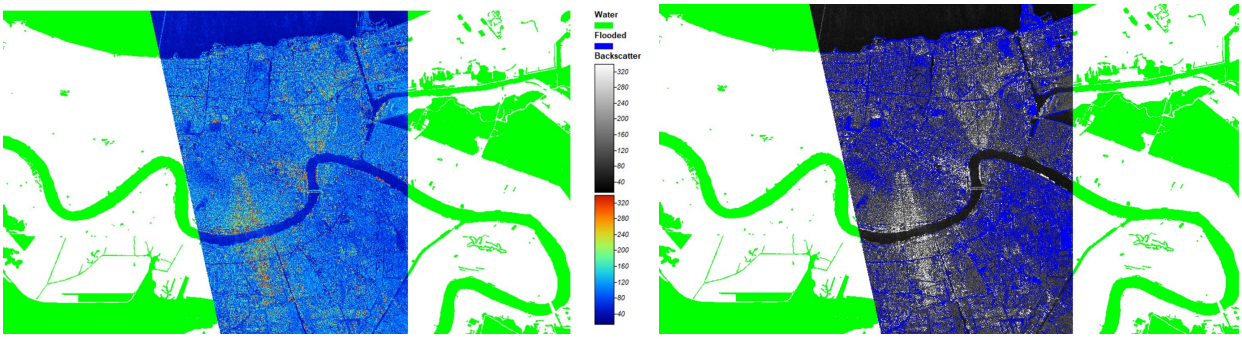

(g) Raw image(04/09/2011)

(h) Flooded area(04/09/2011)

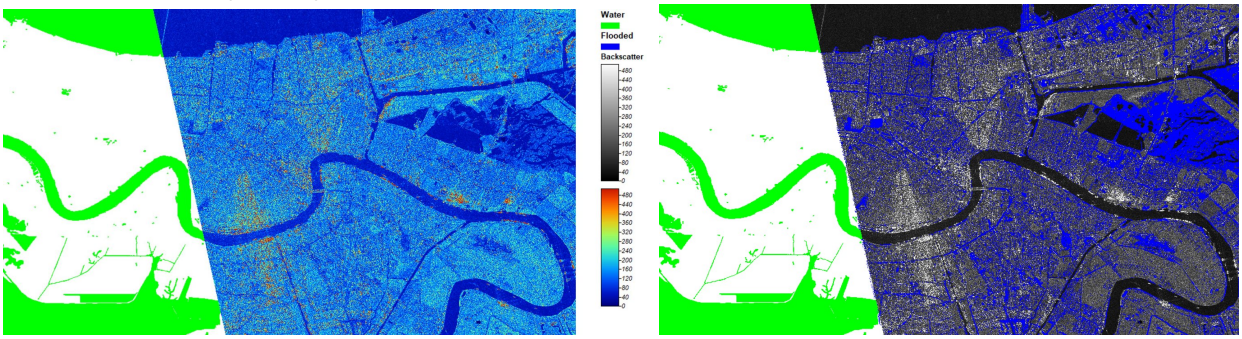

(i) Raw image(03/04/2012) by CosmoSky-Med

(j) Flooded area(03/04/2012)

Figure 5.1: Raw image and flood detection result of New Orleans

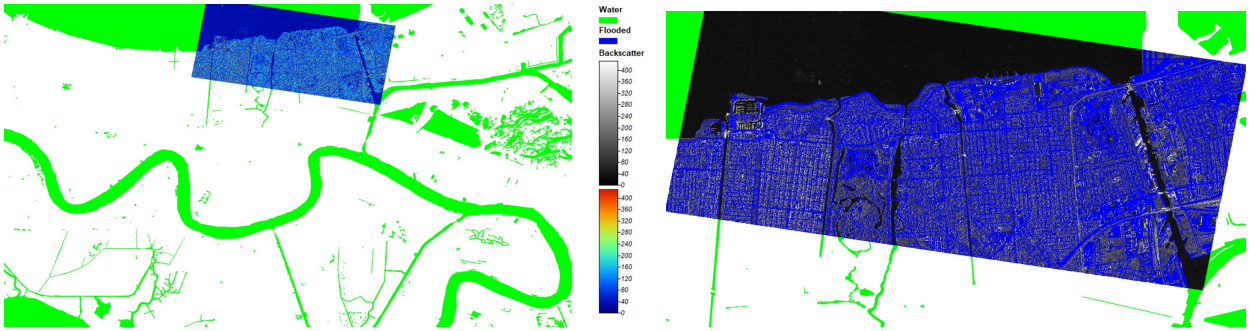

(k) Raw image(03/04/2012)by TerraSAR-X

(l) Flooded area(03/04/2012)

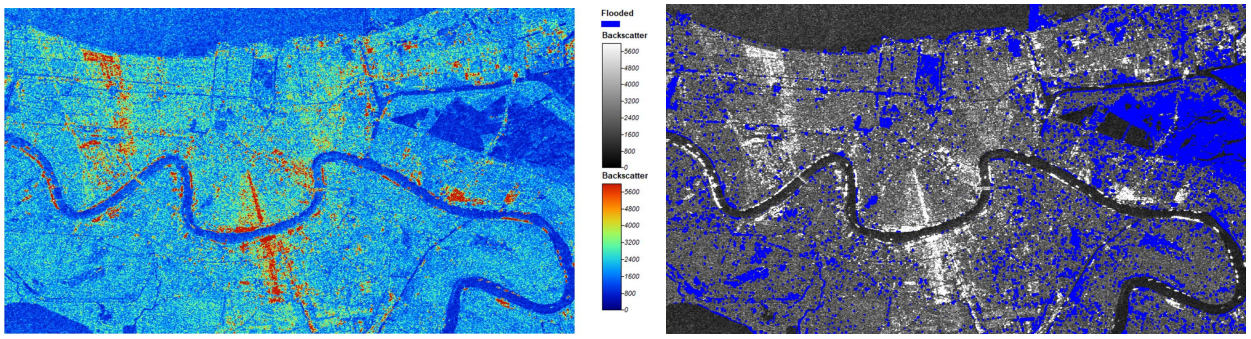

(m) Raw image(01/04/2016)

(n) Flooded area(01/04/2016)

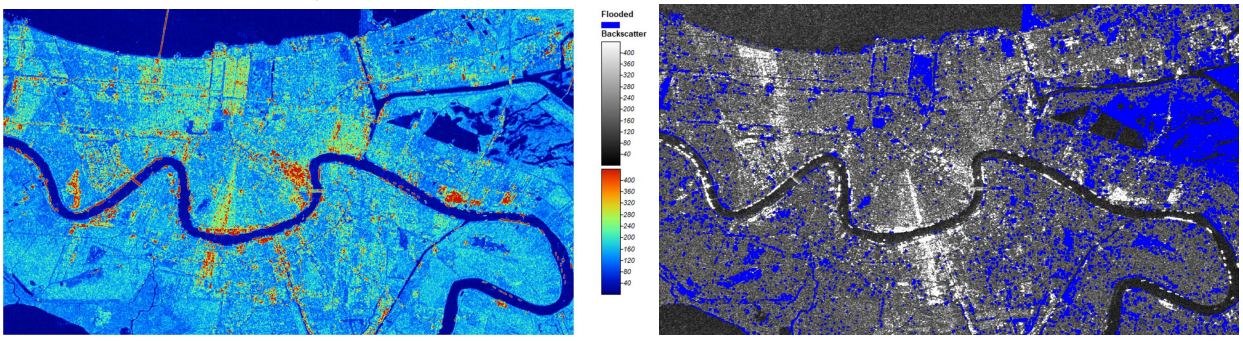

(o) Raw image(15/08/2016)

(p) Flooded area(15/08/2016)]

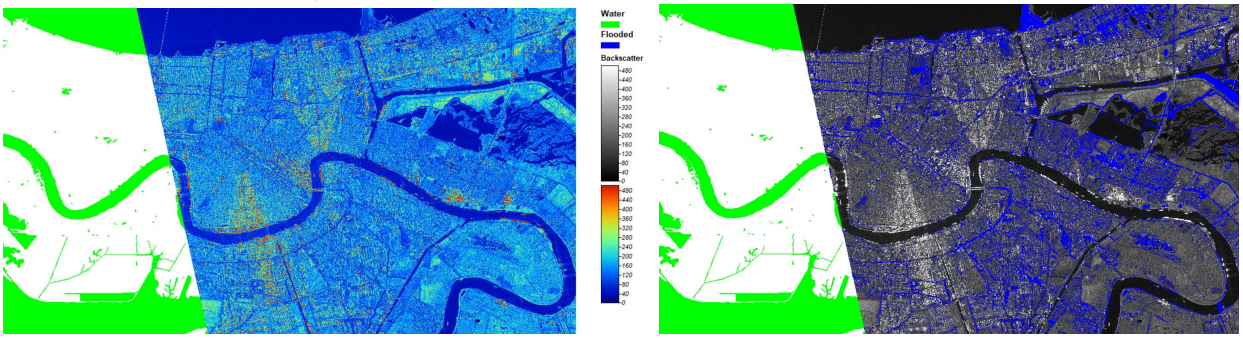

(q) Raw image(05/08/2017)

(r) Flooded area(05/08/2017)

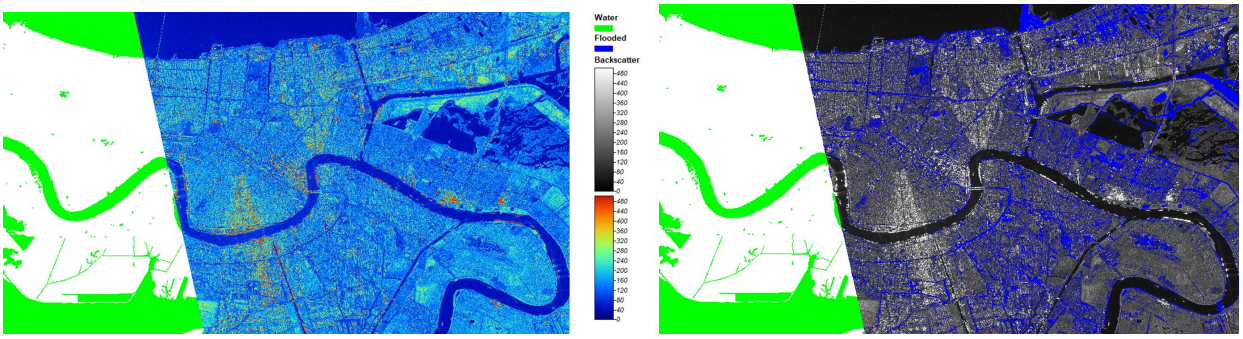

(s) Raw image(22/08/2018)

(t) Flooded area(22/08/2018)

Figure 5.1: Raw image and flood detection result of New Orleans

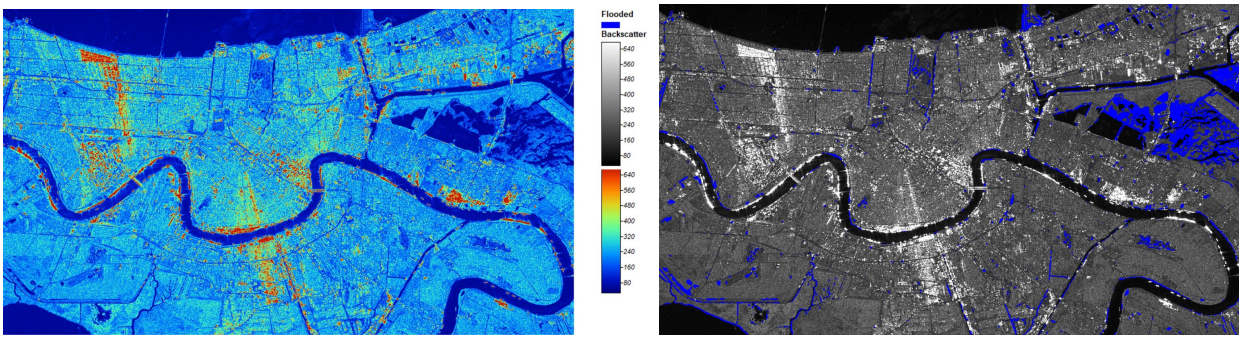

(u) Raw image(06/04/2019)

(v) Flooded area(06/04/2019)

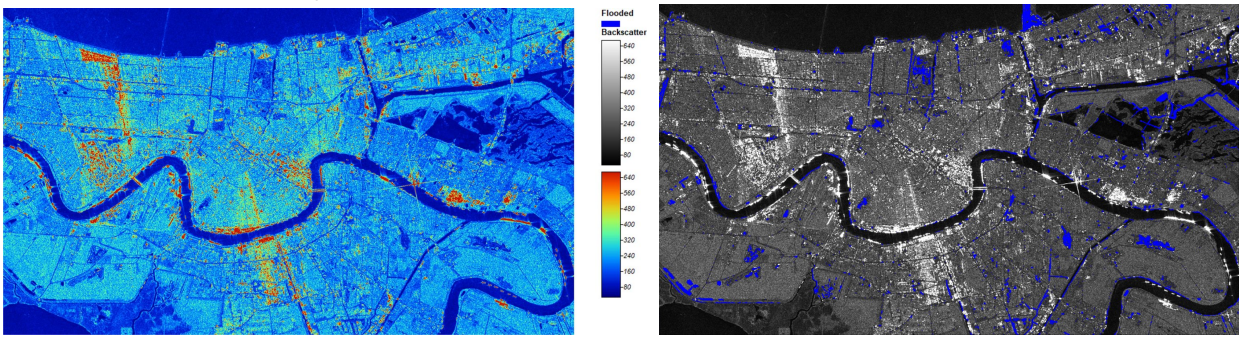

(w) Raw image(11/07/2019)

(x) Flooded area(11/07/2019)

Figure 5.1: Raw image and flood detection result of New Orleans

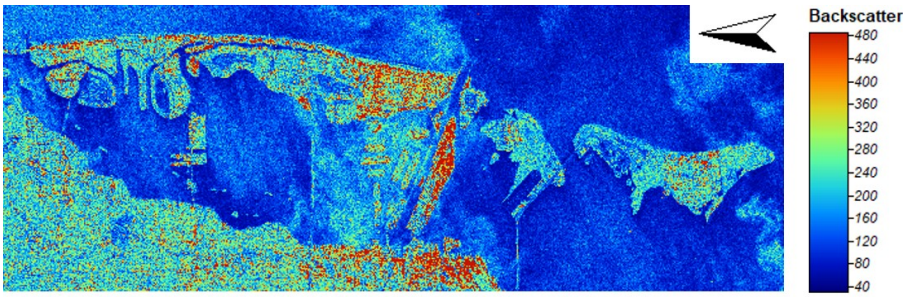

(a) Raw image(15/10/2016)

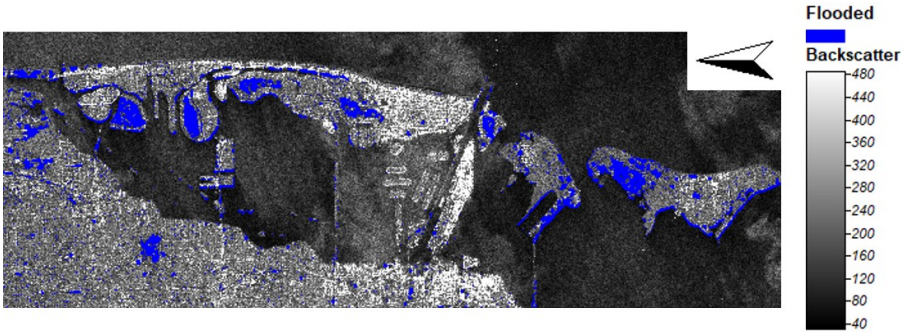

(b) Flooded area(15/10/2016)

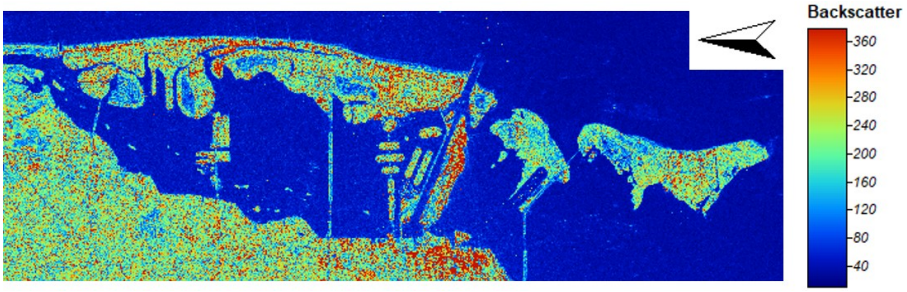

(c) Raw image(14/11/2016)

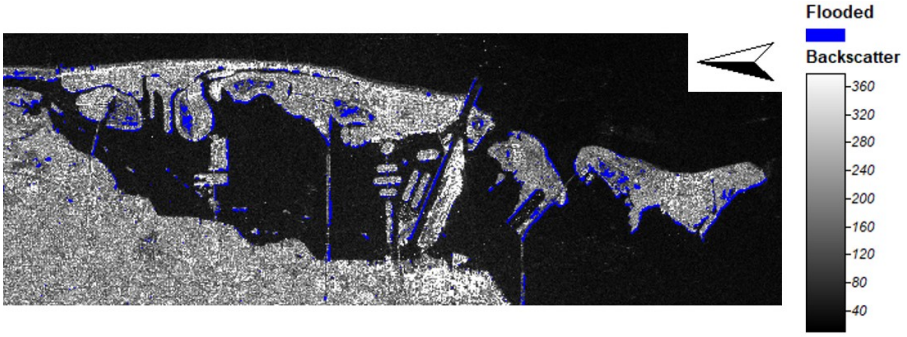

(d) Flooded area(14/11/2016)

Figure 5.2: Raw image and flood detection result of Miami

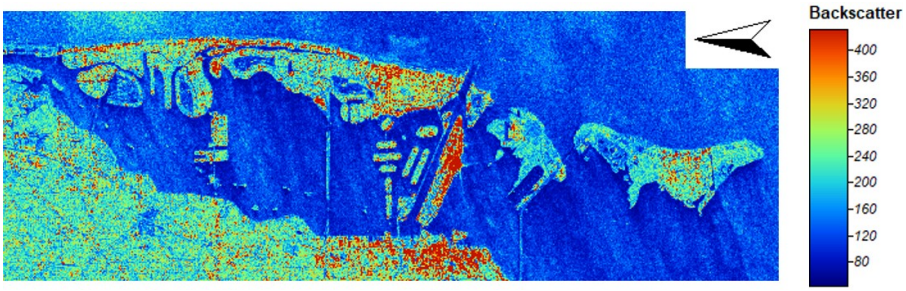

(e) Raw image(04/10/2017) from Sentinel-1

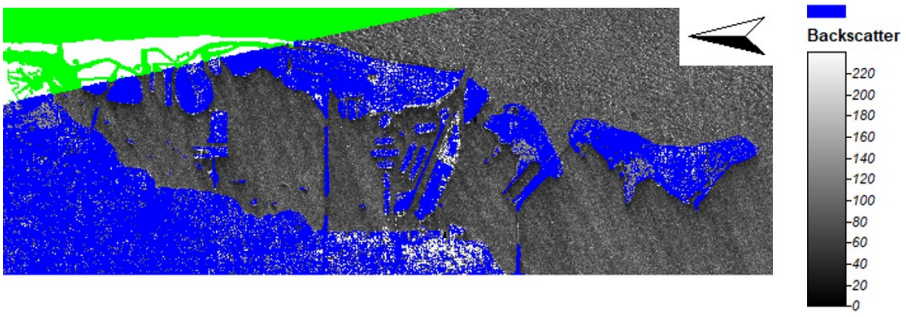

(f) Flooded area(04/10/2017) from Sentinel-1

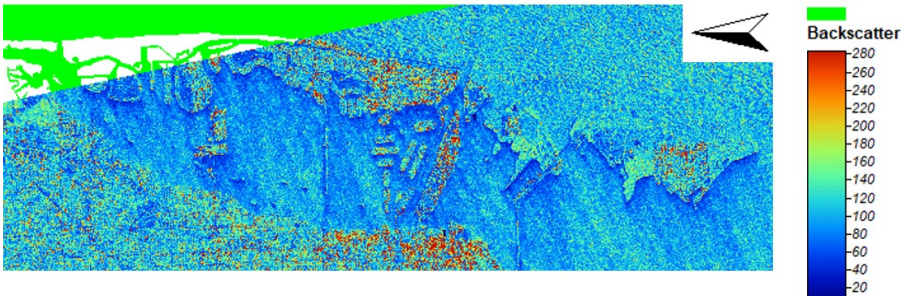

(g) Raw image(04/10/2017) from Cosmo-SkyMed

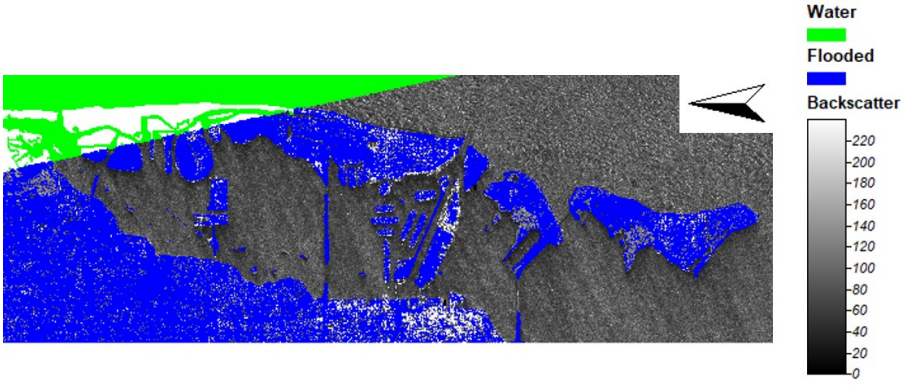

(h) Flooded area(04/10/2017) from Cosmo-SkyMed

Figure 5.2: Raw image and flood detection result of Miami

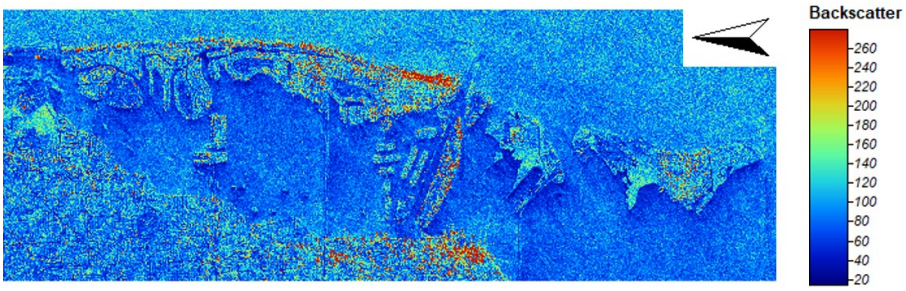

(i) Raw image(26/09/2019)

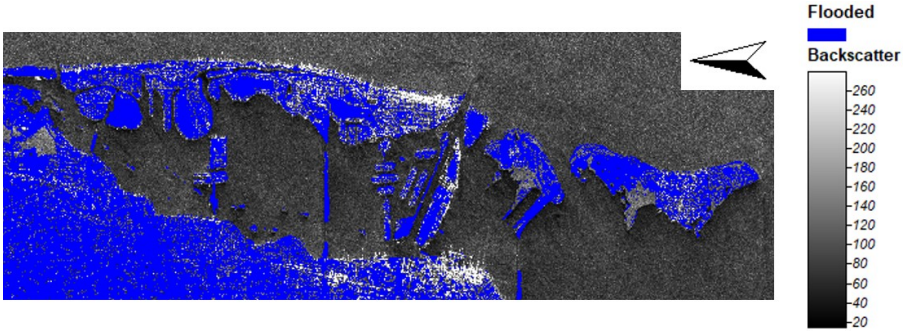

(j) Flooded area(26/09/2019)

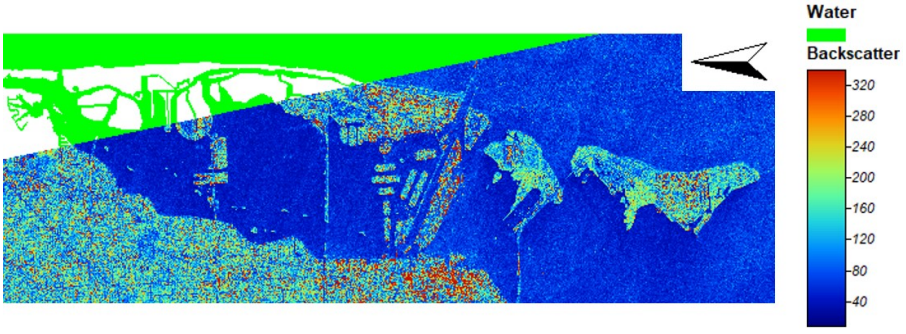

(k) Raw image(22/11/2019)

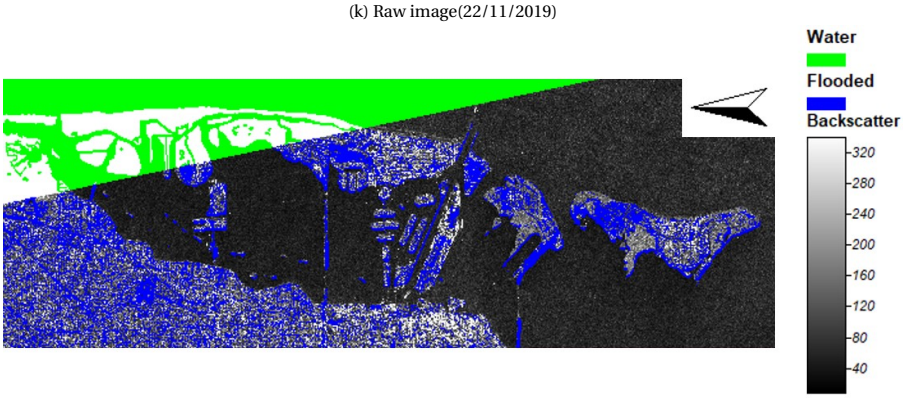

(l) Flooded area(22/11/2019)

Figure 5.2: Raw image and flood detection result of Miami

6

Probabilistic forecasting model

The preparation of the model is finished and the model is ready to be run. In the last chapter the detection result of remote sensing image is discussed, and in previous chapters description of flood conditioning variables and methodologies of the model is given. Hitherto the data of variables are already cleaned and process and the structure of the model is built. This chapter presents and analyses the result of models.

6.1. Result of model structure 1

New Orleans study area data is used to test model structure 1. This model uses one cell's own historical data for training, therefore, due to a limited number of suitable and available remote sensing images, this model is trained with only a few data points. Because for Miami study area only six remote sensing images are acquired, which means a maximum of six data points for each training, the number of data is determined too few to have a robust model. So the first model structure is only examined at the New Orleans study area, which has twelve images. Variables used for predicting New Orleans flooding include precipitation and sea level. Elevation, distance to the water area and drainage capacity remain unchanged over time for one cell so they will not influence models' result even when considered as input.

Although in total there are twelve images, some images do not cover the whole study area, which results in the inconsistent number of being taken by a image across the study area. The times that one cell is included in the image is given in the figure 6.1a. The number of times of being recorded by remote sensing images for one cell is the number of data points for the cell in training. And the ratio of one location being detected as flooded over all the times when it was recorded in a remote sensing image is calculated and presented in figure 6.1b. Locations with high frequency of being flooded is in yellow colour, which are along the seaside, some streets at the downtown, the suburb area at the northwest side and the swamp area at the northeast area.

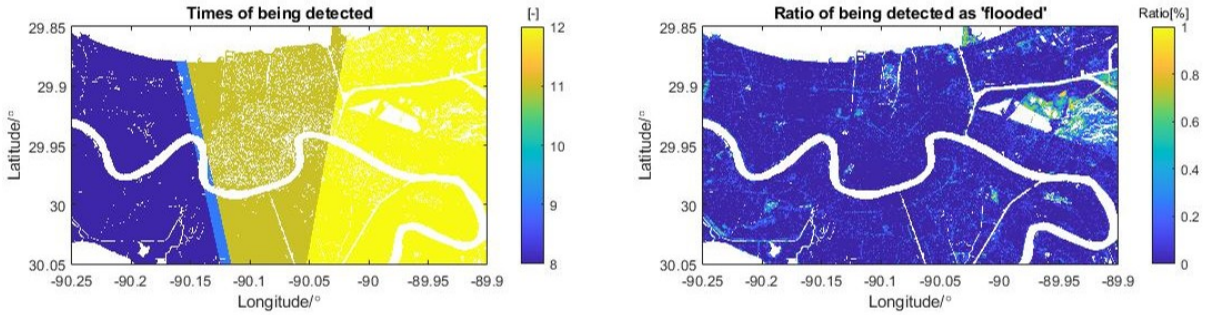

(a) Time of being taken in a remote sensing image

(b) Ratio of being detected as flooded

Figure 6.1: Times of one location being taken in a remote sensing image and ratio of one location be detected as flooded

Training each cell with its own model means each cell is in charge of predicting its own probability of flooding and has its own coefficients. Coefficients of each cell's intercept, precipitation and two sea level stations' record are shown in figure 6.2.

One problem of this model structure is that at many cells too few data points leads to failed training or extremely value of coefficients. In this figures above, the grey area are cells that did not result in a successful model because that area has never been reported as being flooded in study events. As we can see that only a part of the study area built a probabilistic model, however, among these cells, there are many cells with extremely large or small coefficients. Because the absolute value of coefficient of precipitation is much smaller than other coefficients, so colour range of

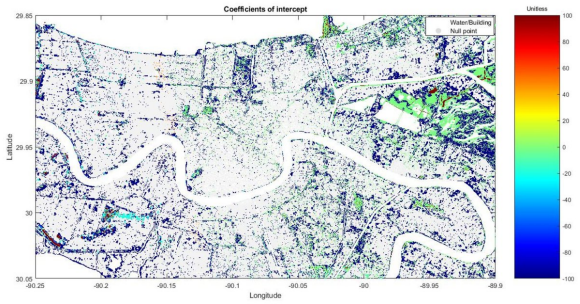

(a) Coefficient of intercept

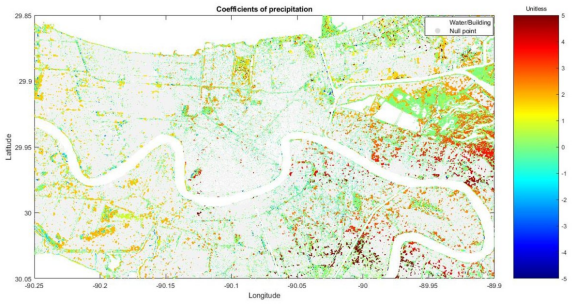

(b) Coefficient of precipitation

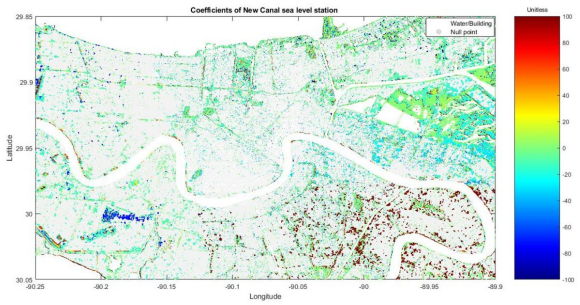

(c) Coefficient of sea level station New Canal

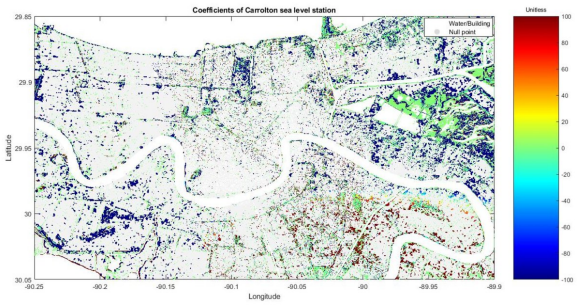

(d) Coefficient of sea level station Carrolton)

Figure 6.2: Coefficients of New Orleans trained by logistic regression

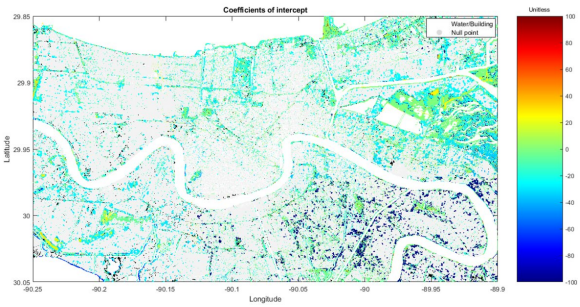

(a) Coefficient of intercept

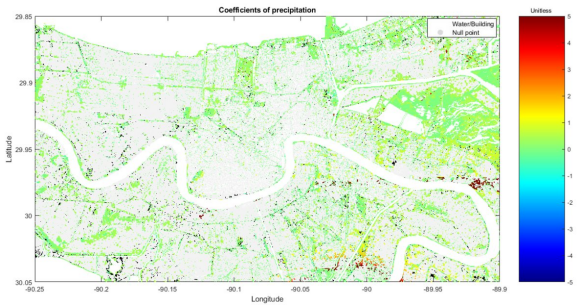

(b) Coefficient of precipitation

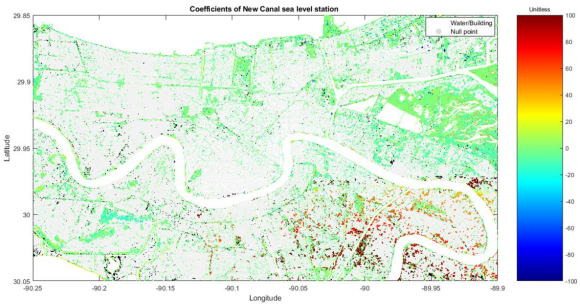

(c) Coefficient of sea level station New Canal

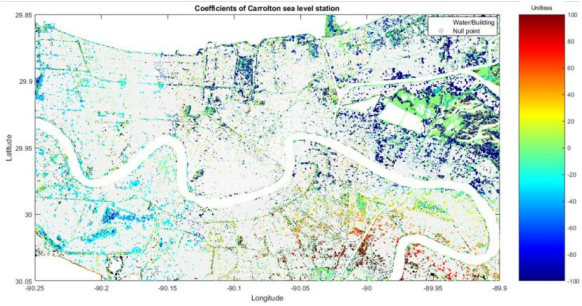

(d) Coefficient of sea level station Carrolton)

Figure 6.3: Coefficients of New Orleans trained by probit regression

coefficient of precipitation is set as $[-5,5]$, while other coefficients' colour range is set as $[-100,100]$. A large portion of locations the coefficients exceed the maximum or minimum limits. In fact, the values of the coefficient of some cells reach a magnitude of e^10, which is not reasonable. This problem could only be solved by obtaining more flood records from remote sensing images.

If focusing on cells that succeeded in training a model, it could be seen that both regressions resulted in positive coefficients of precipitation for most cells, which reflects that the relationship between precipitation and flooding is correctly captured, however, values of the coefficient of sea levels are not uniform. The coefficient of water level at carrollton station fluctuates among different areas. In the southeast area the coefficients are mostly positive related to water level, while in another area the raise in sea level reduces the probability of flooding. The location of carrollton station could be a reason for this. This station is set at the riverside of Mississippi river, therefore the discharge of the river also has an influence on the water level. The coefficient of New Canal sea level station records are more uniform across the whole study area. At most area the coefficients are close to zero. Except in the southeast area,

where coefficients of two sea level stations are predicted to be extremely high.

Constructed model's performance is validated with five events. The Receiver Operating Characteristic curve is generated by using the threshold of probability which is an arithmetic progression from 0 to 1 with 0.025 as a step. The result is presented in figure 4.8a. The model's performances of each event vary hugely. The accuracy of prediction of event happened at 6^{th}, April, 2019 is significantly better than other events'. Two events result in the curves below the diagonal line, which indicates the model's incapability of forecasting flooding correctly. Overall the model could not give a stable accurate forecast of all events. There is no huge difference between result trained by two regressions, both of which gave a similar curve of each flood event.

To choose the threshold of probability, $distancetocorner$ is used. For one cell, if the forecasted probability is higher than the threshold, it is predicted as 'flooded', otherwise 'dry'. The cutoff value is chosen by the point that is closest to the upper-left point(0,1). Once the cutoff of probability is settled, a flood extent map is produced, and scores of validation of the map are calculated, such as accuracy and Cohen's kappa. Scores are summarised in table 6.1.

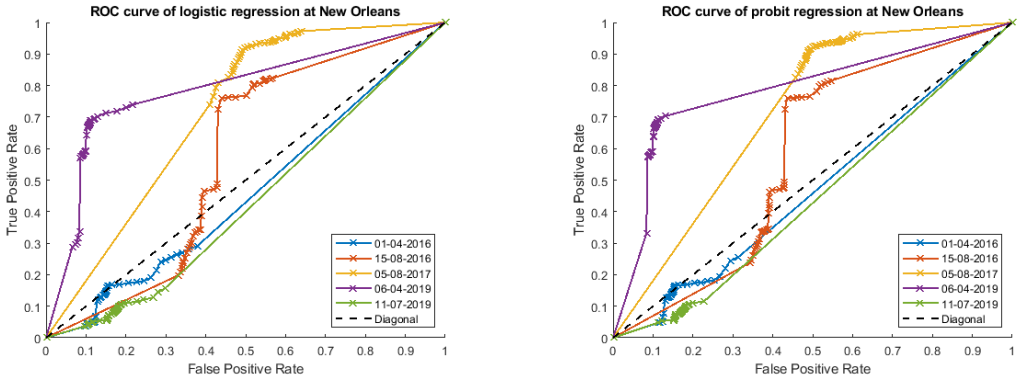

(a) Logistic regression

(b) Probit regression

Figure 6.4: ROC curve of New Orleans model-1

Table 6.1: Scores of model-1 at New Orleans

Regression	Threshold	Scores			
		Precision	Accuracy	F1	Kappa
Logistic	0.270	0.205	0.648	0.258	0.046
Probit	0.290	0.199	0.616	0.254	0.022

6.2. Model structure 2

This model structure takes flood information from several flood events to construct one model which contains millions of training data points. Since some images only cover a part of the study area in New Orleans, they should not be included in the dataset to predict the probability of flooding for the whole area. Therefore these images are excluded. When two images recorded the same flood event, the one of higher resolution is chosen. In total, six images are used for training at New Orleans and six images for Miami. All variables are standardised into $[0,1]$ for comparison of coefficients. Oversampling method SMOTE is applied to each fold in cross-validation separately before training, and differences between model applying over-sampling method SMOTE and without over-sampling are discussed either.

6.2.1. New Orleans' flood forecast

At New Orleans, flood conditioning factors include: precipitation, drainage capacity, elevation, sea level and distance to permanent water. Before training these variables are standardised to $[0,1]$ for the purpose of comparing coefficients. Several sets of models are trained and compared to find the optimal model for New Orleans.

Comparison between using raw precipitation and weighted precipitation

Two ways are used to calculate the precipitation amount in this study. One is simply summing up the precipitation and the other one is weighting the precipitation rate according to time. Precipitations calculated by two methods are used for prediction to examine how they relate to flooding. Both of them are used as one single input variable to train a model separately. Variables are all standardised to $[0,1]$ therefore the value of precipitation does not affect the coefficients' values.

Coefficients of models trained by two kinds of precipitation are shown in table 6.2. Coefficients of time-weighted precipitation are 3.02 and 1.80 for logistic regression and probit regression respectively, both of which are larger than

coefficients of raw precipitation, which means that flooding is more sensitive to precipitation when time effect in considered. This suggests that time element is crucial and it should be considered in the flood forecasting model. Therefore time-weighted precipitation is used in training the model instead of simply summing precipitation.

Table 6.2: Coefficient of precipitations with and without weighting

Regression	Event set	Raw precipitation		Weighted precipitation	
		Intercept	Precipitation	Intercept	Precipitation
Logistic	**Exclude event-1**	-1.94	2.05	-2.45	4.02
	Exclude event-2	-1.57	0.43	-1.45	0.01
	Exclude event-3	-1.51	1.63	-2.01	3.59
	Exclude event-4	-1.64	1.78	-1.78	3.03
	Exclude event-5	-1.89	2.85	-2.14	3.93
	Exclude event-6	-1.66	2.14	-1.89	3.57
	Average	-1.70	**1.81**	-1.95	**3.02**
Probit	**Exclude event-1**	-1.16	1.20	-1.44	2.34
	Exclude event-2	-0.95	0.25	-0.88	0.00
	Exclude event-3	-0.93	1.00	-1.21	2.15
	Exclude event-4	-1.00	1.08	-1.08	1.82
	Exclude event-5	-1.15	1.72	-1.29	2.35
	Exclude event-6	-1.01	1.31	-1.15	2.17
	Average	-1.03	**1.09**	-1.17	**1.80**

Model trained with full variables

At the beginning, model is trained with all five variables to evaluate their influences on flooding. As it is stated that cross-validation is used in this model, six images produced six sets of coefficients which are presents in table 6.3. In each event set one image is excluded from a dataset and used as validation data.

Table 6.3: Coefficients of Model trained by all variables

Regression	Event set	Coefficient						
		Intercept	Precipitation	Elevation	Distance to water area	Drainage capacity	Sea level (Carrolton)	Sea level (New canal)
Logistic	Exclude event-1	1.39	3.94	-15.10	-4.42	-1.09	-0.22	1.16
	Exclude event-2	2.49	1.38	-16.17	-5.90	-3.52	-0.03	1.40
	Exclude event-3	0.43	4.19	-12.83	-3.87	-0.94	0.08	2.64
	Exclude event-4	1.60	3.80	-13.67	-4.53	-1.81	-0.52	2.08
	Exclude event-5	0.28	1.81	-11.52	-3.81	-1.22	0.70	5.24
	Exclude event-6	1.62	0.71	-12.66	-4.33	-2.64	4.72	-12.23
	Average	**1.30**	**2.64**	**-13.66**	**-4.48**	**-1.87**	**0.79**	**0.05**
Probit	Exclude event-1	0.67	2.35	-8.35	-2.30	-0.56	-0.15	0.65
	Exclude event-2	1.10	0.74	-8.25	-2.62	-1.67	-0.03	0.70
	Exclude event-3	0.17	2.52	-7.34	-2.04	-0.45	0.02	1.52
	Exclude event-4	0.79	2.30	-7.60	-2.33	-1.00	-0.32	1.18
	Exclude event-5	0.06	1.17	-6.46	-2.01	-0.65	0.38	2.97
	Exclude event-6	0.87	0.49	-7.21	-2.27	-1.46	2.71	-7.10
	Average	**0.61**	**1.60**	**-7.54**	**-2.26**	**-0.96**	**0.44**	**-0.01**

From the table 6.3, it could be seen that factors' effects on flooding are the same as expectation for both regressions. The precipitation amount is in a positive relation with flooding, and the elevation and distance to the water area are in negative relations, which means with the larger precipitation, the lower elevation and the shorter distance to the water area, the chance of flooding is higher. In these three variables, the elevation has the largest influence on the chance of flooding. However, the coefficients of Carrollton sea level station and drainage capacity are smaller comparing to other factors'.

Two reasons could lead to the low correlation between drainage capacity and the probability of flooding. The first is that the drainage capacity is not correctly modelled. As it is discussed in the introduction of New Orleans, the drainage system in New Orleans is complicated, which has many stages. Therefore it might be too simplified to calculate all pump stations' capacity in the same manner. The other reason could be that during some events, not all pumping stations were working. As it is stated in the drainage department website of New Orleans county, whether a pump station is turned on depends on the situation of flooding, so during minor flooding events, some pumping stations were not functioning. However, due to that records of which pump stations were turned on are not traceable. In the model all pump stations are assumed to be working, which introduced discrepancy with reality.

The coefficients of two sea level stations behave differently. When training data set including event-6 (10^{th}, July, 2019), which are datasets 1 to 5, coefficients of Carrollton station fluctuate around zero and the coefficients of New

Canal station are around two. When the event 6 is included, the coefficient of Carrollton station indicates a great positive correlation between sea level and flooding, while coefficient of New Canal station suggests that flooding is very sensitive to sea level at New Canal station in a negative relation. The distinctive behaviour of the two stations' coefficients could be explained by their impact factors. New Canal station lies by the lake of Pontchartrain which is connected to Mexico gulf, and three main drainage canals flow into lake Pontchartrain. Carrollton station is set at Mississippi riverside whose water level is influenced by both river and tide, and elevation of Mississippi river levee is higher than sea levee's elevation. These causes could lead to coefficients' different behaviours.

For model trained by excluding event-6 (10^{th}, July, 2019), coefficients of two stations' records is positive for Carrollton station and negative for New Canal station, whose behaviours are different from other models. But the coefficients of other variables are not of large differences. Therefore the sea levels of all six events are demonstrated in the figure 6.5. As we can see in the figure, the sea level at New Canal station of that event is the lowest record, which happened to be at the lowest sea level in a tide circle. The sea level at Carrollton station is the second highest among all events caused by the 2019 Mississippi river flooding. The flood detection result of event happening at 10^{th}, July, 2019 no many areas were detected as flooded. So when data of event-6 is included in the input, the model considers the sea level at Carrollton has a more negative relation with flooding and the sea level at New Canal has a more positive one. After data of event-6 is excluded, the coefficient of the sea level at Carrollton increased and the coefficient of the sea level at New Canal station decreased.

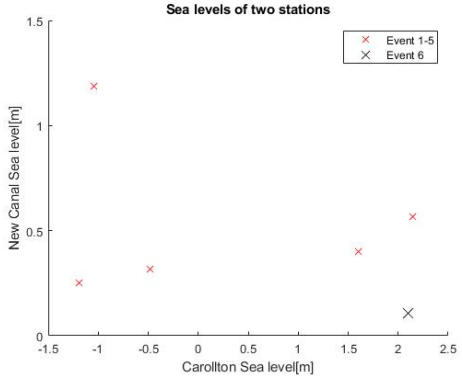

Figure 6.5: Sea level records of two station at New Orleans

Each variable's coefficients are averaged and result is the final set of coefficients of that model. The set of coefficient is then used to train each flood event to see its performance. ROC curve is again used here to present the model's performance.

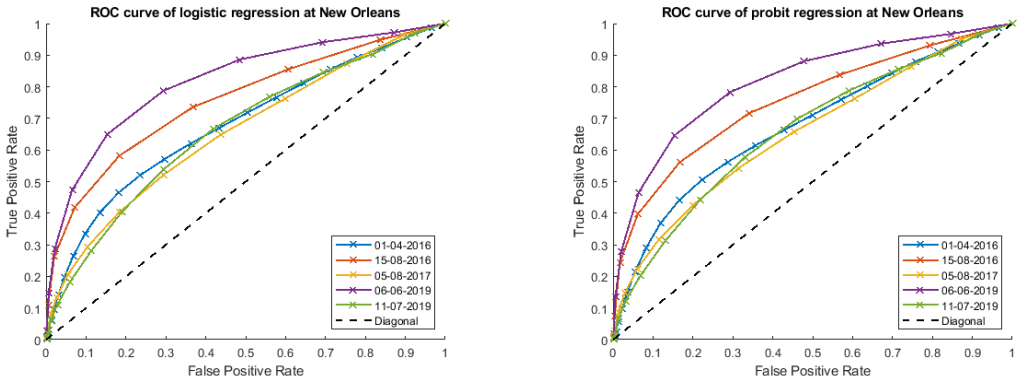

(a) Logistic regression

(b) Probit regression

Figure 6.6: ROC curve of New Orleans model trained with all variables

One event(2^{nd}, Sep., 2008) is not presented in the figure because one sea level station's record is not available at that time. Among the rest five events, result of predicting event on 6^{th}, Apr., 2019 (event-5) has a significantly better performance than other events' predictions. All curves are above the diagonal indicates that a consistent result that the model is capable of predicting the flooding to some extent. Modifications should be tested to see the potential of improving the model's performance.

Model trained with selected variables

The model is re-trained only with precipitation, elevation and distance to water area to test if the model's performance is improved when unimportant variables are eliminated. Result and coefficients are presented in table 6.4.

Table 6.4: Coefficients of model trained by selected variables

Regression	Event set	Coefficient			
		Intercept	**Precipitation**	**Elevation**	**Distance to water area**
Logistic	Exclude event-1	1.67	3.98	-14.92	-4.52
	Exclude event-2	2.91	-0.14	-15.10	-6.93
	Exclude event-3	1.90	3.50	-14.17	-3.99
	Exclude event-4	1.29	3.01	-10.51	-4.46
	Exclude event-5	2.44	3.84	-17.63	-2.81
	Exclude event-6	1.73	3.55	-12.80	-4.57
	Average	**1.99**	**2.96**	**-14.19**	**-4.55**
Probit	Exclude event-1	0.85	2.34	-8.34	-2.38
	Exclude event-2	1.52	-0.05	-8.41	-3.31
	Exclude event-3	1.06	2.11	-8.26	-2.20
	Exclude event-4	0.67	1.83	-6.01	-2.44
	Exclude event-5	1.26	2.30	-9.74	-1.59
	Exclude event-6	0.94	2.15	-7.41	-2.48
	Average	**1.05**	**1.78**	**-8.03**	**-2.40**

In the table, models trained by both logistic regression and probit regression show consistency as models trained with a full set of variables. Probability of flooding is related to elevation, precipitation and distance to water area in the same manner. Among these variables elevation has the highest absolute coefficient, and precipitation has the lowest. Of all training datasets, values of coefficients of one variable are consistent, except for coefficient of precipitation of model trained by dataset excluding flood event-2(29th, Aug., 2012). The reason behind that is the problem of flood detection of remote sensing image. The image of the event on 29th, Aug., 2012 was taken during hurricane Issac. In the image due to wind factor water area at New Orleans was unsettled and showed waves on the surface, which caused that during performing supervised classification the statistics of training data of class 'water' was incorrectly represented. The other reason could be that signals received by radar were perpetuated by heavy precipitation. The remote sensing image of event-2 is of high resolution but fuzzy. In flood detection result of that event, a large proportion of the study area is marked as water. Although it was a hurricane causing serious flooding, the contaminated image could lead to overestimation of flooded area which further caused inaccurate prediction.

The ROC curve of two GLMs are plotted in figure 6.7. Similar to a model trained with all variables, for all events both regressions are capable of predicting the flooding with curves above the diagonal, and prediction of event at 4th, April, 2019 has the best performance.

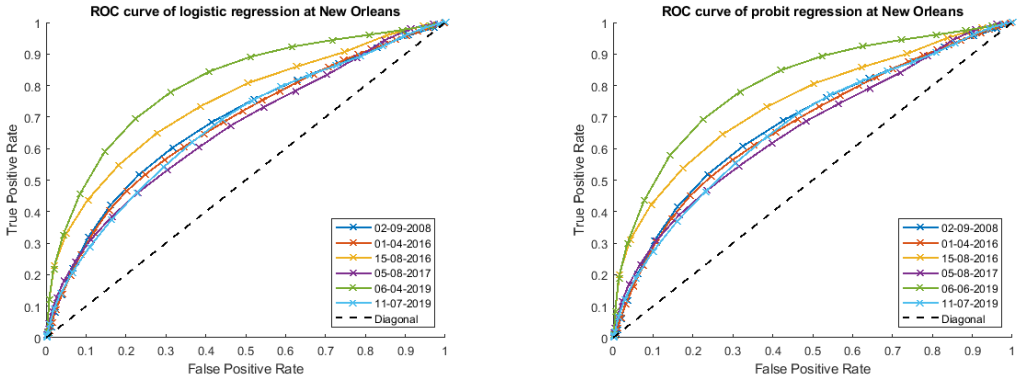

(a) Logistic regression

(b) Logistic regression

Figure 6.7: ROC curve of New Orleans model trained with important variables

Model trained without over-sampling

Aforementioned two kinds of models are both trained with dataset whose minority class 'flooded' was oversampled by SMOTE method. The model discussed here is trained by original dataset without oversampling for presenting how oversampling affects the result. Only three factors(precipitation, elevation and distance to drainage capacity) are used for training. Coefficients of each variable is summarised in table 6.5.

Coefficients of the model trained without over-sampling minority class are close to coefficient trained with oversampling, but the absolute value of most coefficients decreased in this model. It means this kind of model's range of probability of flooding is smaller than the model with over-sampling. This is also reflected in ROC curves 6.8. It is clear

Table 6.5: Coefficients of Model trained by selected variables without over-sampling

Regression	Data set	Coefficient			
		Intercept	Precipitation	Elevation	Distance to water area
Logistic	Exclude event-1	-0.87	3.89	-11.47	-4.84
	Exclude event-2	0.91	-0.89	-14.17	-5.36
	Exclude event-3	-0.25	2.72	-11.27	-4.61
	Exclude event-4	0.11	2.64	-12.25	-4.88
	Exclude event-5	-0.34	2.73	-10.97	-4.32
	Exclude event-6	0.06	2.75	-12.03	-4.88
	Average	**-0.06**	**2.31**	**-12.03**	**-4.82**
Probit	Exclude event-1	-0.73	1.91	-5.21	-2.01
	Exclude event-2	-0.05	-0.36	-5.90	-2.04
	Exclude event-3	-0.43	1.35	-5.18	-1.93
	Exclude event-4	-0.27	1.33	-5.63	-2.04
	Exclude event-5	-0.48	1.35	-5.02	-1.82
	Exclude event-6	-0.30	1.41	-5.50	-2.05
	Average	**-0.38**	**1.17**	**-5.41**	**-1.98**

that in each event's ROC curve there are much less points along curves. The available range of choosing the threshold of probability is too limited so that the threshold could easily be taken as a value larger than the highest predicted probability of flooding or lower than the smallest. Despite the smaller range of predicted probability, the trends of curves do not change much from the model that is trained after oversampling the dataset. prediction results are all above the diagonal line and prediction result of flooding event on 6th, April, 2019 has the best result. Quantitative analysis of this model and others should be made for an accurate assessment.

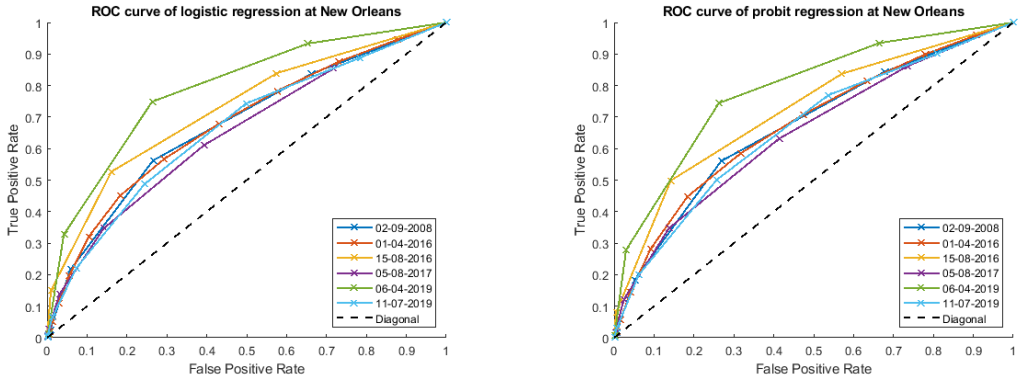

(a) Logistic regression

(b) Probit regression

Figure 6.8: ROC curve of New Orleans model trained with important variables without Over-sampling

6.2.2. Miami's flood forecast

Due to the limit number of image acquired for Miami, it does not make sense to train the first model structure with only six events. So at Miami only the second model structure is considered. Similar to New Orleans, class 'flooded' is over-sampled by SMOTE method to balance numbers of two classes' data points for each fold separately in cross-validation. For coastal flooding at Miami, only three variables are included: sea level, elevation and distance to water area.

Model trained with all variables

All flood conditioning factors are included in the first-run of the model to assess their relations to flooding, which are trained with logistic and probit regressions. And results are shown in table 6.6.

Coefficients in the table tell that for both regressions, models trained with all data sets have small differences. Models predict the relation between each variable and flooding correctly. Distance to the water area and elevation have negative impact and precipitation has a positive influence on flooding. Comparing to the other two variables, coefficients of distance to water area is more insignificant, which tells that it is a less important factor for flooding. Because this study area consists of islands and seaside area all of which are fairly close to sea and inland water system, distance to water area of the study area does not vary much across the study area. Next step is to eliminate this redundant factor.

Table 6.6: Coefficients of model of Miami trained with all variables

Regression	Event set	Coefficient			
		Intercept	Sea level	Elevation	Distance to water area
Logistic	Exclude event-1	-0.12	2.61	-7.83	-0.38
	Exclude event-2	0.48	1.51	-7.11	-0.25
	Exclude event-3	-1.19	4.05	-8.30	-0.03
	Exclude event-4	-0.20	2.53	-9.43	-0.61
	Exclude event-5	-0.09	2.63	-9.22	-1.04
	Exclude event-6	0.08	2.59	-9.22	-0.21
	Average	**-0.17**	**2.65**	**-8.52**	**-0.42**
Probit	Exclude event-1	-0.26	1.66	-4.00	-0.36
	Exclude event-2	0.34	0.93	-4.58	-0.07
	Exclude event-3	-0.63	2.40	-4.88	-0.25
	Exclude event-4	-0.05	1.54	-6.11	-0.39
	Exclude event-5	-0.06	1.53	-5.39	-0.58
	Exclude event-6	-0.16	1.64	-4.75	-0.21
	Average	**-0.14**	**1.62**	**-4.95**	**-0.31**

ROC curve in figure 6.9 shows the results of using average coefficients to predict each flooding event's extent and validating against the flood detection result. The difference between the result of each event is significant. Prediction of an event that happened on 4th, Nov., 2016 surpassed predictions of other events. Predictions of events that happened on 4th, July, 2017 morning and 26th, Sep., 2019 are not satisfying whose ROC curves are almost parallel with diagonal. The model is first revised to see if the prediction results of these two events could be improved.

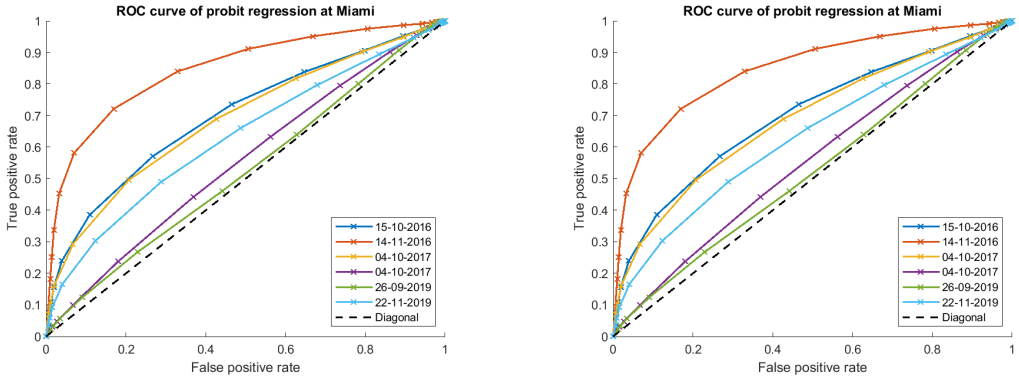

(a) Logistic regression

(b) Probit regression

Figure 6.9: ROC curve of Miami model trained with all variables

Model trained with sea level and elevation

As it is pointed out in the foregoing section that distance to water area is not an important factor to flooding at Miami study area, distance to water area is excluded and this model was trained with only sea level and elevation as input variables. Coefficients of two variables of two regressions are summarised in table 6.7.

Values of two variables' coefficients do not show huge changes. The average coefficients of elevation are -9.03 and -5.54 of logistic regression and probit regression correspondingly. Compared with sea levels' average coefficients which are 2.65 and 1.56, the absolute values of elevation's coefficients are much higher. It could be concluded that elevation is of higher importance on chances of flooding at Miami area. Accuracies of these two models are also evaluated by using the ROC curve to present the prediction results.

ROC curves are presented in figure 6.10. Performances between different events are still not consistent even with insignificant variable eliminated from the input. Forecasting result of event-4 and event-5 are lower than others'. Reviewing flood detection results and sea level records of these two events, the reason of poor accuracy of predictions of event-4 and event-5 should be from the remote sensing images. The sea levels of both events are about 1.06m which is not an extreme value among six events' sea level. But if we examine remote sensing images, both of them have speckles on the whole image, which renders it difficult to tell water area from land area apart. Algorithm classified more area as flooded on both images than flood detection results of events with same sea level. This could lead to low accuracy of the prediction result.

Table 6.7: Coefficients of models of Miami trained with sea level and elevation

Regression	Event set	Coefficient		
		Intercept	Sea level	Elevation
Logistic	Exclude event-1	0.05	2.54	-8.63
	Exclude event-2	0.48	1.55	-7.49
	Exclude event-3	-1.00	4.03	-9.12
	Exclude event-4	-0.02	2.48	-10.29
	Exclude event-5	-0.17	2.56	-9.51
	Exclude event-6	-0.10	2.75	-9.12
	Average	**-0.13**	**2.65**	**-9.03**
Probit	Exclude event-1	-0.06	1.54	-4.82
	Exclude event-2	0.27	0.92	-4.25
	Exclude event-3	-0.25	2.21	-6.19
	Exclude event-4	0.09	1.45	-6.49
	Exclude event-5	-0.04	1.58	-5.93
	Exclude event-6	-0.01	1.64	-5.58
	Average	**0.00**	**1.56**	**-5.54**

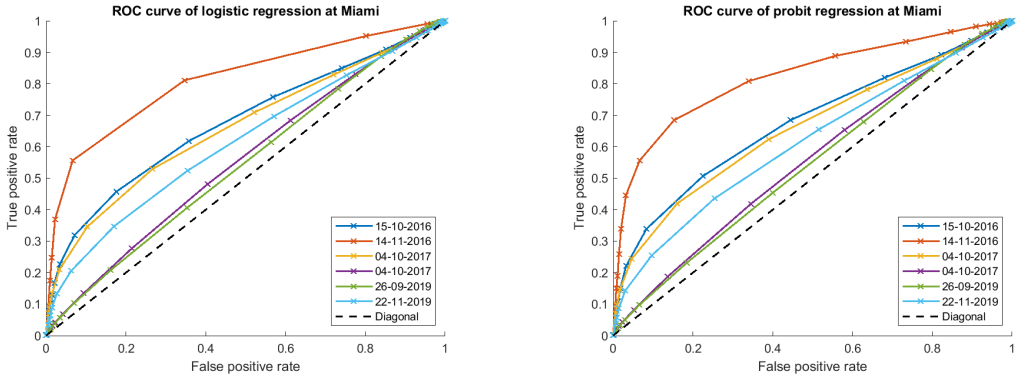

(a) Logistic regression (b) Probit regression

Figure 6.10: ROC curve of Miami model trained with sea level and elevation

Model of Miami Beach area

The northwest area of Miami study area is an urban area far from the sea, which has quite different land uses from the Miami Beach area, so that area is excluded from the training dataset to test the model's performance with focus on Miami Beach area. The trained coefficients at listed in table 6.8. No significant differences showed between this model's coefficients and others'. The accuracy of this model is also examined and presented by ROC curve in figure 6.11. By visual check the curves of ROC in figure 6.11 do shift towards the point(0,1), which suggests a better performance. Quantitative analysis is given in the next section.

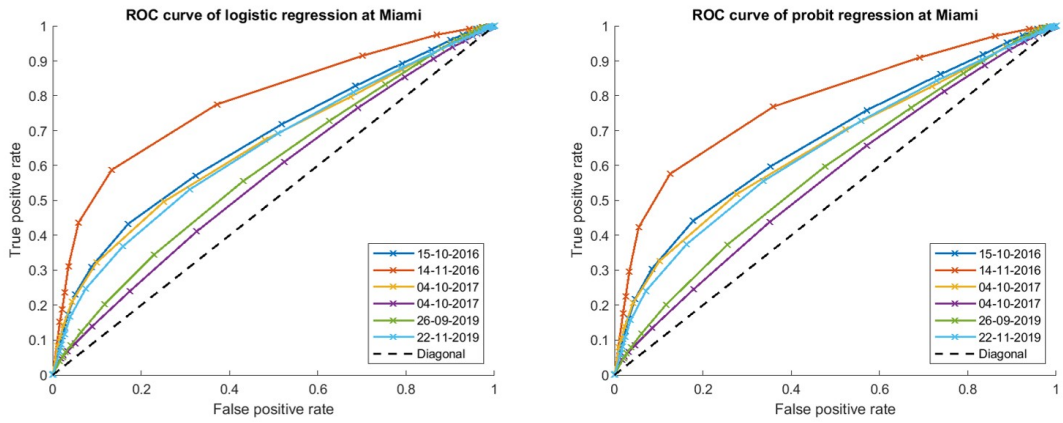

(a) Logistic regression (b) Probit regression

Figure 6.11: ROC curve of Miami Beach model

Table 6.8: Coefficients of models of Miami Beach

Regression	**Event set**	**Coefficient**		
		Intercept	**Sea level**	**Elevation**
Logistic	Exclude event-1	0.38	2.15	-8.45
	Exclude event-2	0.30	2.21	-8.96
	Exclude event-3	0.05	2.93	-9.65
	Exclude event-4	0.66	2.22	-11.98
	Exclude event-5	0.62	2.15	-10.61
	Exclude event-6	0.37	2.41	-9.69
	Average	0.40	2.34	-9.89
Probit	Exclude event-1	0.17	1.46	-5.25
	Exclude event-2	-0.03	1.33	-4.22
	Exclude event-3	-0.03	1.70	-5.14
	Exclude event-4	0.48	1.26	-7.24
	Exclude event-5	0.28	1.40	-6.33
	Exclude event-6	-0.01	1.50	-4.82
	Average	0.14	1.44	-5.50

6.2.3. Analysis and discussion

At both study areas, logistic regression and probit regression were used to construct the probabilistic model to forecasting flood extent. An iteration process is used, and each iteration left out one flood event's data from the input and resulted in one set of coefficients. All sets of coefficients are averaged and too]]k as model's coefficients. This final model gave the prediction of each flooding event and the result is validated against flood detection result. Figures of ROC curve have already been discussed and scores of each model is given in 6.9 and 6.10.

Table 6.9: Scores of models of New Orleans

Regression	Variable set	Threshold	Scores			
			Precision	Accuracy	F1	Kappa
Logistic	All variables	0.113	0.096	0.631	0.171	0.092
	Important variables	0.263	0.121	0.723	0.202	0.119
	Important variables without over-sampling	0.063	**0.126**	**0.736**	**0.209**	**0.127**
Probit	All variables	0.125	0.032	0.543	0.061	0.021
	Important variables	0.263	0.033	0.577	0.063	0.024
	Important variables without over-sampling	0.067	**0.036**	**0.655**	**0.069**	**0.030**

Highest values of each score are bolded in the table. At New Orleans study area, overall the model could achieve a high value of accuracy but score low in precision. Scores of F1 and cohen's kappa are not satisfying either. The highest accuracy is 12.6% and the highest cohen's kappa is 0.127, both of which are given by model trained by logistic regression with three important factors without oversampling. It slightly outruns model with the same input variables using logistic regression with the oversampling technique. Using all variables to train the model gives the worst result by both regressions. In conclusion, models' performances are improved after eliminating unimportant factors, but whether adopting over-sampling technique could result in a more accurate model is not clear.

As for choosing the cutoff value of the probability of flooding, after eliminating less important factors, the cutoff value of probability rose from about 12% to 26%. But if the model is trained without over-sampling the minority class, the cutoff value will be lowest around 6.4%. Too narrow a range of probability will cause difficulty in identifying the high risk of flooding. Despite its small advantage in precision and other scores, not over-sampling the minority class is not encouraged.

For comparing two regressions' adaptability to flood extent forecasting, it is clear that at New Orleans study area model trained by logistic regression has a significantly better result in all scores than probit regression indicating that logit link function is more suitable for modelling probability of flooding. The cutoff of probability does not differ much for two regressions.

Scores of Miami are presented in table 6.10. Among models of Miami, cohen's kappa and accuracy do not change much. Eliminating distance to the water area does not improve the model's performance. The reason is that the variable distance to water area is not significant so that in the first model which was trained with all variables, its impact has already been small on the prediction result. Therefore it does not make a large difference when it is excluded from the input variables. The performance of the model improved when the study area is limited to the Miami Beach area, and the model scores the highest values of Cohen's kappa and precision, which indicates the importance of consider-

Table 6.10: Scores of models of Miami

Regression	Variable set	Threshold	Scores			
			Precision	Accuracy	F1	Kappa
Logistic	All variables	0.488	0.204	0.479	0.329	0.115
	With sea level and elevation	0.488	0.203	0.470	0.329	0.114
	Miami beach	0.533	**0.236**	**0.504**	**0.366**	**0.131**
Probit	All variables	0.683	0.204	0.479	0.329	0.115
	With sea level and elevation	0.679	0.205	**0.566**	0.312	0.109
	Miami beach	0.533	**0.232**	0.485	**0.365**	**0.125**

ing the land use in the training.

Cutoff values of probability are higher of models trained by probit regression than logistic regression for models of Miami. The cutoff value of probability of probit regression reaches 68% while the latter's cutoff values are at 48.8%, but all of these four cutoff values are higher than cutoff values of models of New Orleans.

Comparing table 6.10 and table 6.9, it could be concluded that models of Miami study area trumps models of New Orleans. At Miami, the values of precision of all four models are almost the same at 20%, and F1 scores are higher than that of models of New Orleans. Flooding mechanism could be the reason. At Miami, not flood defence system is built to protect the area from tidal flooding, which only lasts for hours, so flooding area is linked to sea level and elevation in a very straightforward manner. However, at New Orleans, complicated flood defence system which consists of a drainage system and levee system makes the generation of the flood a very intricate process.

Odd ratios of the key variables of two study areas are calculated and summarised in table 6.11. As it is stated in the section 4.2.4, $odds = \frac{p(Y=1)}{p(Y=0)} = exp(\beta_i)$, which indicates the change when variable X_i change. If the sea level is 10cm higher, as it is indicated in the table, the probability of one location being flooded is almost two times higher. A storm event with 50mm larger precipitation amount means the chance of one location being flooded is almost 1.5 times higher for New Orleans. For both study areas, if the elevation is 0.5m, then the probability of flooding is 0.95 times less.

Table 6.11: Odds of key variables at two study area

Miami			New Orleans		
	Sea level			**Precipitation**	
	Increased amount	Odds		Increased amount	Odds
	10cm	2.09		50mm	1.46
	Elevation			**Elevation**	
	Increased amount	Odds		Increased amount	Odds
	0.5m	0.94		0.5m	0.95

6.3. Summary

In this chapter the flood detection result is used as input along with other variables to trained probabilistic models based on logistic regression and probit regression. Two study areas' predictions are made with different sets of variables and two kinds of model structures are tested.

The first model structure models forecast flood based on each independent cell. However, due to the lack of data, a large area could not train a model successfully. For Model structure two, a cross-validation iteration was used and coefficients of each iteration are averaged to arrive final models. Each event is tested and validated against the flood detection result, and scores of validations are presented. At New Orleans study area, considering the time effect in calculating precipitation proves to be important, and the accuracy of the model is improved by only using significant variables as input. Over-sampling method turns out to be not efficient in raising accuracy, however it is suggested to employ the over-sample method so the range of forecasted probability is larger and the identification of high-risk area is more clear. At Miami study area, the overall performance of models is superior to New Orleans, although it is still not satisfying. Excluding the variable of distance to water area does not affect models' result, and regression method does not make a huge difference in the result either. But considering the land-use in the model does improve the model's performance.

7

Conclusion and recommendation

This study aims to investigate the feasibility of using flood detection result arrived from remote sensing image to predict flood extent. Two study locations are examined and nineteen images are processed. Flood detection result along with other flood conditioning factors are used as input to construct two different probabilistic forecast models. Logistic regression and probit regressions are the used probabilistic methods and SMOTE method is adopted to oversample the minority class before forecasting.

First SAR images that recorded flooding were collected and analysed. Each image is processed in the same manner. The image was first segmented into polygons delineating land objects by using seed region growing method. Next segmentation result is performed with supervised classification to identify water area. Although in the test image, this procedure could achieve a satisfying accuracy, the validation result of flood detection is not good. There are several reasons resulting in this. The primary reason is that images taken by varies sensors and at varies states are all used in analysis to make sure that the number of images is sufficient. Other seasons like precipitation, cloud and low resolution could also hinder flooded area from being accurately mapped.

Two different model structures are constructed with logistic regression and probit regression. The first kind of model structure proved to be immature currently. Lacking data renders this model's prediction unstable and inaccurate, which is reflected in that at some locations,the lacking of data caused failure in training. The second kind of model did not give a satisfying result either with precision being low. However, the second model could prove the clear relation between key flood conditioning factors and flood.

At both study area, the variable of elevation resulted in the highest absolute value of coefficients, which proves that elevation in highly related to flooding despite the different mechanisms of the flooding in two study areas. At New Orleans area, the variable precipitation has positive coefficient to flooding for all event sets. It means that the model could link the precipitation to flooding. Similarly at Miami study area, the sea level has an positive relation with flooding. While at New Orleans study area, the variable of distance to the water area turns out to be an important factor, however, at Miami study area, it is of small effect on flooding. Other variables such as drainage capacity and sea level at New Orleans are considered as insignificant factors. This is because that it is difficult to model the complicated drainage system in New Orleans, and the flood defence system mitigate the effects of sea level on the city's flooding.

For flood prediction at New Orleans area, two methods to calculate the precipitation amount are used, one of which considered the time effect. The time-weighted precipitation amount turns out to have a much larger coefficient, hence a closer relation to flooding than the simply summed-up precipitation. This test proves to us that when analysing pluvial flooding, the time element should not be obliviated. In Miami area, the last model excluded an part of urban area with the focus on Miami Beach city. And the accuracy gets an obvious improvement. It is a strong suggestion that different land uses exhibit different flood characteristics and land use should be included in this model.

Although the accuracy of all models are not yet satisfying, the model can connect variables with the flood detection result. All variables especially precipitation, sea level and precipitation are correctly linked to flooding judging by their coefficients. Even the time effect of precipitation could be reflected in the result. Despite the low accuracies, the study do prove that using remote sensing images for flood extent forecasting is a feasible way. Improvements and modification should be able to result in a more accurate and functional model.

The reasons that could caused the low accuracy of the detection are quality of remote sensing images and the structure of the probabilistic model. There is a discrepancy of the qualities between images resulting in inaccurate flood detection result, which further effects the forecasting. In terms of forecast model, some important variables are not considered in the input, such as land-use and slope. Some variables could contain important information concerning flooding, so the model should take more factors into account.

No researches have been done before, which is to apply multiple remote sensing images in flood forecasting. It make this research an investigative study. Studies have been performed in the way that one remote sensing image was used to predict the flood extent of one single event, however, in this study, records from several events are integrated

together for the purpose of predicting flood extent. Therefore this study serves to explore the potential of using past flooding events remote sensing images to predict the future flooding events' extents. In the next stage, if this model is fed with enough numbers of remote sensing images and more flood conditioning factors are included, it is fair to expect the performance of this model could be good enough for it to be applied in reality.

7.1. Recommendation

In this study, based on other researches, methodology employed in this paper and models' result, there is still room for improvement and perfection. For future studies, there are some constructive suggestions.

1. **Methods of gridding the study area**

   Shape of cell could be in other forms like triangular and polygons. Study areas are gridded into rectangular in this study and cell length was defined at a small value to control the precision. But it is possible to subdivide the study area into cells with different shapes following the edge of streets, water area and building blocks. In this way it could avoid the problem of involving two different land objects into one cell. This method will impose difficulty in interpolation and computational power.

2. **Improve flood detection method**

   Judging from the flood detection result, it should be admitted that some images are not accurately analysed. The method employed in this study to detect flooding is proved to be accurate, but due to different conditions when each image was taken, and uneven resolutions of images, it would be better to used algorithms and methods targeted at each image's problem. For example some images were taken during a storm which was interfered by precipitation and clouds, and by thorough analysis this contamination on image could be removed.

3. **Increasing the number of remote sensing image**

   This suggestion is given specifically for the first kind of model structure. It is clear that a number of data points at each cell limits the model's performance. Now with Sentinel mission being on an operation, it could provide a large number of available images in the next few years for this kind of studies, especially when Sentinel mission's product is public. The model should be able to make much more accurate prediction with more images.

4. **Using more advanced probabilistic forecasting algorithms**

   Some other probabilistic model is worth to investigating for this study. Two regressions are used in this study for constructing the model: logistic regression and probit regression. They both belong to the generalised linear regression family and the only difference between them is the link function. Other methods such as Bayesian Network should be tested to see their compatibility of forecasting. Other deep learning algorithms such as neural network is also worth to be examined for model structure 2.

5. **Considering other flood conditioning factors**

   Five factors are considered in this study's model, but some other factors related to flooding could be informative. Topographic factors such as slope and topographic wetness index are usually considered in hydrologic modelling. Land use type could be useful too. Grass, forest and urban area should have responded to flooding differently. Considering varies factors and employing features selecting method could help in choosing the most important factors.

Bibliography

R. Adams and L. Bischof. Seeded region growing. *IEEE Transactions on Pattern Analysis and Machine Intelligence*, 16 (6):641–647, June 1994. ISSN 1939-3539. doi: 10.1109/34.295913.

European Space Agency. Esa earth observation missions. https://earth.esa.int/web/guest/missions/esa-eo-missions, a. [Online; accessed 02-04-2020].

European Space Agency. Sentinel-1. https://sentinel.esa.int/web/sentinel/missions/sentinel-1, b. [Online; accessed 19-Oct-2019].

Heiko Apel, Annegret H. Thieken, Bruno Merz, and Günter Blöschl. A probabilistic modelling system for assessing flood risks. *Natural Hazards*, 38(1):79–100, May 2006. ISSN 1573-0840. doi: 10.1007/s11069-005-8603-7. URL https://doi.org/10.1007/s11069-005-8603-7.

Benjamin Bechtel, Andre Ringeler, and Jürgen Böhner. Segmentation for object extraction of trees using matlab and saga. 01 2008.

Asim Biswas and Bing Si. *Model Averaging for Semivariogram Model Parameters*, pages 81–96. 07 2013. doi: 10.5772/52339.

J. Böhner, K.R. McCloy, and J. Strobl. *SAGA - Analysis and Modelling Applications*. Göttinger geographische Abhandlungen. Goltze, 2006. URL https://books.google.nl/books?id=1zOAAAAAMAAJ.

G. Boni, L. Ferraris, L. Pulvirenti, G. Squicciarino, N. Pierdicca, L. Candela, A. R. Pisani, S. Zoffoli, R. Onori, C. Proietti, and P. Pagliara. A prototype system for flood monitoring based on flood forecast combined with cosmo-skymed and sentinel-1 data. *IEEE Journal of Selected Topics in Applied Earth Observations and Remote Sensing*, 9(6):2794–2805, June 2016. ISSN 1939-1404.

P. A. Brivio, R. Colombo, M. Maggi, and R. Tomasoni. Integration of remote sensing data and gis for accurate mapping of flooded areas. *International Journal of Remote Sensing*, 23(3):429–441, 2002. doi: 10.1080/01431160010014729. URL https://doi.org/10.1080/01431160010014729.

N. V. Chawla, K. W. Bowyer, L. O. Hall, and W. P. Kegelmeyer. Smote: Synthetic minority over-sampling technique. *Journal of Artificial Intelligence Research*, 16:321–357, Jun 2002. ISSN 1076-9757. doi: 10.1613/jair.953. URL http://dx.doi.org/10.1613/jair.953.

Marco Chini, Ramona Pelich, Luca Pulvirenti, Nazzareno Pierdicca, Renaud Hostache, and Patrick Matgen. Sentinel-1 insar coherence to detect floodwater in urban areas: Houston and hurricane harvey as a test case. *Remote Sensing*, 11(2), 2019. ISSN 2072-4292. doi: 10.3390/rs11020107. URL https://www.mdpi.com/2072-4292/11/2/107.

Bechtel B. Bock M. Dietrich H. Fischer E. Gerlitz L. Wehberg J. Wichmann V. Conrad, O. and J. Böhner. System for automated geoscientific analyses (saga), 2015.

Gayathri K. Devia, B.P. Ganasri, and G.S. Dwarakish. A review on hydrological models. *Aquatic Procedia*, 4:1001 – 1007, 2015. ISSN 2214-241X. doi: https://doi.org/10.1016/j.aqpro.2015.02.126. URL http://www.sciencedirect.com/science/article/pii/S2214241X15001273.

Timothy Dixon, Falk Amelung, Alessandro Ferretti, Fabrizio Novali, Fabio Rocca, Roy Dokka, G. Sella, Sang-Wan Kim, Shimon Wdowinski, and Dean Whitman. Subsidence and flooding in new orleans. *Nature*, 441:587–588, 05 2006. doi: 10.1038/441587a.

G. Donchyts. Planetary-scale surface water detection from space, 01 2018. ISSN 978-94-6233-862-3.

Q. Duan, Y. Yan, and A. V. Vasilakos. A survey on service-oriented network virtualization toward convergence of networking and cloud computing. *IEEE Transactions on Network and Service Management*, 9(4):373–392, December 2012. ISSN 1932-4537. doi: 10.1109/TNSM.2012.113012.120310.

R.W. Fitzgerald and B.G. Lees. Assessing the classification accuracy of multisource remote sensing data. *Remote Sensing of Environment*, 47(3):362 – 368, 1994. ISSN 0034-4257. doi: https://doi.org/10.1016/0034-4257(94)90103-1. URL http://www.sciencedirect.com/science/article/pii/0034425794901031.

R. Fjortoft, A. Lopes, P. Marthon, and E. Cubero-Castan. An optimal multiedge detector for sar image segmentation. *IEEE Transactions on Geoscience and Remote Sensing*, 36(3):793–802, May 1998. ISSN 1558-0644. doi: 10.1109/36.673672.

Yan Gao, Jean Francois Mas, Norman Kerle, and Jose Antonio Navarrete Pacheco. Optimal region growing segmentation and its effect on classification accuracy. *International Journal of Remote Sensing*, 32(13):3747–3763, 2011. doi: 10.1080/01431161003777189. URL https://doi.org/10.1080/01431161003777189.

Javier García-Pintado, David C. Mason, Sarah L. Dance, Hannah L. Cloke, Jeff C. Neal, Jim Freer, and Paul D. Bates. Satellite-supported flood forecasting in river networks: A real case study. *Journal of Hydrology*, 523:706 – 724, 2015. ISSN 0022-1694. doi: https://doi.org/10.1016/j.jhydrol.2015.01.084. URL http://www.sciencedirect.com/science/article/pii/S0022169415001031.

Noel Gorelick, Matt Hancher, Mike Dixon, Simon Ilyushchenko, David Thau, and Rebecca Moore. Google earth engine: Planetary-scale geospatial analysis for everyone. *Remote Sensing of Environment*, 202:18 – 27, 2017. ISSN 0034-4257. doi: https://doi.org/10.1016/j.rse.2017.06.031. URL http://www.sciencedirect.com/science/article/pii/S0034425717302900. Big Remotely Sensed Data: tools, applications and experiences.

Shasha Han and Paulin Coulibaly. Bayesian flood forecasting methods: A review. *Journal of Hydrology*, 551:340 – 351, 2017. ISSN 0022-1694. doi: https://doi.org/10.1016/j.jhydrol.2017.06.004. URL http://www.sciencedirect.com/science/article/pii/S0022169417304031. Investigation of Coastal Aquifers.

Justine Henonin, Beniamino Russo, Ole Mark, and Philippe Gourbesville. Real-time urban flood forecasting and modelling – a state of the art. *Journal of Hydroinformatics*, 15(3):717–736, 02 2013. ISSN 1464-7141. doi: 10.2166/hydro.2013.132. URL https://doi.org/10.2166/hydro.2013.132.

Jochen Hinkel, Daniel Lincke, Athanasios T. Vafeidis, Mahé Perrette, Robert James Nicholls, Richard S. J. Tol, Ben Marzeion, Xavier Fettweis, Cezar Ionescu, and Anders Levermann. Coastal flood damage and adaptation costs under 21st century sea-level rise. *Proceedings of the National Academy of Sciences*, 111(9):3292–3297, 2014. ISSN 0027-8424. doi: 10.1073/pnas.1222469111. URL https://www.pnas.org/content/111/9/3292.

Yukiko Hirabayashi, Mahendran Roobavannan, Sujan Koirala, Lisako Konoshima, Dai Yamazaki, Satoshi Watanabe, Hyungjun Kim, and Shinjiro Kanae. Global flood risk under climate change. *Nature Climate Change*, 3:816–821, 09 2013. doi: 10.1038/nclimate1911.

LA Jefferson Parish. Jefferson parish drainage department. http://www.jeffparish.net/departments/drainage. [Online; accessed 22-12-2019].

Roman Krzysztofowicz. Bayesian theory of probabilistic forecasting via deterministic hydrologic model. *Water Resources Research*, 35(9):2739–2750. doi: 10.1029/1999WR900099. URL https://agupubs.onlinelibrary.wiley.com/doi/abs/10.1029/1999WR900099.

Venkat Lakshmi. *Remote Sensing of Hydrological Extremes*. 01 2017. ISBN 978-3-319-43743-9. doi: 10.1007/978-3-319-43744-6.

Lianfa Li, Jinfeng Wang, Hareton Leung, and Chengsheng Jiang. Assessment of catastrophic risk using bayesian network constructed from domain knowledge and spatial data. *Risk Analysis*, 30(7):1157–1175, 2010. doi: 10.1111/j.1539-6924.2010.01429.x. URL https://onlinelibrary.wiley.com/doi/abs/10.1111/j.1539-6924.2010.01429.x.

Dengsheng Lu and Qihao Weng. A survey of image classification methods and techniques for improving classification performance. *International Journal of Remote Sensing*, 28:823 – 870, 03 2007. doi: 10.1080/01431160600746456.

Darren Lumbroso, Paul Orr, Clare Twigger-Ross, Elham Kashefi, Gordon Walker, and Nigel Watson. Communication and dissemination of probabilistic flood warnings - final report, 09 2009.

Radosław Malinowski, Geoff Groom, Wolfgang Schwanghart, and Goswin Heckrath. Detection and delineation of localized flooding from worldview-2 multispectral data. *Remote Sensing*, 7(11):14853–14875, 2015. ISSN 2072-4292. doi: 10.3390/rs71114853. URL http://www.mdpi.com/2072-4292/7/11/14853.

S. Martinis, A. Twele, and S. Voigt. Towards operational near real-time flood detection using a split-based automatic thresholding procedure on high resolution terrasar-x data. *Natural Hazards and Earth System Sciences*, 9(2):303–314, 2009. doi: 10.5194/nhess-9-303-2009. URL https://www.nat-hazards-earth-syst-sci.net/9/303/2009/.

F. S. Marzano, S. Mori, and J. A. Weinman. Evidence of rainfall signatures on x-band synthetic aperture radar imagery over land. *IEEE Transactions on Geoscience and Remote Sensing*, 48(2):950–964, Feb 2010. ISSN 1558-0644. doi: 10.1109/TGRS.2009.2034843.

Andrew Mehnert and Paul Jackway. An improved seeded region growing algorithm. *Pattern Recognition Letters*, 18 (10):1065 – 1071, 1997. ISSN 0167-8655. doi: https://doi.org/10.1016/S0167-8655(97)00131-1. URL http://www.sciencedirect.com/science/article/pii/S0167865597001311.

F. Molteni, R. Buizza, T. N. Palmer, and T. Petroliagis. The ecmwf ensemble prediction system: Methodology and validation. *Quarterly Journal of the Royal Meteorological Society*, 122(529):73–119, 1996. doi: 10.1002/qj.49712252905. URL https://rmets.onlinelibrary.wiley.com/doi/abs/10.1002/qj.49712252905.

Giorgos Mountrakis, Jungho Im, and Caesar Ogole. Support vector machines in remote sensing: A review. *ISPRS Journal of Photogrammetry and Remote Sensing*, 66(3):247 – 259, 2011. ISSN 0924-2716. doi: https://doi.org/10.1016/j.isprsjprs.2010.11.001. URL http://www.sciencedirect.com/science/article/pii/S0924271610001140.

A. Nandi, Arpita Mandal, Matthew Wilson, and David Smith. Flood hazard mapping in jamaica using principal component analysis and logistic regression. *Environmental Earth Sciences*, 75, 03 2016. doi: 10.1007/s12665-016-5323-0.

NASA. Nasa shuttle radar topography mission global 1 arc second v003. https://gcmd.nasa.gov/KeywordSearch/Metadata.do?Portal=daacs&KeywordPath=Parameters%7CLAND+SURFACE%7CTOPOGRAPHY%7CTOPOGRAPHIC+EFFECTS&EntryId=SRTMGL13&MetadataView=Full&MetadataType=0&lbnode=mdlb2. [Online; accessed 22-12-2019].

J. A. Nelder and R. W. M. Wedderburn. Generalized linear models. *Journal of the Royal Statistical Society: Series A (General)*, 135(3):370–384, 1972. doi: 10.2307/2344614. URL https://rss.onlinelibrary.wiley.com/doi/abs/10.2307/2344614.

Steve Nixon. Eu overview of methodologies used in preparation of flood hazard and flood risk maps. Technical report, Jan 2016.

OpenStreetMap contributors. Geofabrik. http://download.geofabrik.de/, 2020.

Emmanuel Opolot. Application of remote sensing and geographical information systems in flood management: A review. *Research Journal of Applied Sciences, Engineering and Technology*, 6:1884–1894, 07 2013. doi: 10.19026/rjaset.6.3920.

N. Otsu. A threshold selection method from gray-level histograms. *IEEE Transactions on Systems, Man, and Cybernetics*, 9(1):62–66, Jan 1979. ISSN 2168-2909. doi: 10.1109/TSMC.1979.4310076.

Biswajeet Pradhan. Flood susceptible mapping and risk area delineation using logistic regression, gis and remote sensing. *Journal of Spatial Hydrology*, 9:1–18, 01 2009.

Stefan Rahmstorf. A semi-empirical approach to projecting future sea-level rise. *Science*, 315(5810):368–370, 2007. ISSN 0036-8075. doi: 10.1126/science.1135456. URL https://science.sciencemag.org/content/315/5810/368.

J. Rogers. Development of the new orleans flood protection system prior to hurricane katrina. *Journal of Geotechnical and Geoenvironmental Engineering - J GEOTECH GEOENVIRON ENG*, 134, 05 2008. doi: 10.1061/(ASCE)1090-0241(2008)134:5(602).

Mayra A. Román-Rivera and Jean T. Ellis. The king tide conundrum. *Journal of Coastal Research*, pages 769–771, 2018. doi: 10.2112/JCOASTRES-D-18A-00001.1. URL https://doi.org/10.2112/JCOASTRES-D-18A-00001.1.

Siddharth Saksena and Venkatesh Merwade. Incorporating the effect of dem resolution and accuracy for improved flood inundation mapping. *Journal of Hydrology*, 530:180 – 194, 2015. ISSN 0022-1694. doi: https://doi.org/10.1016/j.jhydrol.2015.09.069. URL http://www.sciencedirect.com/science/article/pii/S0022169415007520.

Stefan Schlaffer, Patrick Matgen, Markus Hollaus, and Wolfgang Wagner. Flood detection from multi-temporal sar data using harmonic analysis and change detection. *International Journal of Applied Earth Observation and Geoinformation*, 38:15 – 24, 2015. ISSN 0303-2434. doi: https://doi.org/10.1016/j.jag.2014.12.001. URL http://www.sciencedirect.com/science/article/pii/S0303243414002645.

Sewerage and Water Board of New Orleans. Drainage system facts and map. https://www.swbno.org/About/DrainageSystemFactsAndMap. [Online; accessed 22-12-2019].

D. Stewart, D. Blacknell, A. Blake, R. Cook, and C. Oliver. Optimal approach to sar image segmentation and classification. *Radar, Sonar and Navigation, IEE Proceedings* -, 147:134 – 142, 07 2000. doi: 10.1049/ip-rsn:20000400.

William V. Sweet, Robert E. Kopp, Christopher P. Weaver, Jayantha Obeysekera, Radley M. Horton, E. Robert Thieler, and Chris Zervas. Global and regional sea level rise scenarios for the united states. Technical report, 2007.

Dan Swenson and Jeff Adelson. Emptying the bowl. https://www.nola.com/news/environment/article_1fc9c490-fc6f-509c-a2df-105d420b9dae.html. [Online; accessed 02-04-2020].

Mahyat Shafapour Tehrany, Biswajeet Pradhan, and Mustafa Neamah Jebur. Spatial prediction of flood susceptible areas using rule based decision tree (dt) and a novel ensemble bivariate and multivariate statistical models in gis. *Journal of Hydrology*, 504:69 – 79, 2013. ISSN 0022-1694. doi: https://doi.org/10.1016/j.jhydrol.2013.09.034. URL http://www.sciencedirect.com/science/article/pii/S0022169413006872.

F. Tupin, J. Inglada, and J.M. Nicolas. *Remote Sensing Imagery*. ISTE. Wiley, 2014. ISBN 9781118898925. URL https://books.google.nl/books?id=GfcXAwAAQBAJ.

USGS. What is remote sensing and what is it used for? https://www.usgs.gov/faqs/what-remote-sensing-and-what-it-used?qt-news_science_products=3#qt-news_science_products. [Online; accessed 22-Oct-2019].

Burkett V., R., Zilkoski D., B., and Hart D., A. Sea-level rise and subsidence: Implications for flooding in new orleans, louisiana. In *USGS Aquifer Mechanics and Subsidence Interest Group conference*, pages 63–70. U.S. Geological Survey, 2001.

Charles Verpoorter, Tiit Kutser, and Lars Tranvik. Automated mapping of water bodies using landsat multispectral data. *Limnology and Oceanography: Methods*, 10(12):1037–1050. doi: 10.4319/lom.2012.10.1037. URL https://aslopubs.onlinelibrary.wiley.com/doi/abs/10.4319/lom.2012.10.1037.

Bin Wang, Atsuo Ono Members, Kanako Muramatsu Nonmember, and Noboru Fujiwara Member. Automated detection and removal of clouds and their shadows from landsat tm images. *IEICE Transactions on Information and Systems*, E82-D, 09 1999.

Shimon Wdowinski, Ronald Bray, Ben P. Kirtman, and Zhaohua Wu. Increasing flooding hazard in coastal communities due to rising sea level: Case study of miami beach, florida. *Ocean Coastal Management*, 126:1 – 8, 2016. ISSN 0964-5691. doi: https://doi.org/10.1016/j.ocecoaman.2016.03.002. URL http://www.sciencedirect.com/science/article/pii/S0964569116300278.

Wikipedia. Drainage system at new orleans. https://en.wikipedia.org/wiki/Drainage_in_New_Orleans. [Online; accessed 02-04-2020].

World Meteorological Organization (WMO). *Guidelines on Ensemble Prediction Systems and Forecasting*, 2012.

Hanqiu Xu. Modification of normalised difference water index (ndwi) to enhance open water features in remotely sensed imagery. *International Journal of Remote Sensing*, 27(14):3025–3033, 2006. doi: 10.1080/01431160600589179. URL https://doi.org/10.1080/01431160600589179.

Xiucheng Yang and Li Chen. Evaluation of automated urban surface water extraction from sentinel-2a imagery using different water indices. *Journal of Applied Remote Sensing*, 11:026016, 05 2017. doi: 10.1117/1.JRS.11.026016.

Xiucheng Yang, Qiming Qin, Pierre Grussenmeyer, and Mathieu Koehl. Urban surface water body detection with suppressed built-up noise based on water indices from sentinel-2 msi imagery. *Remote Sensing of Environment*, 219:259 – 270, 2018. ISSN 0034-4257. doi: https://doi.org/10.1016/j.rse.2018.09.016. URL http://www.sciencedirect.com/science/article/pii/S0034425718304279.

Chinatsu Yonezawa and Shoji Takeuchi. Effect of clouds on ers sar interferograms applied to land subsidence detection. *International Journal of Remote Sensing*, 24(1):169–174, 2003. doi: 10.1080/01431160304999. URL https://doi.org/10.1080/01431160304999.

Y.Wang, J.D.Colby, and K.A. Mulcahy. An efficient method for mapping flood extent in a coastal floodplain using landsat tm and dem data. *International Journal of Remote Sensing*, 23(18):3681–3696, 2002. doi: 10.1080/01431160110114484. URL https://doi.org/10.1080/01431160110114484.

Fang Zhang, Xiaolin Zhu, and Desheng Liu. Blending modis and landsat images for urban flood mapping. *International Journal of Remote Sensing*, 35(9):3237–3253, 2014. doi: 10.1080/01431161.2014.903351. URL https://doi.org/10.1080/01431161.2014.903351.

A

Information of reported flooded location

Locations that are marked as flooded from NOAA's storm event database and news are presented here. Date, exact location, source of information are presented in table A.1 and A.2. In all these twenty-seven locations, nineteen are detected correctly.

Table A.1: Location reported flooded and source of records at New Orleans

Study area	Year	Month	Day	Location	Scource
New Orleans	2008	9	1	Upper Ninth Ward	https://www.pressreader.com/uk/the-herald-1130/20080902/282776352335739
					https://www.ncdc.noaa.gov/stormevents/eventdetails.jsp?id=135638
	2010	5	16	-	https://www.ncdc.noaa.gov/stormevents/eventdetails.jsp?id=226257
	2011	9	4	Touro Infirmary	https://www.ncdc.noaa.gov/stormevents/eventdetails.jsp?id=348281
	2012	4	4	Sections of Gentilly	https://www.ncdc.noaa.gov/stormevents/eventdetails.jsp?id=364487
	2012	8	29	St. Roch Ave. At cross of St. Charles Ave. and Erato St.	https://www.reuters.com/article/us-storm-isaac/new-orleans-withstands-isaacs-wrath-for-now-idUSBRE87L0PH20120829 https://www.ncdc.noaa.gov/stormevents/eventdetails.jsp?id=410285
	2016	4	1	Tucker Ave. Morris Place 400-Blk Rosa Ave. 1400-Blk Papworth Ave. Edenborn Ave. N. Arnoult Ave. Bonnabel Blvd 1300-Blk Aris Ave. WNapoleon 500-Blk Arlington Dr Entrance to Earhart from Clearview 600-Blk Oaklawn Ave. At cross of N Corporate DrMounes St 1600 Blk of Carrollton Ave. 1200 Blk Of Dealers Ave. 1432 Lake Ave.	https://www.fox8live.com/story/31621616/jefferson-parish-flooded-streets/ https://www.ncdc.noaa.gov/stormevents/eventdetails.jsp?id=623206
	2017	8	5	S. Carrolton st. City park Ave. At cross of Bank St. and St. Genois New Orleans Public Library	https://www.youtube.com/watch?v=odJdauUIUhI https://www.ncdc.noaa.gov/stormevents/eventdetails.jsp?id=713244
	2019	4	4	742 S Jefferson Davis Pkwy 700 S Clark St. North Rendon and St. Peter street Basin St. near Claiborne Ave.	https://www.youtube.com/watch?v=0Aw0Vcb7BY8 https://www.nola.com/news/article_89760af1-4536-55d1-985b-591e28eb3637.html https://www.youtube.com/watch?v=d0I3hs9c85A https://www.youtube.com/watch?v=oQQL3bYSmEo
	2019	7	10	1598 St Bernard Ave. 833 Canal St 4325 Banks St	https://www.youtube.com/watch?v=qp5EVzGpa6Q https://www.nola.com/news/healthcare_hospitals/article_4d7097ea-a340-11e9-adc3-53715c9eee61.html https://www.ncdc.noaa.gov/stormevents/eventdetails.jsp?id=846023 https://www.ncdc.noaa.gov/stormevents/eventdetails.jsp?id=835355

Table A.2: Location reported flooded and source of records at Miami

Study area	Year	Month	Day	Location	Scource
Miami	2016	10	15	Edgwater area	IEM Local Storm Application:
				24th, 50th, and 53rd St.	https://mesonet.agron.iastate.edu/lsr/#CRP/201602292300/201612262259/0100"
				Collins Ave.	
				Lincoln Rd.	
	2016	11	14	Biscayne Park	
	2017	10	4	78th St.	
				Byron Ave.	
	2019	9	26	Brickell Bay Dr.	
				SE 2 St.	
				East of State Road A1A	

B

Information of remote sensing images

Remote sensing applied in this study are from four satellites, and each image is taken by different sensors at different conditions. The detailed properties of these images are given in table B.1.

Table B.1: Information of image analyzed

Study area	Satellite	Mode	Resolution(m)	Polarisation mode	Incident angle(Deg.)	Orbit dir.	Year	Month	Day	Hour	Minute	Coverage of study area
New Orleans	TerraSAR-X	ScanSAR	18	HH	37.87	Descending	2008	9	2	11	58	Full
	Radarsat-2	High Incidence	20×28	HH	58.11	Descending	2008	9	2	11	39	Full
	COSMO-SkyMed	ScanSAR(HugeRegion)	100	VV	46.74	Descending	2010	5	16	23	51	Partial
	COSMO-SkyMed	StripMap(HIMAGE)	3	HH	32.19	Ascending	2011	9	4	11	52	Full
	TerraSAR-X	High Resolution	1	HH	43.32	Descending	2012	4	3	11	59	Partial
	COSMO-SkyMed	StripMap(HIMAGE)	3	HH	32.21	Ascending	2012	4	3	11	50	Partial
	TerraSAR-X	StripMap	3	HH	24.81	Descending	2012	8	29	12	8	Partial
	Radarsat-2	ScanSAR narrow	50	VV	30.24	Ascending	2016	4	1	23	57	Full
	TerraSAR-X	Wide ScanSAR	40	HH	34.55	Descending	2016	8	15	11	59	Full
	Radarsat-2	ScanSAR narrow	50	VV	39.31	Descending	2017	8	6	11	55	Full
	COSMO-SkyMed	StripMap(HIMAGE)	3	HH	32.19	Ascending	2018	8	22	11	41	Partial
	Sentinel-1	IW	22.5	VV	32.90	Ascending	2019	4	6	0	2	Full
	Sentinel-1	IW	22.5	VV	32.90	Ascending	2019	7	11	0	2	Full
Miami	Sentinel-1	IW	22.5	VV	32.90	Ascending	2016	10	15	23	27	Full
	Sentinel-1	IW	22.5	VV	32.90	Ascending	2016	11	14	23	27	Full
	Sentinel-1	IW	22.5	VV	32.90	Ascending	2017	10	4	23	27	Full
	COSMO-SkyMed	StripMap(HIMAGE)	3	HH	29.31	Ascending	2017	10	4	11	3	Partial
	COSMO-SkyMed	StripMap(HIMAGE)	3	HH	23.91	Descending	2019	9	26	23	12	Full
	COSMO-SkyMed	StripMap(HIMAGE)	3	HH	29.31	Ascending	2019	11	22	11	4	Partial

C

Drainage system of New Orleans study area

The New Orleans study area covers the Jefferson Parish and Orleans Parish.The modelled drainage capacity is calculated based on information about pump stations taken from the government official sites of these two Parishes. Figure C.1 presents the distribution of pumps stations of Jefferson Parish ,and figure C.2 provides information about the pump stations of Orleans Parish.

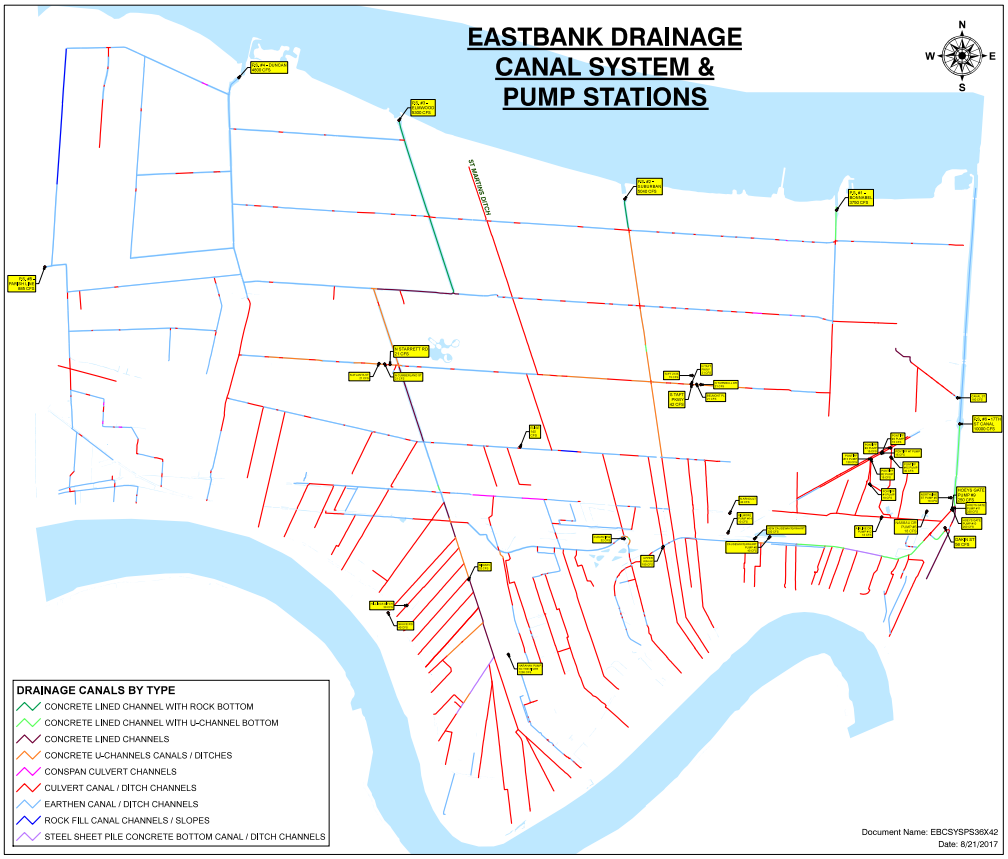

(a) East Bank

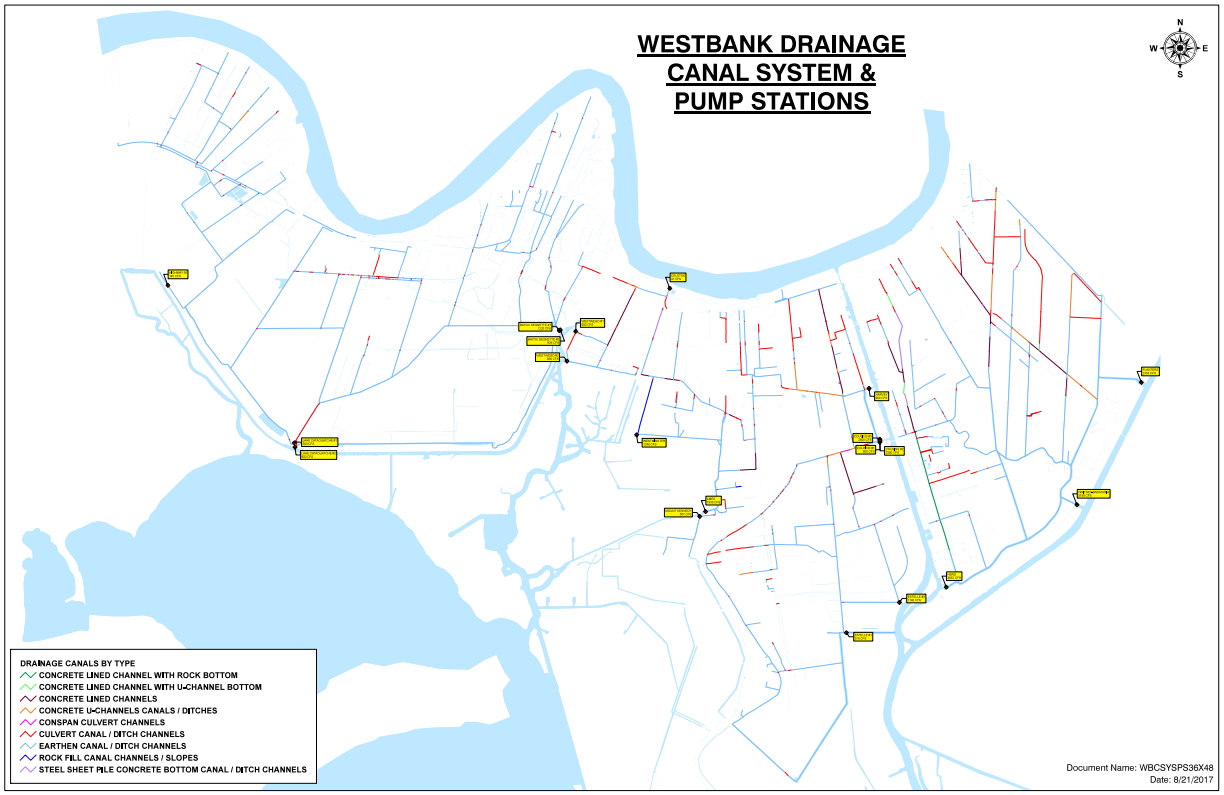

(b) West Bank

Figure C.1: Drainage system in Jefferson Parish

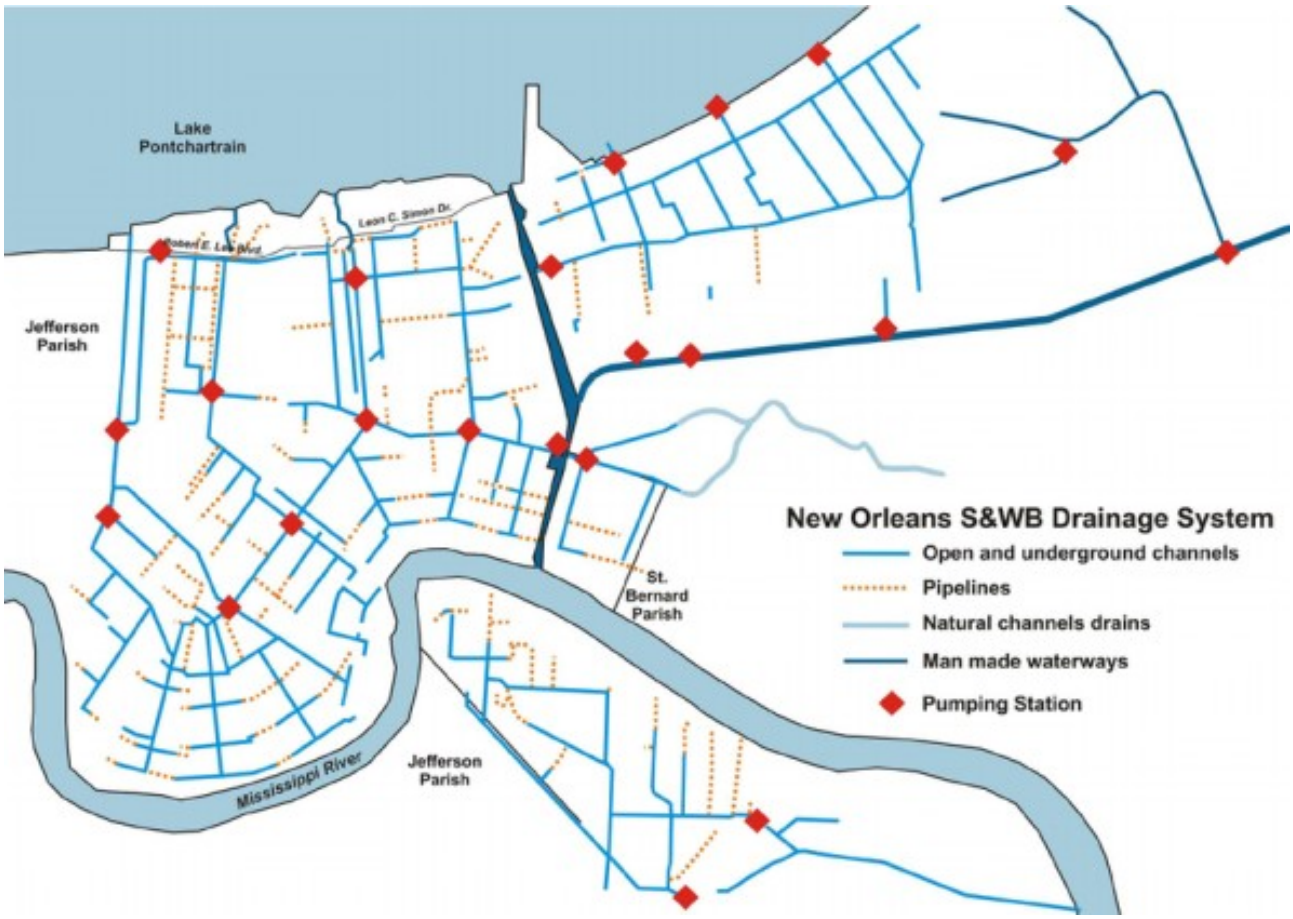

Figure C.2: Drainage system in City of New Orleans